

2014-04-25

Oscillatory wall strain reduction precedes arterial intimal hyperplasia in a murine model

John T. Favreau
Worcester Polytechnic Institute

Follow this and additional works at: <https://digitalcommons.wpi.edu/etd-dissertations>

Repository Citation

Favreau, J. T. (2014). *Oscillatory wall strain reduction precedes arterial intimal hyperplasia in a murine model*. Retrieved from <https://digitalcommons.wpi.edu/etd-dissertations/172>

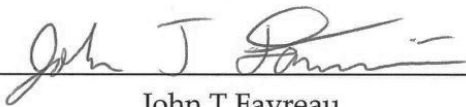
This dissertation is brought to you for free and open access by Digital WPI. It has been accepted for inclusion in Doctoral Dissertations (All Dissertations, All Years) by an authorized administrator of Digital WPI. For more information, please contact wpi-etd@wpi.edu.

Oscillatory wall strain reduction precedes arterial intimal hyperplasia in a murine model

A Dissertation
Submitted to the Faculty of the
WORCESTER POLYTECHNIC INSTITUTE
In partial fulfillment of the requirements for the Degree of
Doctorate of Philosophy in Biomedical Engineering

April 16th, 2014

By


John T Favreau



Glenn R. Gaudette, Ph.D.
Associate Professor, Advisor
Department of Biomedical Engineering
Worcester Polytechnic Institute



Cosme Furlong, Ph.D.
Associate Professor
Department of Mechanical Engineering
Worcester Polytechnic Institute



C. Keith Ozaki, M.D.
Associate Professor of Surgery
Brigham and Women's Hospital/
Harvard Medical School
Adjunct Associate Professor
Department of Biomedical Engineering
Worcester Polytechnic Institute



Yanhang Zhang, Ph.D.
Associate Professor
Department of Mechanical Engineering
Boston University



Marsha W. Rolle, Ph.D.
Associate Professor
Department of Biomedical Engineering
Worcester Polytechnic Institute



Helene Langevin, M.D.
Professor of Medicine
Brigham and Women's Hospital/
Harvard Medical School

Acknowledgements

I would like to thank a number of people for their assistance with this project. First and foremost, I would like to thank my advisor, Glenn Gaudette Ph.D. for his endless support on all aspects of this project. During my time at WPI, Glenn has given me invaluable experience as a researcher. From learning new surgical techniques to giving lectures to writing grants, Glenn has enabled me to have a hand in all aspects of his lab's research. This experience has helped me to grow as a scientist and a leader.

In addition to Dr. Gaudette, I must recognize C. Keith Ozaki M.D. and the Vascular Surgery Research Laboratory at Brigham and Women's Hospital. From my very first semester as a graduate student to the very end of my research, the Ozaki Lab has welcomed me as a researcher in their lab. In working with the Ozaki Lab, I have learned to view research from a clinical perspective and to understand some of the unique issues related to surgical research. I am truly grateful to all of the members of the Ozaki lab for their hospitality and guidance throughout the past 4 years.

My dissertation committee – which includes Dr. Cosme Furlong and Dr. Marsha Rolle of WPI, Dr. Yanhang Zhang of Boston University, Dr. Helene Langevin of Brigham and Women's Hospital, along with Dr. Gaudette and Dr. Ozaki – have been invaluable throughout my dissertation preparation and research. They have provided thoughtful insight to much of my research and I am thankful for the time they have spent with me.

I would also like to thank the faculty of the WPI Biomedical Engineering Department as well as the core staff at Gateway Park. The open lab environment at Gateway has enabled me to exchange ideas with other researchers in the field of biomedical engineering and improve the overall quality of this work. Additionally, the imaging and histology core have contributed significantly to improving the quality of images presented in this work.

I must also acknowledge the many members of the Gaudette lab who have aided me with this project. Whether through sectioning and staining tissues or providing critical review of papers and presentations, my fellow graduate and undergraduate students in the lab have been indispensable in enabling all of my work.

I am also indebted to a number of people and organizations for their provision of key equipment or financial support for this project. In particular, access to ultrasound equipment used herein was provided in part by Ronglih Liao Ph.D. and the Brigham and Women's Hospital Cardiovascular Physiology Core, Helene Langevin M.D. and the Osher Center at Brigham and Women's Hospital and FUJIFILM Visualsonics Inc. My time at WPI was also funded in part by a WPI Teaching Assistantship, an American Heart Association Predoctoral Fellowship, the Koerner Family Foundation, and an NIH R01 grant.

Last but certainly not least, I must thank my family and friends for supporting me throughout this process. Particularly, I would like to thank my parents, Thomas and Mary Favreau and my fiancée Elyse for their support. I could not have done this without you.

Table of Contents

Acknowledgements.....	ii
Table of Contents.....	iii
Table of Figures.....	vii
Table of Tables	viii
Abbreviations.....	ix
Abstract.....	x
1 Overview.....	1
1.1 Introduction	1
1.2 Overall goal and hypothesis.....	4
1.3 Specific Aim I: Develop and apply a noninvasive, ultrasound-based method for measuring mechanical strain in the murine vasculature	5
1.3.1 Objective 1A: Validate an ultrasound-based strain measurement technique	6
1.3.2 Objective 1B: Apply the ultrasound based method <i>in vivo</i> in a murine model of vascular disease.....	6
1.4 Specific Aim II: Evaluate if a relationship exists between oscillatory wall strain and intimal hyperplasia formation	6
1.4.1 Objective 2: Determine what relationship exists between mechanical strain and pathological wall remodeling.....	7
1.5 Specific Aim III: Determine if changes in oscillatory wall strain precede formation of intimal hyperplasia <i>in vivo</i>	7
1.5.1 Objective 3A: Determine the temporal progression of wall strain in the focal stenosis model	8
1.5.2 Objective 3B: Determine the temporal progression of intimal hyperplasia in the focal stenosis model.....	8
2 Background	9
2.1 Introduction	9
2.1.1 The cardiovascular system.....	9
2.1.2 Vascular structure	9
2.1.3 Mechanical forces on the vessel wall.....	13
2.2 Vascular disease	16
2.2.1 Relation between intimal hyperplasia and vascular disease	16
2.2.2 Relation between Wall shear stress and vascular disease	18
2.2.3 Relation between wall tensile stress and strain and vascular disease	19

2.3	Techniques for measuring vascular mechanics <i>in vivo</i>	22
2.3.1	Measurement of wall shear stress.....	22
2.3.2	Measurement of wall tensile stress.....	24
2.3.3	Measurement of wall strain	25
2.4	Summary	26
3	Objective 1A: Validation of ultrasound strain measurement.....	28
3.1	Introduction	28
3.2	Materials and methods.....	29
3.2.1	Development of an <i>in vitro</i> model of pulsatile pressure.....	31
3.2.2	Ultrasound data acquisition and analysis	33
3.2.3	Video data acquisition and analysis.....	34
3.2.4	Theoretical relationships.....	35
3.2.5	Statistics	35
3.3	Results.....	36
3.3.1	Comparison of optical and ultrasound strain measurements	36
3.3.2	Theoretical relationships between lumen and outside strains	38
3.4	Discussion	40
4	Objective 1B: <i>In vivo</i> testing of ultrasound vascular strain methodology.....	44
4.1	Introduction	44
4.1.1	Aortic aneurysms	44
4.1.2	Murine models of aortic aneurysms.....	44
4.2	Materials and methods.....	45
4.2.1	Mouse model	45
4.2.2	Dietary perturbations	46
4.2.3	Study design	46
4.2.4	Strain calculation.....	49
4.2.5	Statistics	50
4.3	Results.....	50
4.3.1	Effects of diet on aortic strain.....	50
4.3.2	Short term impact of Angiotensin-II treatment on mechanical strain.....	52
4.3.3	Long term effects of angiotensin II treatment on mechanical strain.....	53
4.3.4	Relative effects of different factors on mechanical strain.....	54

4.4	Discussion	56
4.5	Conclusions.....	61
5	Objective 2: Determination of the relationship between circumferential wall strain and intimal hyperplasia.....	62
5.1	Introduction	62
5.2	Materials and methods.....	62
5.2.1	Study design	62
5.2.2	Mouse model	63
5.2.3	Ultrasound data acquisition	63
5.2.4	Strain calculations	64
5.2.5	Tissue Harvest and Histology	65
5.2.6	Statistics	66
5.3	Results.....	66
5.3.1	Wall strain analysis.....	67
5.3.2	Histological analysis of wall adaptations	67
5.3.3	Temporal progression of arterial cross-sectional areas	68
5.3.4	Relationship between Day 27 strain and Histological outcome.....	70
5.4	Discussion	72
6	Objective 3A: Determine the temporal progression of wall strain in the focal stenosis model.....	74
6.1	Introduction	74
6.2	Materials and methods.....	74
6.2.1	Experimental Design	74
6.2.2	Relationship between early strain and eventual intimal hyperplasia	75
6.3	Results.....	76
6.3.1	Wall strain analysis.....	76
6.3.2	Temporal progression of arterial cross-sectional areas	77
6.3.3	Relationship between acute strain and subsequent intimal thickness	79
6.4	Discussion	81
7	Objective 3B: Determine the temporal progression of intimal hyperplasia in the focal stenosis model	84
7.1	Introduction	84
7.2	Materials and methods.....	85

7.2.1	Experimental design	85
7.2.2	Ultrasound data acquisition	85
7.2.3	Focal stenosis model	86
7.2.4	Quantification of Intimal Thickness and Wall Thickness.....	86
7.2.5	Assessment of cell type markers	87
7.2.6	Assessment of cell proliferation	88
7.2.7	Assessment of glycosaminoglycan synthesis.....	88
7.2.8	Statistical Analyses.....	89
7.3	Results.....	89
7.3.1	Ultrasound strain analysis	89
7.3.2	Changes in wall cross-sectional area	92
7.3.3	Histological analysis of intimal thickness.....	94
7.3.4	Relationship between strain and diameter	95
7.3.5	Immunohistochemical analysis.....	96
7.4	Discussion	100
8	Conclusions and Future Work.....	103
8.1	Conclusions.....	103
8.2	Limitations	108
8.3	Future work	110
	Works Cited.....	115
	Appendix A: Reprint permissions	130
	Permissions for Chapter 4	130
	Permissions for Chapters 5 and 6.....	140
	Appendix B: Staining protocols and controls.....	147
	Masson's Trichrome	147
	Ki-67 and alpha Smooth Muscle Actin.....	150
	Hyaluronic acid and Versican	153
	Myosin Heavy Chain, CD-31 and CD-45.....	155
	Appendix C: Derivation of theoretical strain relationship	158
	Appendix D: Determination of vessel layer thickness	160

Table of Figures

Figure 1-1: Staining of vessels with intimal hyperplastic lesions.	2
Figure 1-2: Overall hypothesis of this dissertation.	5
Figure 2-1: Structure of the healthy artery.	12
Figure 2-2: Forces applied to the blood vessel wall <i>in vivo</i>	16
Figure 3-1: Comparison of sonomicrometry and HDM strains.	30
Figure 3-2: Ultrasound validation experimental setup.	32
Figure 3-3: Close-up of ultrasound validation tubing setup.	33
Figure 3-4: Use of High Density Mapping to determine displacement fields.	35
Figure 3-5: Computation of green's strain from HDM data.	35
Figure 3-6: Simulated wall strains in Penrose tubing.	36
Figure 3-7: Sample regions of interest and strain curves.	37
Figure 3-8: Comparison of wall strains recorded with ultrasound and HDM.	38
Figure 3-9: Theoretical relationship between lumen and outside strains for silicon tubing.	40
Figure 4-1: Segments of interest analyzed in the thoracic and abdominal aorta.	48
Figure 4-2: Sample ultrasound image of an aorta.	49
Figure 4-3: Comparison of baseline preoperative strain magnitudes.	52
Figure 4-4: Short and long term effects of Ang II on normal and high fat animals.	54
Figure 4-5: Effects of Ang II and aneurismal degeneration on aortic wall strain.	56
Figure 5-1: Objective 2 study design.	64
Figure 5-2: Regional differences in strain.	67
Figure 5-3: Morphological analysis of day-28 carotid arteries.	68
Figure 5-4: Changes in (A) diastolic and (B) systolic lumen area.	69
Figure 5-5: Relationship between day 27 strain and day 28 intimal thickness.	71
Figure 5-6: Quantitative relationship between day 27 strain and neointima formation.	71
Figure 6-1: Schematic of Aim 3A study.	75
Figure 6-2: Regional differences in strain.	78
Figure 6-3: Changes in (A) diastolic and (B) systolic lumen area.	79
Figure 6-4: Differences in LCCA regions with low (<0.1) and high (>0.1) day 4 strain.	81
Figure 7-1: Experimental design for Aim 3B studies.	85
Figure 7-2: Average oscillatory wall strain.	90
Figure 7-3: Average regional oscillatory wall strains.	91
Figure 7-4: Progression of strain in control and experimental arteries.	91
Figure 7-5: Histogram analysis of strain data at each time point.	92
Figure 7-6: Changes in arterial cross-sectional area throughout the experiment.	93
Figure 7-7: Use of Masson's Trichrome to find thickness of vessel layers.	94
Figure 7-8: Intimal thickness and wall thickness at day 4.	95
Figure 7-9: Differences in cross-sectional area between low and high strain groups.	96
Figure 7-10: Myosin heavy chain, CD-31 and CD-45 expression.	97
Figure 7-11: Ki-67 and α SMA expression in control and experimental arteries.	98
Figure 7-12: Hyaluronic acid and versican expression in control and experimental arteries.	99
Figure 8-1: Summary of the results of this dissertation.	107
Figure 8-2: Two-photon microscopy analysis of medial elastin and collagen.	112

Table of Tables

Table 4-A: Experimental groups for Objective 1A.....	46
Table 5-A: Sample sizes used for strain and histological analyses.....	66
Table 6-A: Sample sizes used for strain and histological analyses on the LCCA.....	76

Abbreviations

AAA	Abdominal aortic aneurysm
ANG II	Angiotensin II
apoE	Apolipoprotein-E
CAD	Coronary artery disease
CT	Computed Tomography
CVD	Cardiovascular disease
ECM	Extracellular matrix
EEL	External elastic lamina
eNOS	Endothelial nitric oxide synthase
GAG	Glycosaminoglycan
HA	Hyaluronic acid
HDM	High density mapping
IEL	Internal elastic lamina
IH	Intimal hyperplasia
LCCA	Left common carotid artery
MRI	Magnetic resonance imaging
NO	Nitric Oxide
OCT	Optical coherence tomography
PAD	Peripheral artery disease
RCCA	Right common carotid artery
SMC	Smooth muscle cell

Abstract

Cardiovascular diseases (CVD) remain the most common cause of death in the United States. Additionally, peripheral artery disease affects thousands of people each year. A major underlying cause of these diseases is the occlusion of the coronary or peripheral arteries due to arteriosclerosis. To overcome this, a number of vascular interventions have been developed including angioplasty, stenting, endarterectomies and bypass grafts. Although all of these methods are capable of restoring blood flow to the distal organ after occlusion, they are all plagued by unacceptably high restenosis rates. While the biological reactions that occur as a result of each of these methods differ, the initiating factor of both the primary atherosclerosis and subsequent failure of vascular interventions appears to be intimal hyperplasia (IH).

Intimal hyperplasia is most simply defined as the expansion of multiple layers of cells internally to the internal elastic lamina of the blood vessel. This excessive cellular growth leads to arterial stenosis, plaque formation and inflammatory reactions. Despite extensive research the underlying factors that cause IH remain unclear. A quantity of research to date has implicated endothelial cell mechanosensation as the mechanism by which IH is initiated with evidence positively correlating wall shear stress with IH. Others, however, have demonstrated that changes in the stresses applied to the wall *in vitro* can modulate IH independent of hemodynamic shear stress. Thus, relations between wall tensile stress and IH *in vivo* may shed light on the underlying mechanisms of IH. Since noninvasive measurement of wall tensile stress *in vivo* is difficult, it is most feasible to measure oscillatory wall strain which is intimately related to wall tensile stress through the mechanical properties of the arterial wall. In this dissertation, we hypothesize that reductions in oscillatory wall strain precede the formation of intimal hyperplasia in a murine model.

To test our hypothesis, we first developed a novel, high spatial and temporal resolution method to measure oscillatory wall strains in the murine common carotid artery. We validated this method both *in vitro* using an arterial phantom and *in vivo* using a murine model of abdominal aortic aneurysms. To assess relationships between strain and IH, we applied our strain measurement technique to a recently developed mouse model of IH. In this model, a suture is used to create a focal stenosis and reduce flow through the common carotid artery by 85%; resulting in proximal IH formation. Using this approach, we identified a relationship between oscillatory strain reductions and IH. Subsequent analysis demonstrated that early reductions in mechanical strain just 4 days after focal stenosis creation correlate with IH formation nearly 1 month later.

Since IH is not expected to form by day 4 in this model, we went on to assess changes in gross vascular morphology at day 4. We discovered that, although strains are significantly reduced by day 4, no significant IH can be observed, suggesting that changes in wall structure are resulting in strain reductions. At day 4 post-op, we observed cellular proliferation and leukocyte recruitment to the wall without intimal hyperplasia. These studies suggest that early reductions in mechanical strain may be an important predictor of IH formation. Clinically, this relation could be important for the development of novel techniques for predicting IH formation before it becomes hemodynamically significant.

1 Overview

1.1 Introduction

The 2013 update of the American Heart Association's heart disease and stroke statistics indicates that 32.3% of deaths in the United States list cardiovascular disease (CVD) as the underlying cause and that more than 50% of death certificates mention CVD as a contributing factor to death.¹ Although the death rates per 100,000 Americans due to CVD have declined from 864.9 in 1999 to 243.9 in 2009, the prevalence of CVD is expected to rise from 35.6% to 40.8% by the year 2030.¹ These statistics indicate a real clinical need to improve our understanding and treatment of CVD and its causes.

Coronary artery disease (CAD) and peripheral artery disease (PAD) both contribute significantly to mortality and morbidity in the United States, each affecting more than 14 million Americans.¹ CAD is estimated to have been responsible for over 1.2 million hospital stays in 2004 and was determined the most expensive condition treated in hospitals and caused more than 50% of cardiovascular events.¹ Similarly, PAD caused 14,000 deaths in 2009 and also contributes to CVD prevalence.²

Although a number of evidence based interventions have been applied to treat CAD and PAD, these interventions fail to address the underlying causes of the diseases.³ Present day treatments for CAD and PAD include angioplasty, stents, endarterectomies, and bypass grafts. Although these treatments have decreased the mortality rates due to arterial occlusive diseases, all continue to suffer from unacceptably high failure rates which in some cases exceed 50%.^{2, 4, 5} While the biologic adaptation underlying the failure of each of these treatments differs subtly, the underlying cause of both the primary arterial occlusive disease and the subsequent treatments appears to be intimal hyperplasia (IH).⁶⁻¹¹

Intimal hyperplasia is characterized by the expansion of multiple layers of cells expressing alpha smooth muscle actin (α SMA) internally to the internal elastic lamina of a blood vessel (Figure 1-1).^{3, 12} This expansion often results in the appearance and aggregation of foam cells, accumulation of cholesterol and the eventual formation of atherosclerotic plaques.^{3, 12, 13} In the healthy adult artery, smooth muscle cells (SMCs) remain outside the internal elastic lamina and maintain a homeostatic level of growth to maintain vessel size and structure with a very low rate of both proliferation and death.¹⁴⁻¹⁸ In the pathological state, however, SMCs can be seen to migrate into the intimal compartment of the vessel. This proliferative and migratory response is the primary underlying mechanism that initiates arteriosclerosis, arterial occlusion and the eventual end organ ischemia associated with CAD, PAD and virtually all contemporary treatments of the disease.^{3, 6-11, 14}

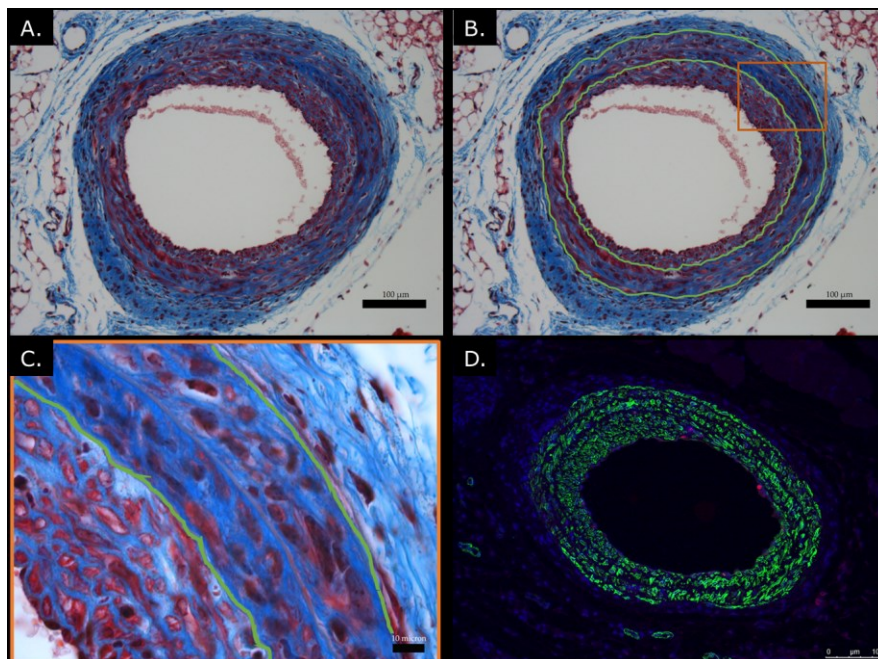


Figure 1-1: Staining of vessels with intimal hyperplastic lesions. A) Masson's Trichrome stain of a mouse carotid artery with intimal hyperplasia. B) Masson's Trichrome stain with overlaid green tracings of the internal and external elastic laminae. C) Close-up of region shown in B. D) Dual stain of Ki-67 (red) and alpha smooth muscle actin (green) showing cells expressing alpha smooth muscle actin within the internal elastic lamina and cellular proliferation at the edge of the vessel lumen.

Although a number of hypotheses have been made as to why IH occurs, a long line of evidence suggests that cellular sensing of the mechanical environment that the artery is exposed to provides the cues that initiate IH. Low wall shear stress,¹⁹ high wall tensile stress²⁰ and the combination of both factors²¹ may play a role in the formation of IH in the vessel wall. Others suggest that wall strain, which is closely related to wall stress, may play a more direct role in IH formation.²² Although a number of researchers have implicated wall shear stress as the primary factor affecting IH formation,²³⁻²⁶ shear-based explanations alone fail to predict many aspects of IH.^{27, 28} A leading hypothesis is that the arterial wall actively maintains a homeostatic level of wall stress.²⁹⁻³¹ This theory is supported by the observation that the number of lamellar units in any given artery is proportional to blood vessel diameter.³² By maintaining this relationship, the vascular wall keeps the mechanical tension per lamellar unit within an amazingly narrow physiological range, even across numerous mammalian species.³² Since wall stress and strain are intimately related through the mechanical properties of the vessel wall, others have suggested that wall strain, not stress, is the underlying state sensed by the cell.³³ The sheer volume of literature relating the mechanical environment to IH suggests that *in vivo* assessment of arterial mechanics may be useful for the characterization, diagnosis and prevention of IH and arterial occlusive diseases.

Given that wall stress is difficult to measure accurately *in vivo*, analysis of wall strain represents a more promising mechanical property to assess in living models. *In vivo* wall strain has been assessed using a number of methodologies which are both invasive and non-invasive including MRI,^{34, 35} ultrasound³⁶ and high speed light imaging based methods³⁷. Herein we

develop a novel method to assess cyclic arterial strain in a murine model and determine the relationship between cyclic wall strain and IH.

1.2 Overall goal and hypothesis

The overall goal of this study is to determine the relationship between cyclic wall strain and IH in a small animal model of arterial occlusive disease. **We hypothesize that reductions in oscillatory wall strain precede the formation of intimal hyperplasia in a murine model** (Figure 1-2). The expected outcome of this dissertation is to provide compelling evidence to support the above hypothesis and to enable future research to establish if mechanical strain can be used to predict IH formation in the mouse or in larger animals.

To systematically test our hypothesis, this dissertation was divided into three specific aims and 5 objectives. Herein, we first aim to develop and validate a novel, high spatial and temporal resolution method for measuring cyclic wall strains in the murine model. We then aim to demonstrate that a relationship exists between cyclic strain and IH. Finally, we aim to determine the detailed temporal changes in both cyclic strain and IH and demonstrate that changes in cyclic strain precede IH formation in this model.

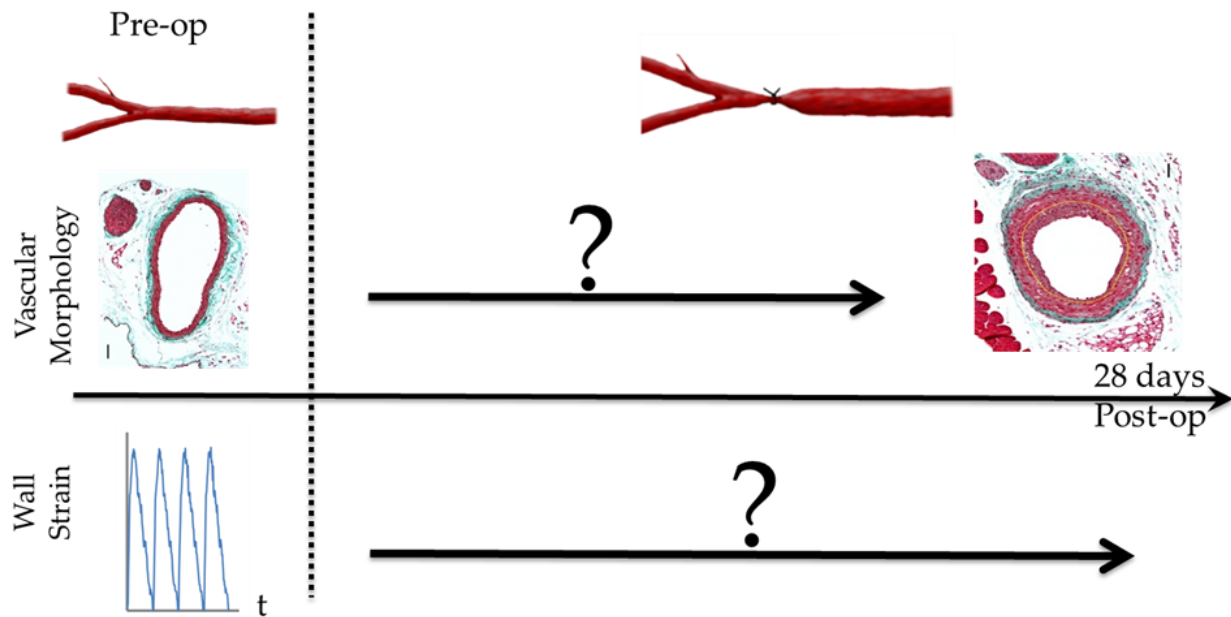


Figure 1-2: Overall hypothesis of this dissertation. We hypothesize that, using a murine model of IH, we can demonstrate that reductions in cyclic circumferential wall strain temporally precede the formation of IH in the corresponding region of the vessel.

1.3 Specific Aim I: Develop and apply a noninvasive, ultrasound-based method for measuring mechanical strain in the murine vasculature

Recent developments in high frequency ultrasound technology have considerably improved both the spatial and temporal imaging resolution of ultrasonography systems, allowing researchers to accurately measure luminal diameter *in vivo* in mice.^{38, 39} Simultaneously, improvements in speckle tracking technology in ultrasound imaging has allowed for objective quantification of both myocardial strains and strain rates in small animal models.⁴⁰⁻⁴³ In this Aim, we propose that the combination of high frequency ultrasound and speckle tracking algorithms can be used to quantify and assess mechanical strains on the murine arterial wall *in vivo*.

1.3.1 Objective 1A: Validate an ultrasound-based strain measurement technique

A number of measurement techniques have been applied to measuring strains on the arterial wall both *in vitro* and *in vivo*. Given that we eventually aim to apply our strain measurement technique to an *in vivo* murine model, the technique must be both noninvasive and have a large enough spatial resolution to resolve changes in diameter of vessels on the micron scale.⁴⁰ High frequency ultrasound meets both of these requirements. In this objective, we used telecentric optics to accurately and dynamically measure the diameter of an *in vitro* murine artery phantom. Simultaneously, we measured strains using our novel ultrasound-based method and demonstrated that we produce similar results with both techniques.

1.3.2 Objective 1B: Apply the ultrasound based method *in vivo* in a murine model of vascular disease

Although IH remains the overall focus of this study, the development of a non-invasive, high resolution strain measurement method for *in vivo* studies would be beneficial to the study of a number of vascular diseases. In this objective, we chose to apply our novel ultrasound technique to a murine model of abdominal aortic aneurysm (AAA) formation. In this objective, we hypothesized that high-frequency ultrasound scan biomicroscopy combined with speckle-tracking can be used to define the role of oscillatory wall strain in AAA formation in defined aortic anatomic regions in the Angiotensin II apolipoprotein-E deficient mouse model of AAAs. The results of this objective demonstrate the utility of our novel ultrasound method and showed that it can be effectively applied to mouse models of arterial disease.⁴⁴

1.4 Specific Aim II: Evaluate if a relationship exists between oscillatory wall strain and intimal hyperplasia formation

In Specific Aim I, we validated the measurement accuracy and precision of our ultrasound strain measurement technique and demonstrated that it can be effectively applied to a living

model of arterial disease. In Aim II, we apply this method to a novel model of arterial intimal hyperplasia and examine how dynamic mechanical strain relates to IH.

In a previous study in our collaborating lab, we have demonstrated a novel, technically simple, model of IH formation in the mouse.³⁷ In this model, a focal stenosis is created on the murine carotid artery. In the resulting publication detailing this method, we showed that immediately after creation of the focal stenosis, wall shear stress and cyclic wall strain were significantly reduced in the artery proximal to the stenosis. In objective 2, we combine this novel model with our ultrasound-based strain measurement method to better understand the relationship between cyclic strain and IH formation in the mouse.

1.4.1 Objective 2: Determine what relationship exists between mechanical strain and pathological wall remodeling

In order to assess the relationship between IH and cyclic strain, in objective 2 we used the ultrasound strain measurement technique validated in Aim I to assess cyclic strains in the region proximal to the stenosis pre-operatively and at day 27 after focal stenosis. We then collected arterial tissues for histological analysis at day 28. In this objective, we demonstrate that when we create a focal stenosis in our mouse model, we induce the formation of IH and the complete occlusion of ~30% of arteries by 28 days post-surgery. In this objective, we discovered that there was a relationship between cyclic strains measured at day 27 and IH at day 28. The existence of this relationship suggests that changes in mechanical strain may play an underlying role in the processes that eventually result in IH formation.

1.5 Specific Aim III: Determine if changes in oscillatory wall strain precede formation of intimal hyperplasia *in vivo*

In Specific Aim II, we provide evidence that a relationship exists between acute changes in mechanical strain and IH formation at the ~1 month time point in our murine model. In the final

objective of this dissertation, we seek to more clearly define this temporal relationship and to delineate exactly when both cyclic strain and IH formation occur in this model

1.5.1 Objective 3A: Determine the temporal progression of wall strain in the focal stenosis model

In the objective 3A experiment, we use data collected from the animals in Objective 2 to assess changes in strain at just 4 days post-op. Regional reductions in oscillatory wall strain were quantified at day 4 and compared to histological outcome at day 28. Relationships between early changes in mechanical strain and eventual IH

1.5.2 Objective 3B: Determine the temporal progression of intimal hyperplasia in the focal stenosis model

In objective 3B, we will use an additional *in vivo* study in our mouse model of intimal hyperplasia. In this study, IH was assessed just 4 days after creation of the focal stenosis to both validate that strain reductions occur and to determine if morphological changes or IH are visible at day 4.

2 Background

2.1 Introduction

2.1.1 The cardiovascular system

The cardiovascular system serves as the primary nutrient and waste transport system in the body. It is responsible for carrying oxygen, nutrients and hormones to the body's tissues and removing carbon dioxide and other wastes. The cardiovascular system is composed of two primary components: the heart and the blood vessels. The heart is an electromechanical pump which continually beats throughout a person's life. With each beat, the heart creates pressure gradients which in turn force blood into the vascular system.⁴⁵

The vascular system is a system of tubular blood vessels which transfer blood to and from the body's tissue with each heartbeat. Although often simplified and considered a system of pipes that transports blood, the vasculature is a complex, living and changing system that varies considerably in the body in different anatomic locations. Blood vessels are composed of three different layers, each of which functions to maintain vascular homeostasis.

2.1.2 Vascular structure

The outermost layer of the blood vessel is the adventitial layer. This layer primarily functions to reinforce the vessel and to anchor it to surrounding tissues. The adventitia is composed mostly of interwoven collagen fibers and is infiltrated with fibroblasts.⁴⁶ The high collagen content of the adventitia plays a role in preventing vascular rupture at high pressures.⁴⁷ Additionally, in larger blood vessels, the adventitia can contain a network of smaller blood vessels (the vasa vasorum) which supply nutrients to the vessel wall, which is too distant to obtain nourishment from the vessel lumen.⁴⁵ The vasa vasorum is seen primarily in larger mammals and is not found in small mammals such as mice.⁴⁶

Just inside of the adventitial layer is the external elastic lamina, which is a fenestrated, circumferentially oriented sheet of elastin. Throughout the medial layer of the blood vessel, these elastic laminae occur alternately in the radial direction with layers of vascular smooth muscle cells (SMCs) and proteoglycan rich extracellular matrix (ECM).⁴⁶ Thin fibers of elastin intersect the SMC layers connecting the lamina and forming a continuous three dimensional network throughout the vessel.⁴⁸ Although the number of lamina in the arteries of a given animal may vary greatly throughout the vascular system, the average tension per lamellar unit falls into a surprisingly narrow physiological range, suggesting that lamellar tension is physiologically maintained across vessels of different sizes and even across many mammalian species.^{32, 49, 50} This concept is further supported by studies demonstrating that removal of SMC function in the adult artery does not reduce the static mechanical properties of the vessel.⁵¹ This suggests that the mechanical properties of the vessel are mainly due to the collagen and elastin fibers in the media and are not due to SMC muscle tone.⁴⁶

On the inside of the innermost elastic lamina, or internal elastic lamina, is the intimal layer of the blood vessel. In the healthy artery, the intimal layer is typically formed of a monolayer of endothelial cells which produce and attach to a basal lamina that is supported by the internal elastic lamina.⁴⁶ In some larger animals, including humans, the healthy intimal layer also contains some SMCs in addition to the underlying basal lamina.⁵²⁻⁵⁴ Although the intimal layer does not contribute significantly to vascular mechanics,⁵⁵⁻⁵⁷ it does play an important role in maintaining vascular homeostasis. The intimal layer forms a barrier between the blood and the underlying basal lamina. Denudation of the endothelial layer results in local protein adsorption from the blood stream and can eventually result in thrombosis. In addition to its barrier

function, the intimal layer also plays an important role in mechanosensation of flow through the blood vessel and provides molecular cues that control SMC tone in the medial layer.⁵⁸⁻⁶¹

The layers of blood vessels can be clearly observed using histological staining techniques and biomicroscopy. Masson's trichrome stain differentiates the layers of the arterial wall clearly by staining the elastic lamina bright red, the vascular smooth muscle cells red, the collagenous fibers in the adventitia blue and the nuclei black. Figure 2-1 shows a Masson's Trichrome stain of the healthy murine carotid artery. Although all blood vessels are composed of adventitial, medial and intimal layers, the size and structure of these three layers vary considerably throughout the vascular system. The vascular system can be broadly divided into 3 separate types of blood vessels: arteries, capillaries and veins. Arteries are the first conduits in which blood travels as it exits the heart. Arteries are typically large, muscular vessels which are conditioned to withstand the high, pulsatile pressures created by the beating heart. The largest artery, the aorta, is the first vessel which comes off of the heart. As blood travels through the vasculature from the heart, it is branched into arteries and arterioles, which eventually branch into capillaries. Capillaries are typically formed of only a monolayer of endothelial cells and allow for nutrient transport to the surrounding tissues. After leaving the capillaries, blood flows into the venules and then into the larger veins before returning to the heart. Given that blood pressures and flow rates through the different types of blood vessels differ considerably throughout the vascular system, the relative compositions of the three different vascular layers also vary by vessel type.

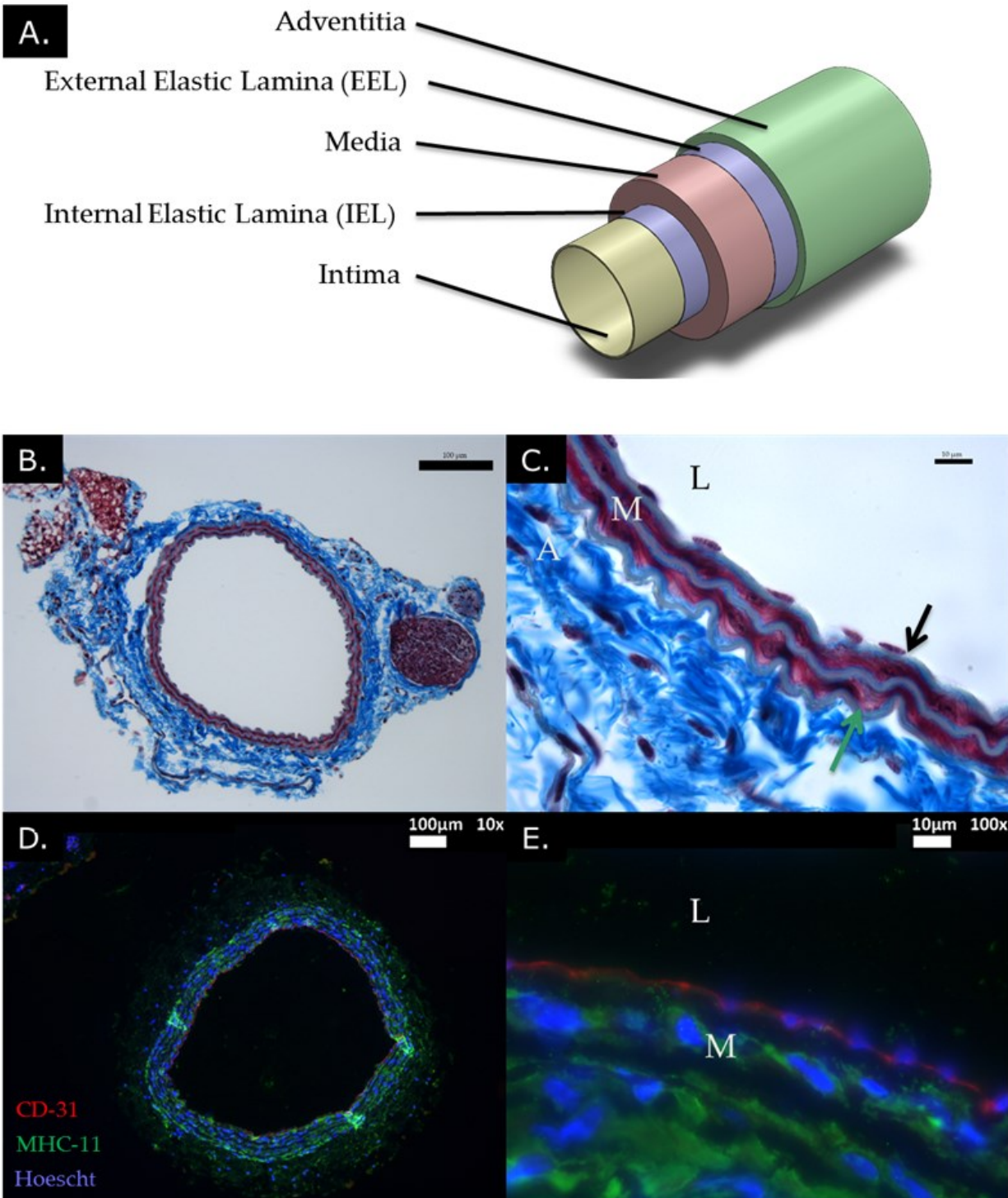


Figure 2-1: Structure of the healthy artery. (A) Schematic of the different layers of the blood vessel. (B) Masson's trichrome stain of a full carotid arterial cross-section in a healthy adult mouse carotid artery. (C) A high magnification image of the arterial wall showing the internal (black arrow) and external (green arrow) elastic laminae. (D) Immunohistochemical stain of a full mouse arterial section stained for endothelial lining (CD-31, red), smooth muscle cells (myosin heavy chain, green), and nuclei (Hoechst 33342, blue) L represents the vessel lumen, M represents the medial layer and A represents the adventitial layer. (E) 100x magnification image of vessel wall from D.

2.1.3 Mechanical forces on the vessel wall

In addition to having a structure targeted at withstanding mechanical forces in their respective locations in the body, many blood vessels also actively react to changes in blood pressure and flow to maintain homeostasis. In particular, blood vessels have been shown to sense and react to two different forces: hemodynamic luminal shear stress and wall tensile stress. Figure 2-2 shows the major forces applied to the blood vessel.

Hemodynamic shear stress is the shear force applied to the endothelial cells in the vessel lumen by the flow of blood through the vessel and can be computed using Equation (2-A). The majority of research assumes that the blood has a constant viscosity and therefore can be considered as a Newtonian fluid.⁶²⁻⁶⁹

$$\tau(u) = \mu \frac{du}{dy} \quad (2-A)$$

Using advanced mechanical modelling techniques, the non-Newtonian properties of blood can be included in shear stress analysis. These techniques demonstrate that Newtonian assumptions can grossly underestimate average wall shear stress on the wall and overestimate the maximum shear stress.⁷⁰ Despite this evidence, limitations in data available in most *in vivo* studies force most researchers to continue using Newtonian fluid assumptions.

Vascular endothelial cells are equipped to sense and respond to the luminal shear forces applied to them. A number of cell surface receptors, ion channels and the cell cytoskeleton have been shown to specialize in mechanotransduction of wall shear.⁷¹ Under normal physiological conditions, steady laminar blood flow generates, on average, a shear stress of approximately 15 dynes/cm².⁷² When sensing this physiological level of shear, endothelial cells release nitric oxide

and other chemical mediators which maintain medial SMCs in a quiescent state and promote vasodilation of the vessel wall.⁷³

Similarly to hemodynamic shear stress, tensile stress in the vessel wall has also been shown to be maintained homeostatically in the healthy artery.⁷⁴ Tensile stress is most simply defined as the force per unit cross-sectional area acting on a given surface. In three dimensions, stress is represented as a 2nd order tensor with 6 independent stress components representing the force per unit area on the sides of a volume element. In the arterial wall, this tensor is typically defined in cylindrical coordinates with 3 normal components and 3 shear components. The normal components of arterial stress are circumferential ($\sigma^{\theta\theta}$), longitudinal (σ^{ll}), and radial (σ^{rr}) stress and the shear components are $\sigma^{r\theta}$, $\sigma^{l\theta}$, σ^{lr} . (Normal stresses are shown in Figure 2-2) Under a given mechanical stress, the blood vessel will deform until the forces within the vessel reach equilibrium.

Mechanical strain is a measure of the distortion of the vascular wall. Although there are a number of mathematical definitions of strain,⁷⁵ the most commonly used definition in the literature for blood vessels is the Green (Lagrangian) strain tensor. For this reason this definition will be used throughout the rest of this dissertation. Like wall stress, strain is also a 2nd order tensor with 6 independent components. Strains in the vessel wall due to the internal blood pressure are limited to the strains in the normal directions: radial strain, longitudinal strain and circumferential strains. Although others have assessed radial⁷⁶ and longitudinal⁷⁷ strains, experimental data⁷⁷ shows that circumferential strains in blood vessels are larger than the other strain components. For this reason, we focus solely on circumferential strains for the remainder of this dissertation. In Green's definition of strain, the deformation of a body is

determined as the change from a reference configuration to a final configuration using the starting configuration as the reference point. Optimally, the reference configuration for strain is defined as the point where the body is under no stress. Defining this configuration in the artery is complicated by the fact that arteries under no external forces still having residual stresses internally.⁷⁸ This is further complicated *in vivo* where the external forces (i.e. blood pressure) are never zero. Therefore, in this dissertation, we will measure oscillatory wall strain. This strain is defined using the vessel at diastole as a reference configuration and the vessel at systole as the final configuration. Although this definition provides no information about the absolute strain state of the vessel wall, it does measure how much strain is being applied to the vessel wall cyclically with each cardiac cycle and is easily measured *in vivo*.

Since wall stress and wall strain are intimately related through the mechanical properties of the vessel wall, wall strain has consequently been implicated as a mediator of vessel homeostasis in addition to wall stress.^{33, 79} *In vitro* studies have demonstrated that both vascular SMCs and vascular endothelial cells respond to changes in cyclic stress/strain independently of wall shear stress.⁸⁰ This suggests that shear stress and strain mechanosensation pathways independently contribute to changes in wall composition seen during neointima formation. Together with shear stress mechanotransduction mechanisms, the vascular wall is able to maintain a homeostatic level of internal pressure and luminal flow.

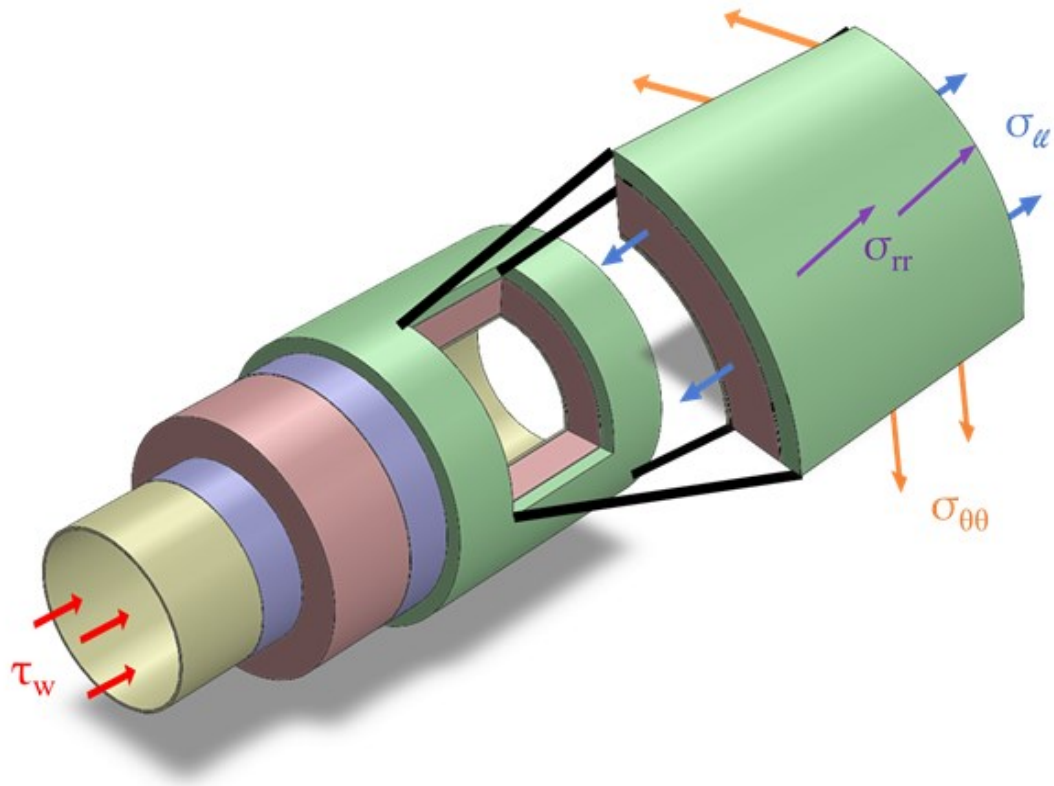


Figure 2-2: Forces applied to the blood vessel wall *in vivo*. The arterial wall is subjected to 4 primary forces *in vivo*: wall shear stress (τ_w , red arrows), longitudinal stress (σ_{ll} , blue arrows), radial stress (σ_{rr} , purple arrows) and circumferential stress ($\sigma_{\theta\theta}$, orange arrows).

2.2 Vascular disease

In this dissertation, we aim to unravel relations between vascular mechanics and intimal hyperplasia. In order to fully describe the importance of these relations, we must first examine the known relationships between vascular mechanics, IH and vascular disease currently described in the literature. In the following sections we will discuss these relationships.

2.2.1 Relation between intimal hyperplasia and vascular disease

Despite extensive research and funding, cardiovascular diseases remain the number one cause of death in first world countries.¹ Although a number of pathologies underlie cardiovascular diseases, many pathologies begin with occlusion of the arterial lumen via arteriosclerosis. Pathologies affected by arteriosclerosis include myocardial infarction, stroke,

and many others. Arteriosclerosis is characterized by the progression from intimal thickening, to inflammatory response, and finally to the formation of fatty streaks and atherosclerotic plaques.³ One of the major factors that initiates the formation of arteriosclerotic plaques is IH,³ and a number of researchers have demonstrated that mechanical forces underlie the propagation of intimal hyperplastic lesions.^{14, 26, 81-85}

Intimal hyperplasia (IH) can be defined as the proliferation of cells in multiple layers internally to the internal elastic lamina. Further, IH cells are observed to express α SMA either permanently or temporarily.³ Others add that the term IH should be reserved for tissues that are both proliferative and without common orientation or clear organization. Cells in IH tend to be spread out with abundant matrix and few, if any, collagen or elastin fibers.¹³ Although IH is typically considered to be a completely pathological response, there are some cases in which IH occurs during healthy physiology. The most commonly referenced cases of this non-pathological IH are the closing of the ductus arteriosus and the closure of umbilical arteries.⁸⁶ Others also report a benign form of IH in the healthy artery. This benign IH has a similar appearance to that of pathological IH but does not significantly reduce lumen area or flow.^{53, 54} Given that the underlying causes of IH and the relation between pathological and benign IH remain unclear, the connection between IH and disease is an important field of study with widespread impact on vascular disease.

In vivo, IH is a precursor and the primary underlying cause for a number of vascular diseases and the subsequent failure of many vascular surgical interventions. Atherosclerosis, the stiffening and stenosis of the artery due to plaque formation, has been shown to occur in regions of preexisting intimal hyperplasia.⁸⁷ Atherosclerotic plaques can go on to cause luminal

narrowing, and eventually the total blockage of the arterial lumen.⁸⁸ Blockage of blood flow results in distal organ ischemia, and eventually cell death. This IH-initiated pathway has been shown to contribute to a number of diseases including stroke,⁸⁹ coronary artery disease,^{6, 86} peripheral artery disease,⁹⁰ and restenosis after a number of clinical interventions.^{6, 8, 13} The following sections of this dissertation will delineate the current literature that relates mechanical forces to biological outcome in intimal hyperplasia.

2.2.2 Relation between Wall shear stress and vascular disease

Blood flow through the healthy artery *in vivo* is typically laminar and maintains a time-averaged shear stress on the vascular endothelial cells of 10-15 dynes/cm² (1-1.5 Pascals).⁹¹ Regions of low wall shear stress and oscillatory flow have been positively correlated with IH *in vitro*²⁵ and *in vivo*,⁹² while high levels of laminar blood flow (shear stress) results in decreased IH formation.⁶⁶ Additionally, increases in blood flow in vessels with preexisting IH can induce regression of IH.⁸² Although high blood flow is typically considered atheroprotective, extremely high shear stresses have also been associated with IH formation.⁹³

Given that, in the arterial circulation, shear stress constantly changes as the heart cycles between diastole and systole, it is necessary to clearly define what “low shear stress” means. Typically, low shear stress in the arteries refers to shear stress with a time average magnitude of less than about 10 dynes/cm² ^{92, 94} but can refer to larger or smaller values depending on the arterial conditions or species.^{59, 95} A number of *in vitro* studies have demonstrated that endothelial cells can sense and respond to changes in hemodynamic shear stress. Of the many biological changes caused by changes in hemodynamic shear stress, the most commonly cited is the nitric oxide (NO)/endothelial nitric oxide synthase (eNOS) pathway.^{59, 82, 96-103} *In vitro*, it has

been demonstrated that increases in applied shear stress results in increases in NO production in arterial endothelial cells.¹⁰⁴ NO has also been shown to prevent vasoconstriction of vessels in the microcirculation suggesting that it both causes vasodilation and reduces the effects of vasoconstrictors.¹⁰⁵ Colotti *et al.* demonstrated that treatment of IH-prone vessels with nitric oxide (NO) reduces IH production in an *ex vivo* model.¹⁰⁶ Further, *in vivo* studies have demonstrated that local release of NO can reduce intimal hyperplasia in both the IH-prone artery and the stented artery.^{107, 108}

Although extensive research has demonstrated the importance of the NO/eNOS pathway in effecting vasodilation after changes in wall shear stress, the mechanism by which the endothelial cells actually sense shear stress still remains unclear.¹⁰⁹ One hypothesis to date involves mechanosensation of fluid shear via torque applied to the endothelial glycocalyx. The glycocalyx is a carbohydrate rich layer of molecules that lines the outside of the cell membrane.⁴⁵ A number of recent studies suggest that endothelial sensation of torque on the glycocalyx results in changes in cell membrane permeability which therefore results in release of NO molecules.¹⁰⁹⁻¹¹¹

2.2.3 Relation between wall tensile stress and strain and vascular disease

In addition to the wall shear stress applied to endothelial cells, the vessel wall is also cyclically exposed to mechanical strain and stress in both the circumferential and longitudinal directions with each cardiac cycle.¹¹² Although mechanical strain is fundamentally different from mechanical stress, the close relationship between the two parameters makes it difficult to separate their effects.

Although this stress is applied to the endothelial cells of the intima, the majority of the stress is supported by the SMCs of the medial layer. Although the exact mechanisms of stress mechanotransduction remain unknown, a plethora of research demonstrates that stress and/or strain mechanotransduction plays a role in vascular disease. Evidence shows that increases in intraluminal pulse pressure (and therefore stress and strain) result in compositional changes in the blood vessel wall.^{50, 113} Additionally, excessive mechanical stretch can result in SMC hypertrophy,^{114, 115} localized inflammatory reactions and degradation of wall structural elastin and collagen.¹¹⁶ All of these changes could contribute to changes in wall structural properties.

Reductions in mechanical stretch also yield changes in SMC phenotype. One study demonstrated that reducing circumferential strains applied to arteries *in vitro* resulted in SMC proliferation and increased production in inflammatory cytokines.¹¹⁷ These correlations suggest that vascular cells sense changes in both shear stress and tensile stress (and/or strain) and react to changes in their mechanical environment.

Some research suggests that the arterial wall actively maintains a homeostatic level of wall stress.^{31, 59, 118} This theory is supported by the observation that the number of lamellar units in any given artery is proportional to blood vessel diameter across a number of mammalian species.³² By maintaining this relationship, the vascular wall keeps the mechanical tension per lamellar unit within an amazingly narrow physiological range.

Compared to the well-established effect of shear stress, the impact of wall strain on the development of intimal hyperplasia is much less defined, and thus the focus of the current proposal. From a mechanical standpoint, the artery can be considered a composite structure with three mechanically unique layers. Given that the intima in the healthy artery is typically

only one cell layer thick, it is generally considered to not contribute to healthy arterial wall mechanics.^{119, 120} Previous studies have examined the different contributions of the arterial wall layers to wall mechanics in both the healthy¹²⁰ and diseased arteries.¹²¹ These studies demonstrated that the material properties vary significantly amongst the three layers¹²⁰ and that the mechanical properties of the intimal layer can contribute significantly to mechanical properties after pathological neointima formation has occurred.¹²¹

Smooth muscle cells are the most prominent cell type in the blood vessel and therefore are the cells that are affected most by cyclic strains. A number of studies have demonstrated relationships between oscillatory strains and biological changes in vascular SMCs. *In vitro* studies have demonstrated that oscillatory strains result in increases in SMC synthesis of collagen¹²²⁻¹²⁴ and elastin as well as glycosaminoglycans (GAGs) such as versican and hyaluronic acid.^{14, 80, 125} Further, studies have shown that the magnitude of ECM and GAG synthesis by SMCs are dependent upon strain magnitude, strain frequency and time in culture.⁸⁰ Recent *ex vivo* studies have proposed that mechanical strain works independently of the wall shear stress to cause intimal hyperplasia.^{126, 127} Cyclic strain has been shown to cause structural and compositional changes in both the endothelial and smooth muscle cells of vein grafts.^{128, 129} Evidence *in vivo* suggests that wall strain correlates positively with intimal thickening.^{73, 130} In the cell culture setting, mechanical stretch activates several pathways capable of regulating smooth muscle cell phenotype,^{131, 132} but biologic information in the *in vivo* setting is limited. This dearth of mechanistic knowledge into links between strain and intimal hyperplasia is largely the result of limited capabilities in the measurement of strain in the intact animal.

2.3 Techniques for measuring vascular mechanics *in vivo*

Although a large quantity of research has been completed to characterize *in vitro* cellular reactions to mechanical stresses and strains, true clinical relevance is best realized through *in vivo* research in animal models and in the clinic. A major hurdle that must be overcome is the need to accurately and consistently measure mechanical stresses and strains *in vivo*. Optimum measurement of mechanical stresses and strains *in vivo* would include non-invasive approaches that have limited effects on animal physiology. The problems associated with *in vivo* studies are exacerbated in small animal models of vascular disease, such as the mouse, because of the small size of rodent vasculature. In this section, we will discuss different methods that are used to measure mechanics *in vivo* in both animal models and humans

2.3.1 Measurement of wall shear stress

Wall shear stress measurements *in vivo* are typically made using either MRI or ultrasound-based of blood flow through the blood vessel. Ultrasound approaches use either transit time of an ultrasound pulse through the vessel to determine bulk blood flow velocities¹³³ or use the Doppler effect to determine local average blood velocities¹³⁴. Others utilize phase-contrast MRI-based measurements to estimate wall shear stress from flow rates.¹³⁵ Of these two methods, ultrasonography provides both higher spatial and temporal resolutions.¹³⁶

The simplest approach to measuring flow velocities using ultrasonography is the use of transit-time flowmeters to measure bulk flow through the blood vessel. Transit-time flowmeters are limited in that they require that the vessel be exposed in order to measure the flow through the vessel. From bulk flow measurements, it is possible to estimate shear stress at the vessel wall using equation (2-B) below where τ is shear stress, μ is the dynamic viscosity of blood, Q is the volumetric flow rate, and d is the vessel's diameter:

$$\tau = \frac{32\mu \cdot Q}{\pi \cdot d^3} \quad (2-B)$$

This formula assumes that the blood has a fully developed, laminar and parabolic flow profile. Additionally it assumes that the blood has constant dynamic viscosity (typically ~3.3 cP)³⁷ and that the vessel has a constant, circular cross-section. Although these assumptions may be accurate enough to calculate time average shear stresses in a healthy blood vessel, they vastly underestimate the shear stresses due to pulsatile flow and non-laminar flow profiles.

Continuous wave Doppler ultrasound has been used extensively to quantify changes in blood flow in humans for over 30 years.¹³⁷⁻¹³⁹ This approach, based on the Doppler Effect, continuously transmits and receives sound waves through the blood vessel wall. The frequency shift of the sound waves received by the transducer compared to those sent are related to the velocity of blood flow through the vessel. The primary limitation of this approach is that it provides no information about where in the ultrasound field of view the measured flow is occurring. Additionally, it is not possible to simultaneously measure continuous-wave ultrasound data and collect ultrasound images, making it even more difficult to interpret flow measurements.

In order to overcome some of the issues associated with continuous-wave Doppler ultrasonography, pulsed-wave Doppler ultrasonography was developed. Pulsed wave Doppler ultrasonography differs from continuous-wave ultrasonography only in that brief pulses of ultrasound wave are emitted. Based on the timing of these pulsed waves and the known speed of sound in tissue, pulsed-wave Doppler made it possible to determine the location of flow velocities. This finding also allows for the use of duplex ultrasound where Doppler velocity

flows and B-mode ultrasound images are simultaneously collected. Even with pulsed-wave Doppler ultrasonography, the method by which shear stress is calculated is limited by a number of assumptions. With both pulsed-wave Doppler, wall shear stress is typically computed based on the maximum velocity (V_{\max}):

$$\tau = \frac{4 \cdot \mu \cdot V_{\max}}{d} \quad (2-C)$$

This formula once again makes the same assumptions as that used for transit-time flowmeters. As a result, it is prone to substantial errors that may cause it to underestimate differences in regional shear stress.¹⁴⁰ Despite these limitations, a number of clinical studies utilize Doppler ultrasound shear stress calculations for both research and diagnosis.¹⁴¹⁻¹⁴³

2.3.2 Measurement of wall tensile stress

Unlike hemodynamic shear stress, tensile stress in the vascular wall cannot be measured based on blood flow. Rather, the most relevant physical method of estimating tensile stress in the vascular wall is through use of pressure measurements. The most simplistic approach to estimating wall stresses is the use of Laplace's law and assuming the artery is a thin walled cylindrical pressure vessel with constant thickness and homogeneous mechanical properties.^{36, 144} To better estimate wall stresses, it is often necessary to constitutively model the blood vessel.^{78, 145} Although constitutive modelling is not a direct method of measuring wall stresses *in vivo*, it can be made to be patient specific by combining 3D imaging (such as MRI or CT scans) with blood pressure measurements. Combining these two measurements into one computer model can provide data about mechanical stresses for a specific artery.^{146, 147} Given that

computational modelling is time consuming, and requires that a number of assumptions be made about arterial mechanics,¹⁴⁵ it may not be the best *in vivo* measure of wall mechanics.

2.3.3 Measurement of wall strain

Wall tensile stress is directly related to tensile strain in the vessel wall through the mechanical properties of the arterial wall. Given that a number of studies have demonstrated that the mechanical properties of the arterial wall can be changed in the diseased state,^{55, 148, 149} it is reasonable to assume that there will be changes in *in vivo* wall stresses and strains due to changes in wall mechanics. Relative to measuring wall tensile stresses *in vivo*, measurement of wall strains is comparatively easy. In order to measure wall strains, it is generally necessary to define a zero strain state from which strains will be measured. Ideally, the zero strain state would be defined with the vessel under zero pressure. Since it is not possible to measure the arterial diameter under zero pressure *in vivo*, the zero strain state for most *in vivo* studies is typically defined as the state of the vessel at diastole.¹⁵⁰

A number of approaches have been used to measure wall strains *in vivo*. In humans, MRI, and both external and intravascular ultrasound have all been used to estimate oscillatory wall strains.^{148, 150-152} MRI has been used in humans to measure circumferential strains in both the carotid artery¹⁵³ and the descending thoracic aorta.¹⁵⁴ Others have reported using MRI to measure carotid strains in the mouse, but EKG gating must be used to overcome temporal resolution limits.³⁵

Ultrasound has been used in humans to assess mechanical strains in a number of studies. In the majority of these studies, speckle tracking algorithms are applied to longitudinal B-mode images of arteries and displacements in each direction are computed. From these displacements,

average strains can be determined.¹⁵⁰ Use of longitudinal B-mode views provides robust data for accurate calculation of average strains but does not allow for regional strain measurement. Others have used external ultrasound to measure cross-sectional diameters in humans and estimate strains based on diameter changes.¹⁵⁵ Use of cross-sectional ultrasound images allows for the measurement of circumferential strains in a specific arterial region but is hindered by changes in probe angle.

In rodents, measurement of vascular strains is more difficult due to the small size and fast heart rates of mice and rats. These conditions require methods with significantly higher spatial and temporal resolutions than is necessary in humans. Goergen *et al.* reported using MRI to measure aortic strains in the mouse with sufficient spatial resolution and using EKG gating to overcome temporal resolution limits.³⁵ Others have reported using longitudinal ultrasound images to measure strains in the mouse.¹⁵⁶ Newer ultrasound systems used primarily in the cardiac literature now report spatial and temporal resolutions that are sufficient to accurately image cardiac cycles in the mouse.^{40, 157} As discussed in section

2.4 Summary

A plethora of studies have demonstrated that vascular cells respond to changes in their mechanical environment^{46, 126, 128, 158, 159} and that these changes in mechanical environment can induce pathological changes in the vessel wall.^{36, 121, 155, 160} Although the majority of previous work focuses on endothelial mechanosensation of wall shear stress^{25, 83, 93, 98, 100, 101, 161-165}, evidence suggests that changes in wall shear stress alone do not fully explain the phenomenon of neointimal formation.^{27, 28} Herein, we focus on the relationship between cyclic deformation of the arterial wall and the eventual intimal hyperplastic outcome in a murine model. By defining

a relationship between noninvasively determined oscillatory wall strains and intimal hyperplasia, we will develop a better understanding of how changes in arterial mechanical environments relate to vascular disease.

3 Objective 1A: Validation of ultrasound strain measurement

3.1 Introduction

Ultrasound has emerged as a tool to enhance understanding of vascular diseases in both the clinical^{166, 167} and research setting.¹⁶⁸⁻¹⁷² One of the most commonly employed models is the murine model, due to its well-defined genome and relatively low cost. Recently, high-frequency ultrasound imaging systems (e.g. Vevo 2100, FUJIFILM Visualsonics, Toronto, ON, Canada) have been developed to noninvasively micro-image mice *in vivo*, and such approaches can reliably detect and measure the mouse aortic diameter *in vivo*.^{38, 39} At the same time, speckle-tracking technology in ultrasound imaging has emerged as a quantitative, objective technique to accurately evaluate myocardial function and dynamics. Speckle tracking functions by tracing the displacement of speckles during the cardiac cycle to measure strain and strain rate,⁴⁰⁻⁴³ and it has been used in the assessment of mouse models of cardiac dysfunction.¹⁷³ In this chapter, we aim to validate a novel system for measuring wall strains noninvasively using an *in vitro* phantom model.

A number of previous studies have employed *in vitro* phantoms of the artery to test novel ultrasonic measurement methods for both flow and a number of vascular disease analyses.^{150, 174-177} Although these different phantoms vary in complexity, the simplest of them are composed of a piece of tubing suspended in a hydrogel solution. A pressure gradient or cyclic flow waveform is created within the tube which can be used to evaluate the ability of ultrasound to measure flow or other properties within the vascular phantom. More complex phantoms include highly sophisticated pulsatile flow pumps and harvested blood vessels with real blood flow through the lumen. Since the goal of this objective is to demonstrate that ultrasound strain measurements using our novel approach have similar results to those found using other

methods, we will use an extremely simple silicone tube model of a blood vessel with precisely defined dimensions.

To provide a benchmark measurement for the strains measured using ultrasound, we will employ a high speed camera system with telecentric lenses to simultaneously measure the strain of the tube. Telecentric lenses are widely used in machine vision to measure the dimensions of products during manufacturing. In a typical camera lens system, the magnification of the system is modified significantly due to changes in focus setting¹⁷⁸ and distance of the lens from the object.¹⁷⁹ This property of traditional camera lenses can distort images recorded with a camera causing images to inaccurately represent the size of objects in the camera field.¹⁸⁰ One approach to overcoming lens distortion is to use telecentric lens systems. Telecentric lenses create nearly orthographic projections of objects being imaged in the image plane. This means that objects that are in focus and those that are out of focus will still be projected at their actual size. Telecentric optics creates a distinct advantage in optical measurement methods because they minimize measurement error due to the perspective distortion. In conjunction with telecentric lenses, we used high density mapping (HDM), an optics-based measurement approach that we previously developed to determine regional displacements in a number of biological tissues.^{37, 181-183} In this objective, we will first demonstrate the accuracy of HDM by comparing HDM strain measurements with sonomicrometry, then validate our ultrasound-based method against HDM.

3.2 Materials and methods

3.2.1 Validation of High Density Mapping against sonomicrometry

Sonomicrometry has long been considered a gold standard for distance measurement in medical displacement and strain analyses.¹⁸⁴ To test the ability of HDM to measure strains, two

sonomicrometry crystals were attached to a 2 inch piece of ¼ inch I.D. Penrose tubing (Penrose drain, Cardinal Health, McGaw Park, IL). This tubing was attached to a syringe pump and oscillatory pressure gradients were created in the closed system to simulate oscillatory wall strains. Displacements were simultaneously measured via two 2mm sonomicrometry crystals sutured to the tubing surface (Triton, San Diego, CA) and a high speed camera (Fastcam 1280pci, Photron USA, San Diego, CA) connected to a telecentric lens (486mm precision telecentric lens, Computer Optics Inc., Hudson, NH). Displacements from the optics system were computed using HDM¹⁸¹ and oscillatory wall strains were computed using both methods. Average strain magnitudes across several cycles were calculated. Simultaneously recorded strains from the cycles were compared using a paired t-test. A sample image used for HDM analysis is shown in Figure 3-1.

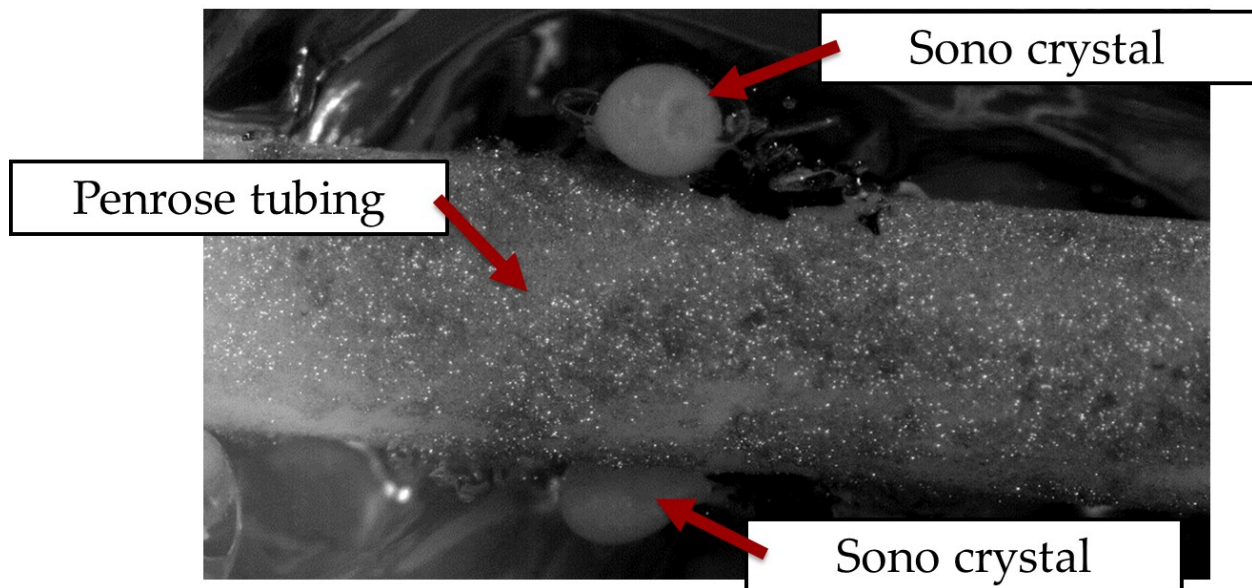


Figure 3-1: Comparison of sonomicrometry and HDM strains. Two sonomicrometry (sono) crystals were sutured to the wall of Penrose tubing. HDM speckle tracking was used to simultaneously determine strains.

3.2.2 Development of an *in vitro* model of pulsatile pressure

Given that ¼ inch Penrose tubing is much larger than the size of blood vessels analyzed in the remainder of this dissertation, ultrasound-based measurement of strain was validated using a small diameter silicone tube. Given that the smallest available sonomicrometry crystals are larger than our tubing phantom, validation of ultrasonography was completed using HDM and not sonomicrometry. In order to complete this validation, we first aimed to create an *in vitro* model of arterial pulsatile pressure. Using similar methodology to previous ultrasound vascular phantoms,^{150, 174-177} a small diameter (1.473 mm I.D.; 1.956 mm O.D., SMI Manufacturing, Saginaw, MI) silicone tube was securely attached to two 1/8 inch barbed connectors. One side of the tubing was connected to a 60 mL syringe (Figure 3-2). The tubing was cleared of air bubbles and the system was closed using a luer valve. The tubing was speckled using a 50:50 mix of silicon carbide microparticles (Silicon carbide 400 grinding compound, Alfa Aesar, Ward Hill, MA) and reflective paint (Scotchlite Reflective Ink 8017, 3M, St. Paul, MN) to create a unique light intensity distribution across the tubing surface. The tubing was secured to a custom optics rig and covered with optically clear ultrasound gel (Aquasonic Clear, Parker labs, Fairfield, NJ). A large glass coverslip was pulled back against the ultrasound gel and bubbles were removed using cotton swabs yielding a flat, undistorted view of the tubing. A telecentric lens and camera were then attached to the optics rig and the camera axis was aligned perpendicular to the coverslip.

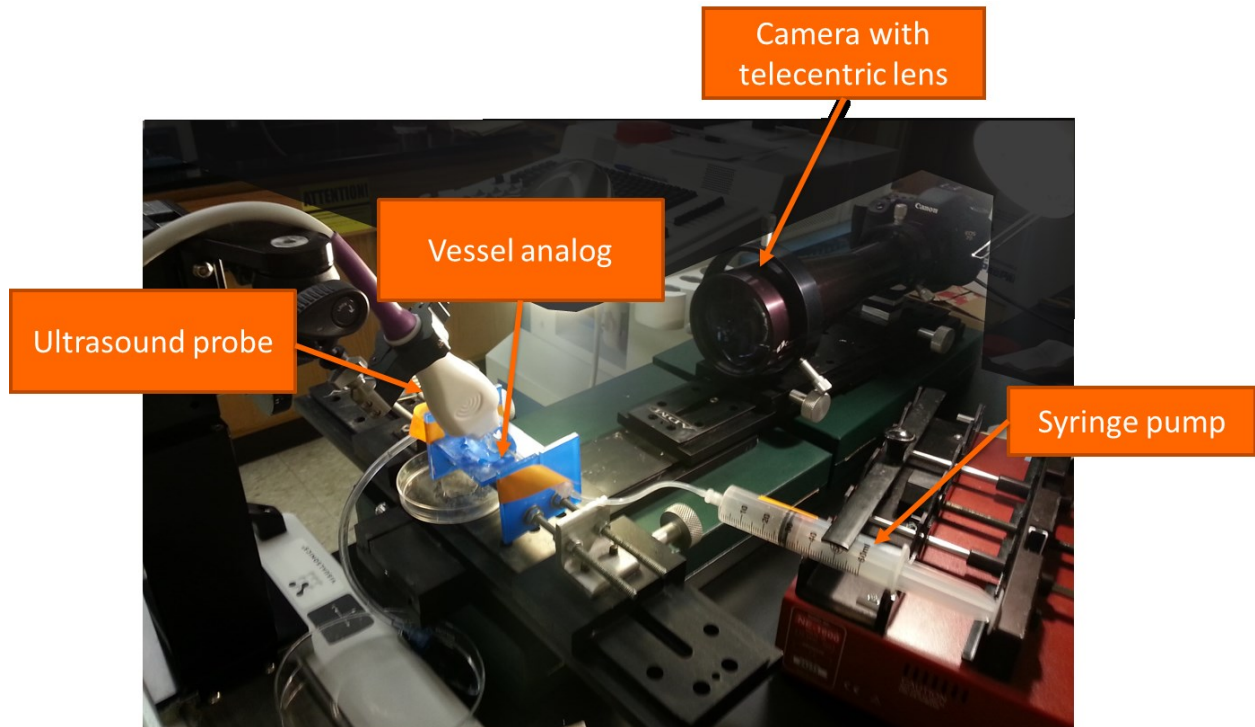


Figure 3-2: Ultrasound validation experimental setup. A telecentric lens attached to a high speed video camera was used to make diameter measurements on a murine blood vessel-sized tube *in vitro*. Simultaneously, strains were measured using the proposed ultrasound measurement system. The resulting circumferential strains were compared between the two measurement methods.

The 60 mL syringe was then connected to a syringe pump and controlled via a computer running pump system software (New Era pump systems, Farmingdale, NY). Cyclic strains were applied to the tubing wall at flow rates of 6, 8, 10, 12, 14 and 16 mL/min for periods of 1, 1.5, 2, 2.5 and 3 seconds. While running each protocol, both ultrasound and video data were simultaneously recorded as described below.

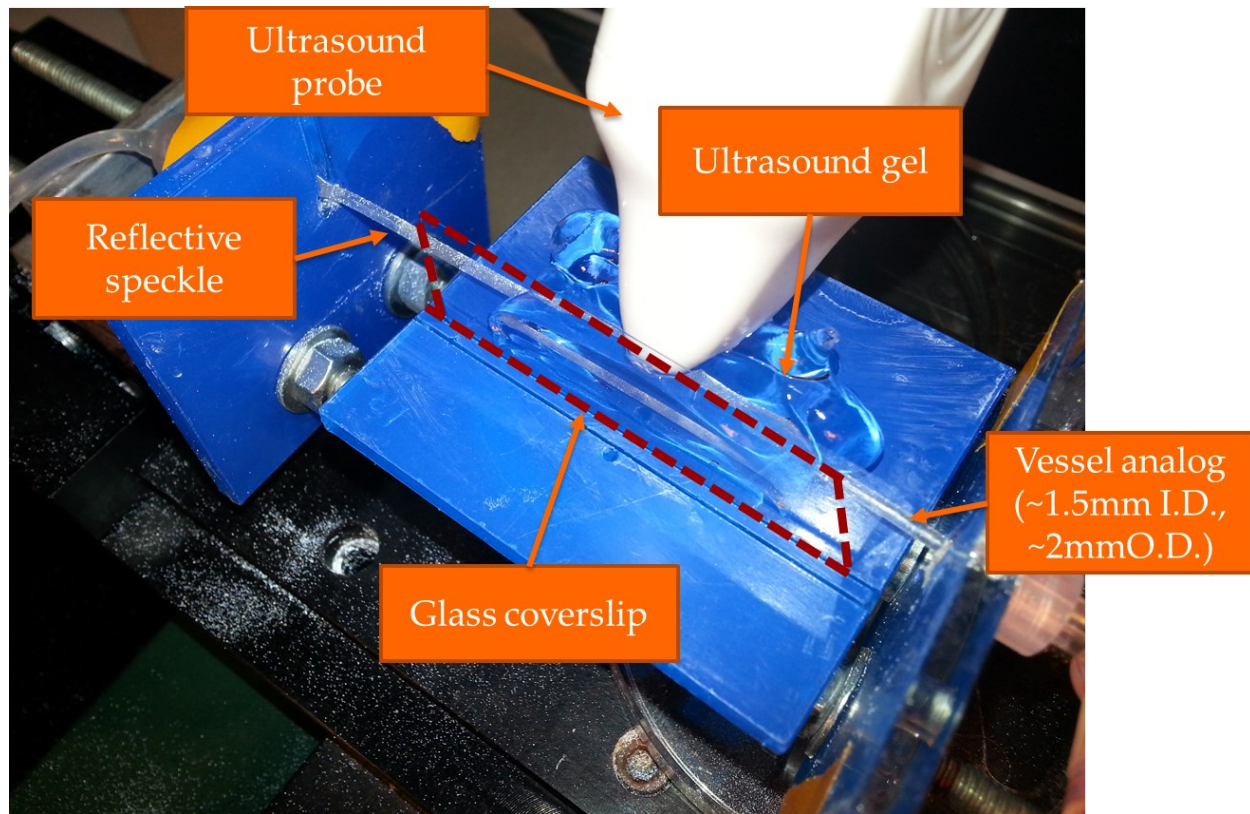


Figure 3-3: Close-up of ultrasound validation tubing setup. A large glass coverslip is used to create an optically flat surface behind which resides the ultrasound gel. This allows for clear, undistorted imaging of the tubing wall which has been pre-speckled to create a large light intensity distribution.

3.2.3 Ultrasound data acquisition and analysis

A 700 MHz ultrasound probe (MS700) and FUJIFILM Visualsonics Vevo2100 ultrasound system were used to record luminal wall strains within the tube. The ultrasound transducer was placed in the ultrasound gel and the tube lumen was visualized and brought into focus. Several consecutive cycles were recorded at a frame rate of 300 Hz. Cyclic mechanical strains as measured at the lumen of the vessel using Green's definition were calculated and reported. Given that strains measured via ultrasound are 1 dimensional only, the stretch ratio was computed and green's strain was calculated via equation (3-A). Cumulative Green's strains were computed for each cycle and averaged for at least 5 cycles in each dataset

$$E = \frac{1}{2}(\lambda^2 - 1) \quad (3-A)$$

3.2.4 Video data acquisition and analysis

A digital camera (EOS 7D, Canon USA, Melville, NY) was attached to the telecentric lens and the tubing was brought into focus. Videos were recorded at maximum resolution and 30 frames per second simultaneously with the ultrasound system. High Density Mapping, a speckle tracking program previously developed in our lab along with custom MatLab programs was used to calculate strains on the outside of the vessel using Green's definition.^{78, 181} Briefly, HDM uses a phase correlation algorithm in 2 dimensions to efficiently determine displacements of regions of an image. As seen in Figure 3-4, small 16 by 16 pixel size sub-regions are compared between two sequential images and combined via phase correlation in the Fourier domain. After subsequent application of an inverse Fourier transform, it is possible to determine the pixel level displacement of the region. Using the sub-pixel algorithm first described by Foroosh *et al.*¹⁸⁵, it is then possible to determine the displacement of the region with an accuracy of 0.09 pixels and a precision of 0.02 pixels.¹⁸¹ This process is iterated across all sub-regions (overlapping by 8 pixels) and images in a dataset to produce displacement fields. From these displacement fields, the displacement gradient tensor is determined and cumulative green's strain is computed (Figure 3-5). For this study, only the normal plane strain in the circumferential direction is reported.

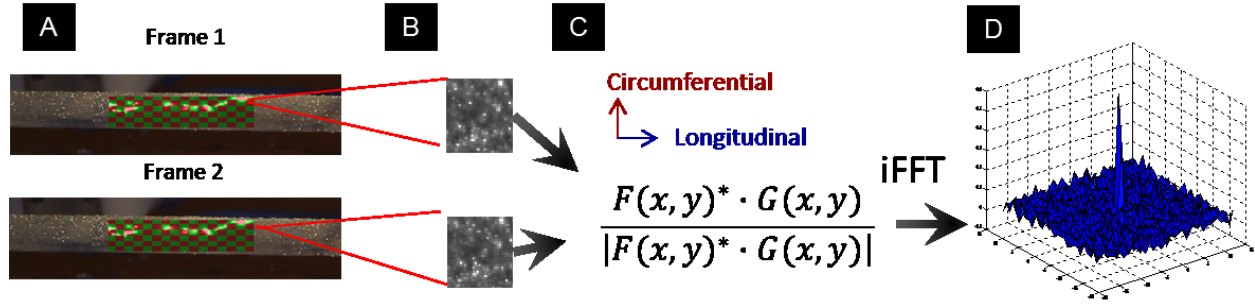


Figure 3-4: Use of High Density Mapping to determine displacement fields. A) A region of interest is defined in an image and divided into 16x16 pixel sub-regions. B) Fast Fourier transforms of corresponding sub-regions of sequential images are computed. C) Phase correlation is applied to the two images in the Fourier domain and the inverse Fourier transform of the result is taken. D) The resulting 2D plot contains a peak at the pixel level displacement of the region.

$$\begin{array}{cccc}
 \text{A} & & \text{B} & \text{C} & \text{D} \\
 U_{ij} = \begin{bmatrix} \frac{du}{dx} & \frac{du}{dy} \\ \frac{dv}{dx} & \frac{dv}{dy} \end{bmatrix} & \longrightarrow & F_{ij} = U_{ij} + \delta_{ij} & \longrightarrow & E_{ij} = \frac{1}{2} (F_{ij}^T \cdot F_{ij} - \delta_{ij}) \quad F_{1-3} = F_{1-2} * F_{2-3}
 \end{array}$$

Figure 3-5: Computation of green's strain from HDM data. A) The displacement gradient tensor U_{ij} is computed from HDM displacements. B) The deformation gradient tensor F_{ij} is computed from displacement gradients (δ_{ij} represents the Kroneker delta) C) Green's strain tensor E_{ij} is computed. D) Cumulative strains across consecutive frames can be computed by multiplying deformation gradient tensors using matrix algebra.

3.2.5 Theoretical relationships

Since commercially available tubing in the size range targeted in this study was limited, the tubing used herein had a considerably thick wall compared to its radius. For this reason, thin-walled tubing mechanical assumptions could not be used. To better understand the expected relationship between strains measured on the inside wall of the tubing (ultrasound) and strains measured on the outside (HDM), the theoretical relationship was determined mathematically.

3.2.6 Statistics

Statistical analyses were executed using Sigmaplot 11 (Systat Software, San Jose, CA). The resulting ultrasound and image strains for each pump condition were compared using a Pearson product moment correlation. Statistical differences between sonomicrometry and HDM strains were determined using a paired t-test. Statistical powers are reported for all negative statistical results.

3.3 Results

3.3.1 Comparison of sonomicrometry and optical strain measurements

Mechanical strains generated on Penrose tubing wall by a syringe pump were simultaneously recorded via a high speed video camera and sonomicrometer. Strains computed using HDM (from the high speed video) and sonomicrometer were averaged across 7 cycles. Data are presented as mean \pm std and statistical comparisons and a paired t-test yielded no significant difference between the two methods ($p=0.39$, Power: 0.05). The resultant strain values are presented in Figure 3-6.

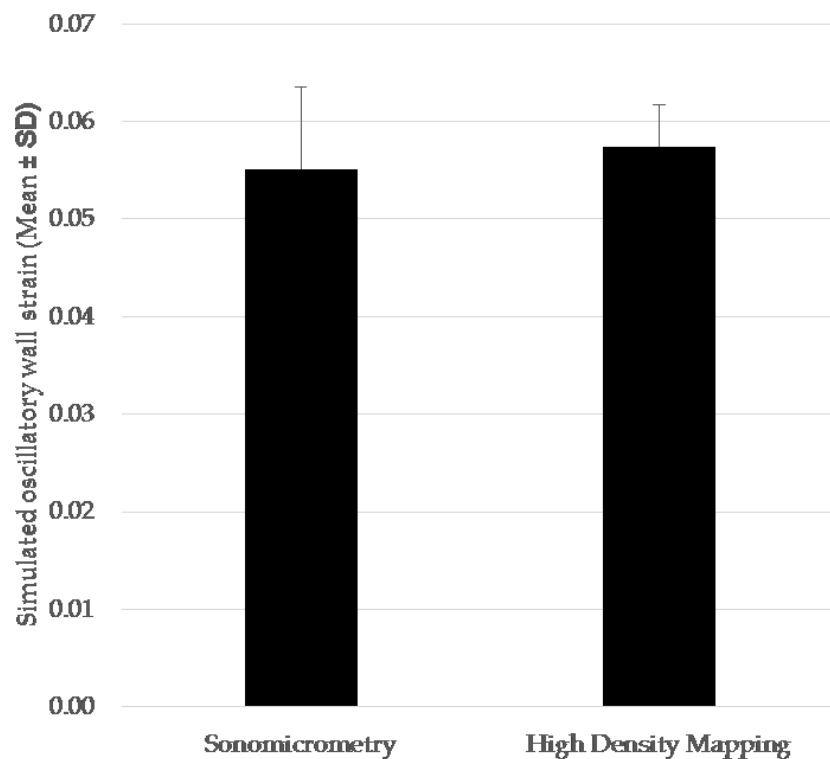


Figure 3-6: Simulated wall strains in Penrose tubing. Data show mean oscillatory wall strain as computed via sonomicrometry and high density mapping for 7 simultaneously recorded cycles. No significant difference between the two groups was seen using a paired t-test.

3.3.2 Comparison of optical and ultrasound strain measurements

Although strain measurements were recorded at 4 different flow rates for 5 different amounts of time, upon analysis, usable strain recordings were only found using HDM for the 8

combinations that produced the largest strains. Thus, data reported below is for flow rates of 10, 12, 14 and 16 mL per minutes and flow times of 2.5 and 3 seconds only. For the selected 8 combinations, clear strain curves were computed using both HDM and US. Sample regions of interest and curves for each method in Figure 3-7: Sample regions of interest and strain curves. Peak strains for corresponding recordings from both HDM and ultrasound were averaged across at least 5 cycles and plotted with ultrasound strain on the x-axis and HDM strain on the y-axis (Figure 3-8).

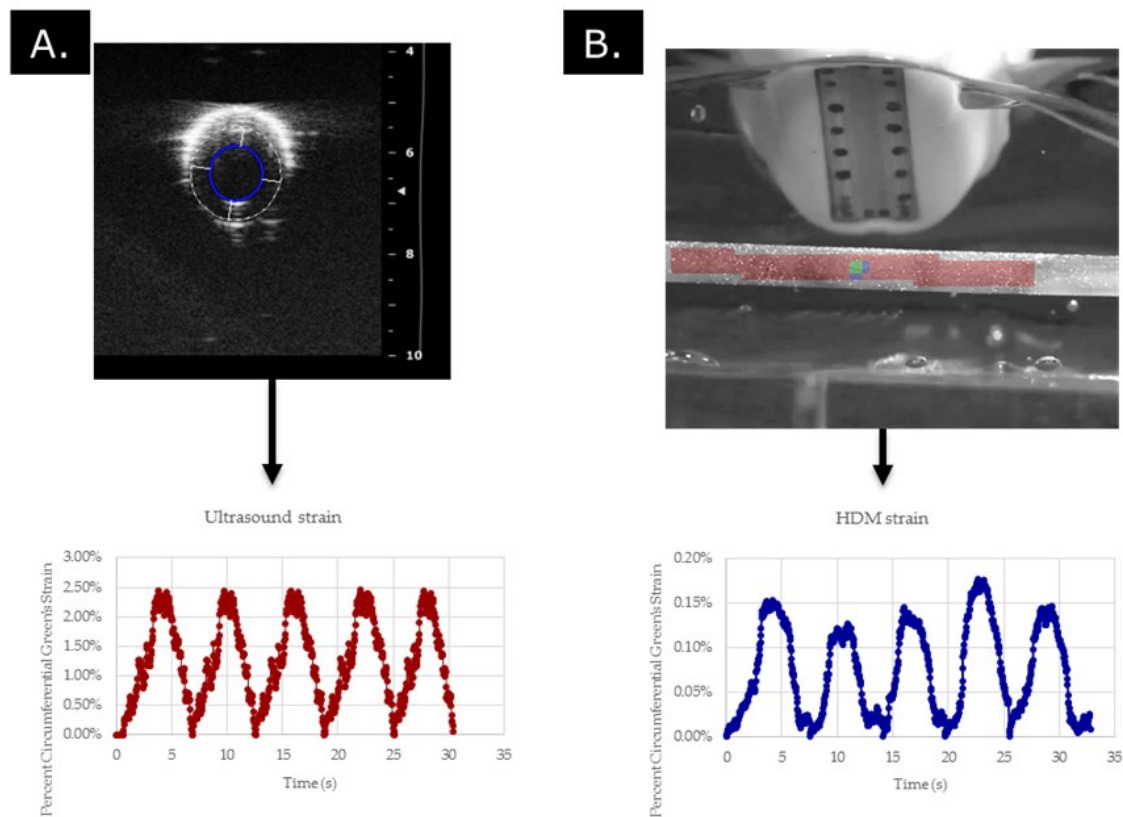


Figure 3-7: Sample regions of interest and strain curves. A) Ultrasound region of interest showing tubing lumen with selected ultrasound tracing and resulting strain curve. B) HDM images with region of interest (red) sub-image size (green square) and sub-image shift (blue square).

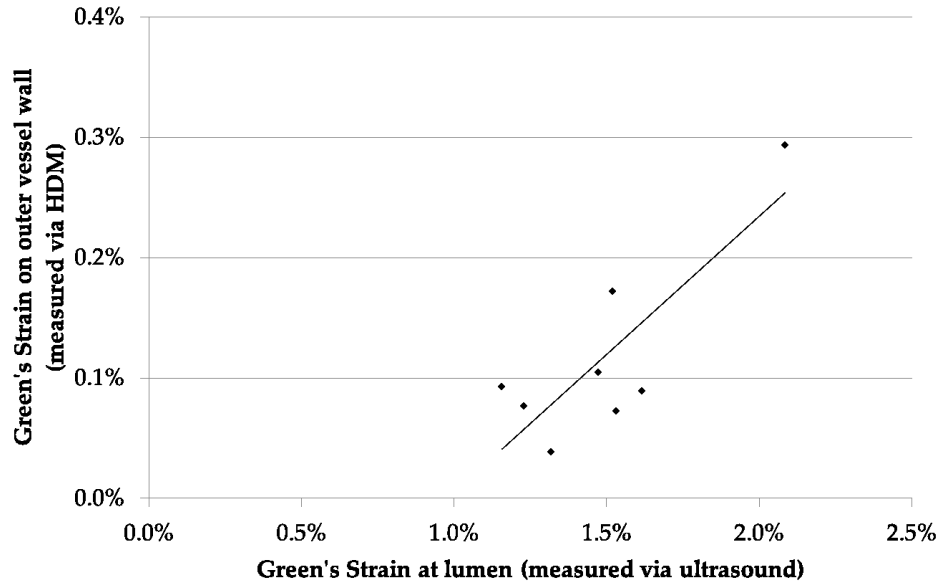


Figure 3-8: Comparison of wall strains recorded with ultrasound and HDM. Note that strains measured with ultrasound were measured at the tubing lumen while strains measured with HDM were measured on the outer wall. Line indicates the linear regression of the data.

As seen in Figure 3-8, strains measured via HDM were significantly lower than those measured with ultrasound. Despite this difference, comparison of the data from the two methods yielded a Pearson's product moment correlation coefficient of 0.83. The indicated linear regression of the data resulted in a slope of 0.23 with the linear fit equation (3-B):

$$E_{\text{HDM}} = 0.23E_{\text{US}} - 0.002 \quad (3-B)$$

3.3.3 Theoretical relationships between lumen and outside strains

The tubing used in this study has a thickness that is almost 25% of its inner radius. As a result, it must be considered a thick-walled pressure vessel and its change in thickness cannot be ignored. Since pressures were not measured in this study, the most relevant relationship to our study is the relation of strain at the outer wall (experimentally measured using HDM) to luminal strain (experimentally measured by ultrasound). Since Green's strain was implemented

for all calculations, Equation (3-A), was used to calculate strain from stretch ratios with E representing Green's strain and λ representing the stretch ratio.

To determine the relationships between Green's strain for the inner and outer walls, the wall cross-sectional area (and therefore volume) were assumed to be constant. This assumption yielded the relationship in Equation (3-C) where r_o and r_i respectively are the outer and inner radius before stretching and R_o and R_i are the outer and inner radii after distension:

$$r_o^2 - r_i^2 = R_o^2 - R_i^2 \quad (3-C)$$

Given that the stretch ratio (λ) is the ratio of the radius after distension to the radius before distension, the following relation between inner and outer strains can be determined. A complete derivation of Equation (3-D) is described in Appendix C:

$$E_o = E_i \cdot \frac{r_i^2}{r_o^2} \quad (3-D)$$

Using this ratio, a theoretical strain relationship curve can be determined and compared to the actual data. This curve is shown in Figure 3-9 alongside the experimental data. The resultant theoretical relationship indicated that the strain measured via HDM is theoretically expected to be 0.57 times the strain measured with ultrasound.

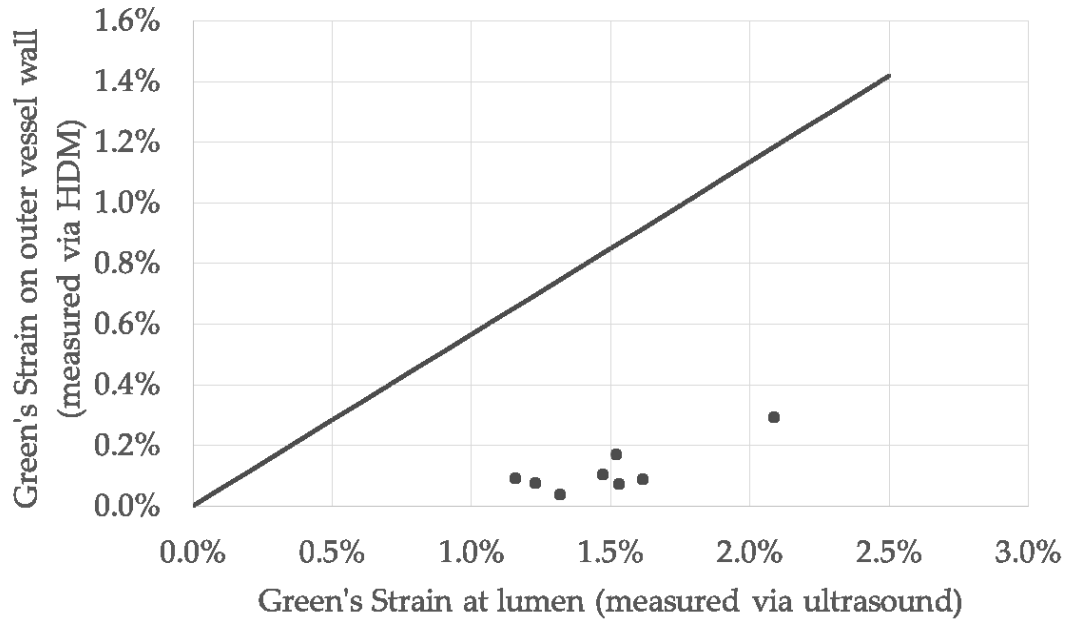


Figure 3-9: Theoretical relationship between lumen and outside strains for silicon tubing. Data points show strain as measured experimental while the line shows the theoretical relationship.

3.4 Discussion

In this chapter, we aimed to validate our ultrasonography-based approach to measuring small diameter vascular strains against another method of measuring strains. In order to accomplish this objective, a simple *in vitro* ultrasound phantom of a blood vessel was constructed and placed in a system designed specifically to allow for simultaneous comparison of strains measured with two different methods. Due to our expertise and publication history in the field of optics-based strain measurements,^{37, 181, 183} we chose to use our high density mapping software to measure regional displacements on the outside of the tubing wall. To enhance this approach, telecentric optics were employed to minimize perspective distortion.

To demonstrate the capabilities of our HDM-based strain measurement approach, HDM strains were directly compared to those measured via sonomicrometry, a method often used as the gold standard for displacement measurements.^{184, 186} Using ¼ inch diameter Penrose tubing, we demonstrated that no difference in oscillatory wall strain values was determined between

sonomicrometry and HDM. Due to the large size (2mm diameter) of available sonomicrometry crystals, we were unable to use sonomicrometry in a direct comparison with our ultrasound-based strain measurement approach. We therefore directly compared HDM with ultrasonography.

The tubing strains that could be produced by our system were primarily limited by the amount of force that could be generated by our syringe pump and the high stiffness of small diameter tubing that was commercially available at the time of this study. As a result of these system limitations, the mechanical strains experimentally measured with both HDM and ultrasound in this chapter were extremely low ($< 2.5\%$) and therefore much smaller than those expected *in vivo*, where reported values are 20-25%.³⁵ Despite these limitations, the results presented in Figure 3-8 demonstrate a clear positive correlation between the data measured using the two methods with a Pearson's correlation coefficient of 0.83. Although the data do correlate, the relationship observed was definitely not 1:1; with strains measured by HDM considerably less than those measured by ultrasound. In order to better understand the relationship we should expect between these two measurements, the theoretical relationship was determined by assuming constant tubing volume. By deriving and applying Equation (3-D), we demonstrated that the theoretical strains measured via HDM at the tubing wall are expected to be smaller than those measured by ultrasound. This theoretical finding supports the experimental findings found in this chapter.

The second factor we suspect may have affected our measurements in this chapter is the lower limit of the spatial resolutions of both the ultrasound and optics based measurement systems. Since the methods used by the ultrasound system to measure displacements are

proprietary, it is not possible for us to determine the spatial resolution of the system. Using an image of a scale with known length, the imaged pixel size for the HDM measurements reported in this chapter is $28.6\text{ }\mu\text{m}$. The region of interest that was used for HDM analysis was 64 pixels ($1830\text{ }\mu\text{m}$) tall. Given that the reported theoretical displacement accuracy of HDM is 0.09 pixels¹⁸¹ ($2.57\text{ }\mu\text{m}$ in this study), the smallest strain that can be accurately determined in this study is 0.14%. This strain level was calculated by dividing the smallest pixel displacement that can be measured by the 64 pixel region height. Since the strains measured via HDM in this chapter are very close to or below this value, the reported HDM measurements are likely not very accurate due to the system's resolution limits. To overcome these limitations, other methods of measuring strain should be used in the future to validate our ultrasound-based measurement approach. One method that has been used increasingly in medical imaging recently is optical coherence tomography (OCT).^{187, 188} OCT uses the same principles as ultrasound imaging, but uses the optical reflective properties of tissues rather than the sonic impedance to determine represent the tissue. Given that the wavelength of light waves are significantly smaller than that of high frequency sound waves, the resolution of OCT can be as high as $1\text{ }\mu\text{m}$ and some systems have reported temporal resolutions greater than 1 kHz.¹⁸⁹ Future studies should utilize a higher resolution state-of-the-art, such as OCT, to more accurately validate ultrasound-based strains.

Despite the limitations in the system used herein, the strains measured between the two methods correlate well and are on the same order of magnitude as the theoretical values. An improved testing system with the capability to produce larger tubing strains would likely yield an even better correlation between the two methods. Given that strain measurements made

using ultrasound used in the remainder of this dissertation will not be compared between measurement methods, the limited correlation demonstrated in this chapter shows that our ultrasound-based approach can provide usable measurements even when near its resolution limits. In the next chapter of this dissertation, we will apply our ultrasound system to *in vivo* measurement of arterial strains.

4 Objective 1B: *In vivo* testing of ultrasound vascular strain methodology

The introduction (starting with section 4.1.1), methods, results and discussion presented in this objective are published in the Journal of Vascular Surgery. These sections are reprinted from: The Journal of Vascular Surgery, 56(2), John T Favreau, Binh T Nguyen, Ian Gao, Peng Yu, Jacob Schneiderman, Glenn R. Gaudette, C. Keith Ozaki, “Murine ultrasound imaging for circumferential strain analyses in the angiotensin II abdominal aortic aneurysm model”, p. 462-469, Copyright 2012, with permission from Elsevier (Appendix A).

4.1 Introduction

In Objective 1A (Chapter 3) of this dissertation, we aimed to demonstrate that ultrasound strain measurements can be used to measure strain, as validated with optical measurement techniques, in a small analog of a blood vessel. For Objective 1B, we aimed to test this system on a live, *in vivo* model of vascular disease. For this study, we chose to analyze strains in a murine model of abdominal aortic aneurysm (AAA). The mouse model was chosen primarily because it is extensively used in the study of the mammalian vasculature and the diseases that affect it.

4.1.1 Aortic aneurysms

Despite knowledge insights over the last decades, the molecular mechanisms of aortic aneurysmal disease remain obscure. Beyond some known clinical risk factors, biomechanical forces contribute to abdominal aortic aneurysm (AAA) development, progression, and rupture.¹⁹⁰⁻¹⁹² The composition and mechanical properties of AAAs are different from those of normal aortas,¹⁹³ with AAAs being stiffer and less distensible than non-aneurysmal aortas.

4.1.2 Murine models of aortic aneurysms

Murine models have emerged as a tool to enhance understanding of aneurysms,^{169, 170} though biomechanical studies have been limited in these models. One of the most commonly employed models involves subcutaneous delivery of angiotensin II (Ang II) into apolipoprotein

E-deficient (apoE^{-/-}) mice via an implanted osmotic pump.^{169, 194-197} Despite widespread clinical value, the use of longitudinal imaging in these aneurysm models remains scarce and under-utilized because the small size of the animals make the quantification and characterization of AAA progression difficult and time-consuming. Current methods for measuring aneurysm biomechanics and progression are simplistic in that they assess only the gross appearance of the aorta,¹⁹⁸ the maximum diameter of the aorta in situ,¹⁹⁹ or the luminal diameter *ex vivo*.²⁰⁰ To date, a few *in vivo* imaging studies have been done on small animal AAA models, but they also only measured aortic diameters.^{38, 201-203} Recently, high-frequency ultrasound imaging systems (e.g. Visualsonics Vevo 2100, Visualsonics, Toronto, ON, Canada) have been developed to noninvasively micro-image mice *in vivo*, and such approaches can reliably detect and measure the luminal diameter of AAA in apoE^{-/-} mice infused with Ang II.^{38, 39} At the same time, speckle-tracking technology in ultrasound imaging has emerged as a quantitative, objective technique to accurately evaluate myocardial function and dynamics. Speckle tracking functions by tracing the displacement of speckles during the cardiac cycle to measure strain and strain rate,⁴⁰⁻⁴³ and it has been used in the assessment of mouse models of cardiac dysfunction.¹⁷³

4.2 Materials and methods

4.2.1 Mouse model

Male apoE deficient mice (B6.129P2-Apoetm1Unc/J) were purchased from the Jackson Laboratory (Bar Harbor, ME), maintained on a 12-hour light-dark cycle, and received water and assigned chow *ad libitum*. All animal experiments were performed according to protocols approved by the Institutional Animal Care and Use Committee and complied with the Guide for the Care and Use of Laboratory Animals (National Institutes of Health Publication No. 85-23, Revised 1996).

At 16 weeks of age, osmotic mini-pumps (Alzet Scientific Products, Model 1002, Cupertino, CA) loaded with Ang II (500-1,000 ng/min/kg) were sterilely implanted in the dorsal subcutaneous tissues under 1-2% isoflurane inhalant anesthesia with oxygen at 1 L/min, and wounds closed with absorbable sutures.

4.2.2 Dietary perturbations

All animals received a 10 kcal% fat standard chow diet after weaning (D12450B; Research Diets Inc., New Brunswick, NJ). The normal chow group was maintained on this diet throughout the course of the experiment. To study the effect of diet induced obesity on aortic wall elasticity, animals designated as high fat were pre-fed with a 60 kcal% fat western diet (D12492; Research Diets Inc.) 6 weeks prior to Ang II infusion and maintained on this diet during the study. Table 4-A summarizes the experimental groups and the specific diets over time.

Table 4-A: Experimental groups for Objective 1A

Diet	Age at Implant	Ultrasound acquisition
Normal Chow (10 kcal% fat)	16 Weeks	Preop, Day 3 (n=8) Preop, Day 14, Day 28 (n=10)
High Fat (60 kcal% fat)	16 Weeks	Preop, Day 3 (n=6) Preop, Day 14, Day 28 (n=10)

4.2.3 Study design

High resolution ultrasonography was performed using a Vevo 2100 Imaging System with MS700 (30-70 MHz) and MS550D (22-55 MHz) linear array transducers (Visualsonics). For short term study groups, data was collected before implantation (pre-op) and at day 3 after

implantation, while for long term groups, data was collected preoperatively, at day 14, and at day 28 after implantation. Mice were anesthetized using 1-2% isoflurane inhalant anesthesia with oxygen at 1 L/min and animals were placed in supine position on a moveable, heated stage maintained at 37°C. Hair was removed from the abdomen and thorax using a depilatory cream. Warmed ultrasound transmission gel was applied to the ventral surface of the animal and the probe was positioned on a fixed stand perpendicular to the stage. After adequate visualization of the aortic segments of interest, one hundred frame (at 240-270 frames per second) B-mode cine image sequences were then recorded over an average of 2-3 cardiac cycles. Since aortic pathologies associated with Ang II infusion frequently occur at defined locations along the aorta (arch and suprarenal > infra-renal and thoracic), six different anatomic segments were chosen to allow for comparisons of mechanical strains at these locations (Figure 4-1).

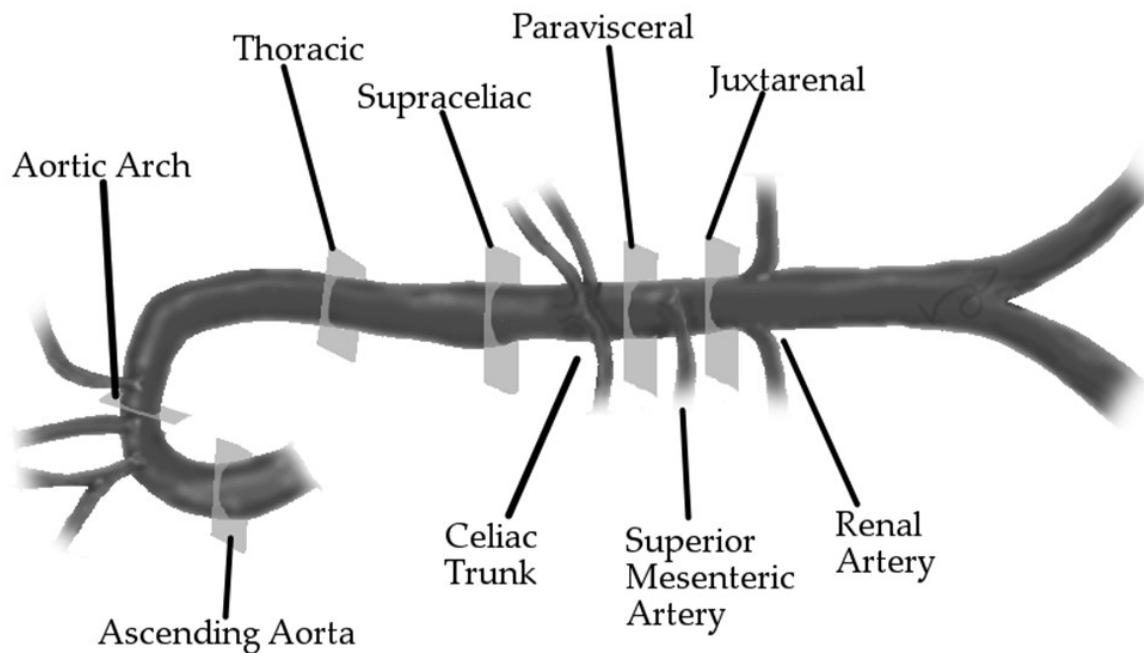


Figure 4-1: Segments of interest analyzed in the thoracic and abdominal aorta. Celiac trunk (CT), superior mesenteric artery (SMA) and renal arteries (RA). The thoracic region = cross-section 5mm proximal to the CT; the supraceliac region = cross-section 1mm proximal to the CT; the paravisceral region = cross-section between the CT and SMA; and the juxtarenal region = cross-section 1mm distal to the SMA.

Ultrasound cine loops collected during the imaging procedure were analyzed to calculate circumferential strains. Cine loops were loaded into Vevostrain 2100 Advanced Cardiac Analysis Software (Visualsonics) and analyzed using the manufacturer's cardiac speckle tracking algorithm. A closed spline of 48 points was manually drawn around the edge of the vessel cross-section in the ultrasound image. Accuracy of speckle tracking throughout the cine loop was verified visually. If tracking did not pass visual inspection, splines were redrawn until adequate tracking was achieved. The frame-to-frame displacements of each of the 48 points throughout the cine loop were the output for strain analysis. Additionally, representative frames from the ultrasound images were saved to allow determination of vessel

regions that did not have enough speckle contrast for adequate analysis (regions that correspond to renal artery branching or echogenic shadow artifacts) (Figure 4-2).

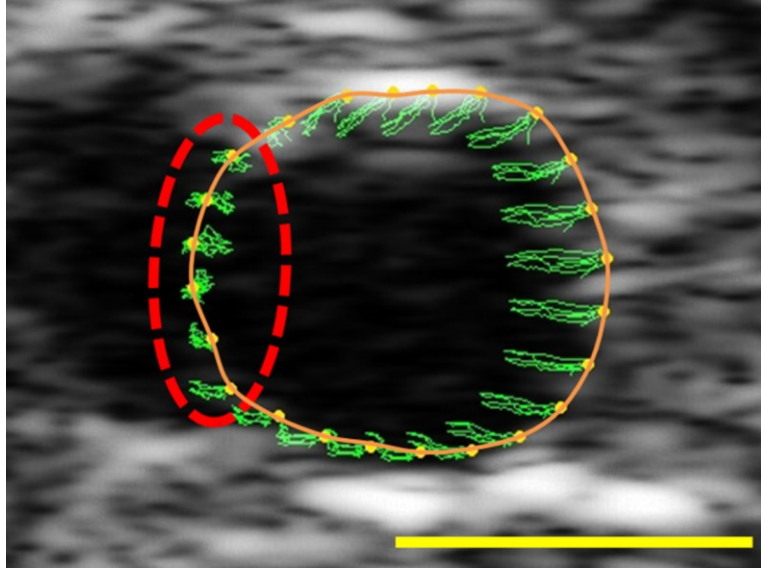


Figure 4-2: Sample ultrasound image of an aorta. Orange line indicates manually drawn spline. Green traces show the path of the tracking points (yellow) throughout several cardiac cycles. The dashed red line indicates a region that has poor contrast (likely due to a branching vessel) and therefore poor tracking. These regions were dropped from the analyses to improve accuracy. Yellow scale bar is 1-mm in length.

4.2.4 Strain calculation

Displacements from the Vevostain software were then downloaded into a custom MatLab (Mathworks, Natick, MA) program and analyzed to determine circumferential strain from displacements. Strains were determined at each of the 48 points around the vessel.

Circumferential strains were calculated using the definition of the Cauchy strain tensor for cylindrical coordinates Equation (4-A).⁷⁵

$$\varepsilon_{\theta\theta} = \frac{1}{r} \left(\frac{\partial u_{\theta}}{\partial \theta} \right) + u_r \quad (4-A)$$

Radii were measured by determining the distance from each point to the centroid of the points around the vessel. It was assumed that the local radius around each measured point was constant at any particular time point. The strains at each point around the vessel were averaged

to give a mean incremental strain from frame to frame. The analysis points were then compared with images from the ultrasound machine. Regions that appeared dark and which had no speckle contrast were then manually dropped from the analysis. An example of these regions is shown with a dashed red line in Figure 4-2. After excluding such un-interpretable regions, average strain curves were plotted, and peaks and troughs were located and manually verified using a custom MatLab program. The maximum circumferential strain value was calculated as the average difference between consecutive peaks to troughs throughout each cine loop. Resulting means were then averaged in each experimental group at each aortic location and reported as mean \pm SEM. In addition to calculating strains, vessel cross-sectional areas were determined from scaled ultrasound images. These areas were then used to determine if vessel diameters changed throughout the study.

4.2.5 Statistics

Statistical analyses were executed using Sigmaplot 11 (Systat Software, San Jose, CA). Comparisons between two groups were completed using an unpaired two-tailed Student's t-test. Comparisons between 3 or more experimental groups and between time points were made using one-way ANOVA with Tukey post-hoc analyses. All data is reported as mean \pm SEM.

4.3 Results

4.3.1 Effects of diet on aortic strain

The normal chow and high fat mice gained weight as expected based on vendor supplied data (Jackson Laboratory, Bar Harbor, ME). To confirm the ability to measure strain in the mouse aorta, pre-op baseline data for mice in the four study groups were analyzed. Data from all normal chow diet mice with all high fat diet mice were compared first (Figure 4-3). The results demonstrate a consistency of measurements in the same aortic location with animals

consuming the same diet. Additionally, our strain values were similar (maximum strains ~19-20%) to those reported by Goergen *et al.* using MRI imaging.³⁵ It also shows no statistically significant differences between normal chow and high fat diet mice at each segment along the aorta preoperatively. However, differences in mechanical strain along the aorta in the normal chow and high fat groups were noted. The major trend seen here is that in both the normal chow and high fat groups, the ascending aorta shows statistically significant higher strain values than the other anatomical locations ($P < .05$). Additionally, the lowest strain values were observed in the arch segment ($P < .05$).

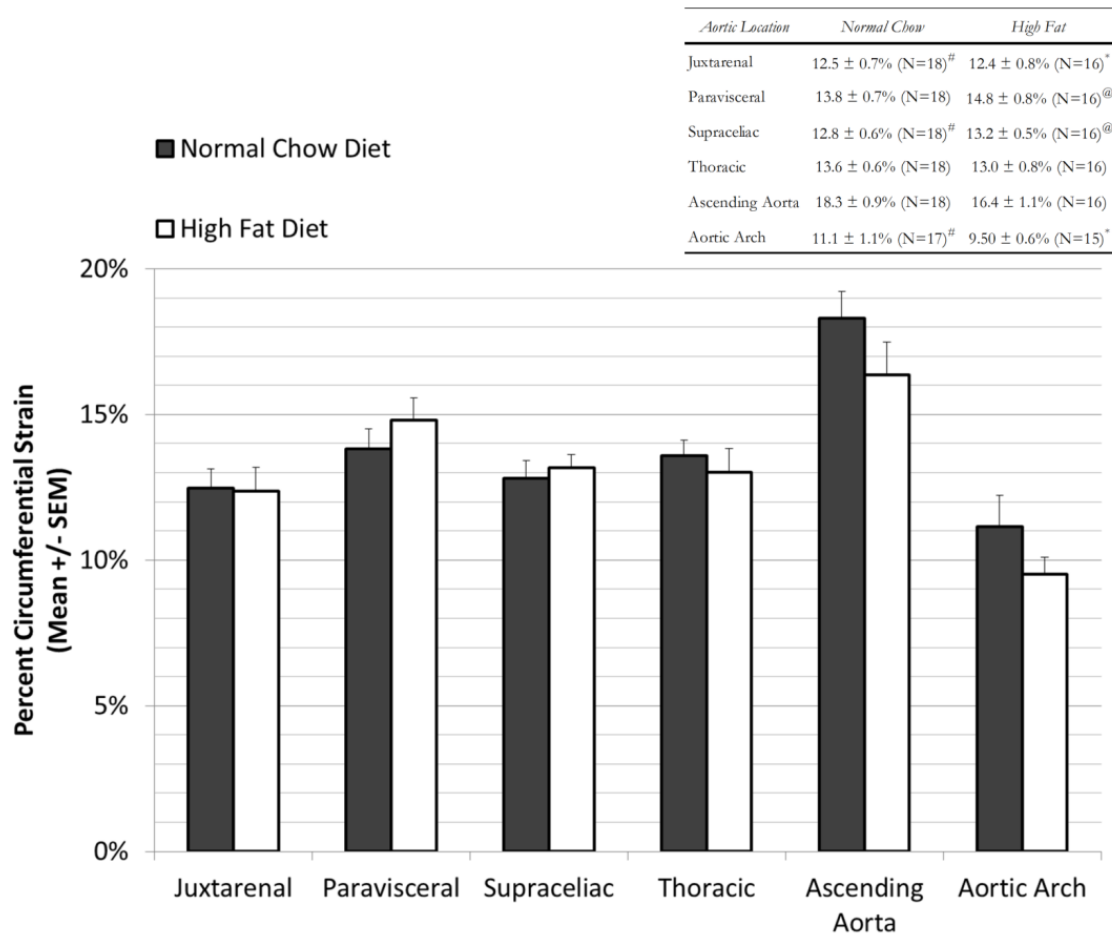


Figure 4-3: Comparison of baseline preoperative strain magnitudes. Comparisons are made across 6 aortic locations between normal chow and high fat diet mice. Statistical statements are noted in the inset table. No statistically significant differences were found between mice of different diets in any aortic location, though differentials were noted among segments as depicted. All statistical statements indicate that $P < .05$; all groups contain 15 or more animals. *Indicates statistical difference from high-fat ascending aorta; #indicates statistical difference from normal chow ascending aorta; and @indicates statistical difference from high-fat aortic arch.

4.3.2 Short term impact of Angiotensin-II treatment on mechanical strain

Using the short-term arm of the study, the acute effects of the Ang II treatment

(1000ng/kg/min) on mechanical strain in normal chow and high fat mice (Figure 4-4, A) were isolated. There is a consistent trend toward decreased strains in all aortic locations after just 3 days of Ang II treatment in the normal chow group. Reductions in the supraceliac, thoracic, and ascending aortic locations were statistically significant ($P < .05$). None of these animals showed changes in aortic diameter at day 3 post-Ang II infusion.

Similar results were found in the short-term study for the mice fed on a high fat diet (Figure 4-4, B). In this group, there was a similar trend toward decreased strain at the day 3 time point, with statistically significant decreases occurring in the supraceliac segment. Unlike the normal chow group, however, two animals in this group formed aortic aneurysms (at least 1.5 times greater diameter than initial measurement; paravisceral and supraceliac regions) by day 3 post-op, while one animal died of aortic arch rupture prior to day 3.

4.3.3 Long term effects of angiotensin II treatment on mechanical strain

Long-term changes in strain were analyzed for both the normal chow and high fat groups receiving Ang II (500ng/kg/min). In both groups there was a progressive trend towards decreased mechanical strains from pre-op to day 14 to 28 strains (Figure 4-4, C and D). The largest reduction of strain was observed in the para-visceral, and the supra-celiac segments in high fat diet mice (Figure 4-4, D). The majority of these reductions in strain corresponded directly with aneurysm formation. It should be noted that both the normal chow and high fat groups contained animals with and without aneurysm development by day 28.

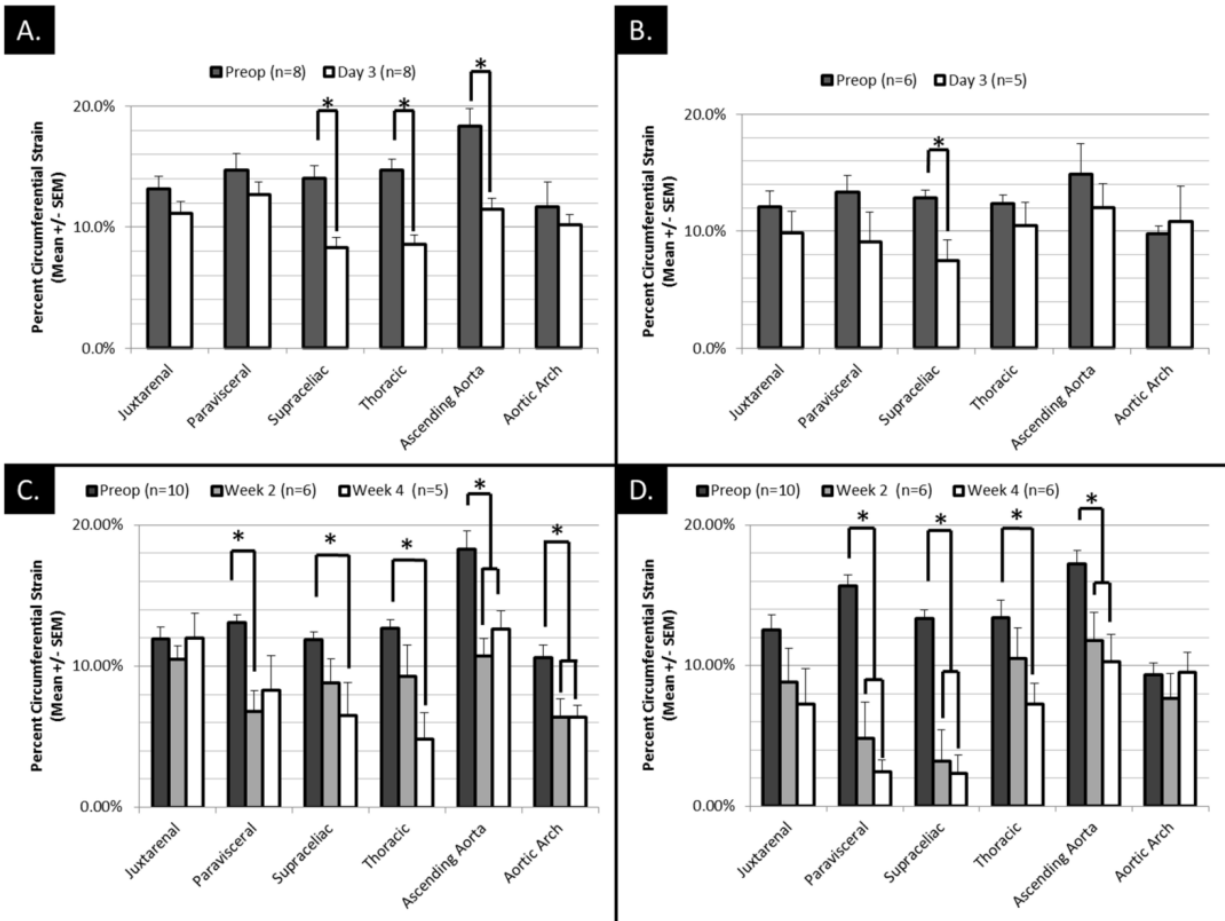


Figure 4-4: Short and long term effects of Ang II on normal and high fat animals. (A) Short-term effects of Ang II treatment on animals fed on normal chow diets. (B) Short-term effects of Ang II treatment on animals consuming only high fat diets since week 10 of age. (C) Long-term effects of Ang II treatment on normal chow animals. (D) Long-term effects of Ang II on high fat animals. * Indicates $P < .05$.

4.3.4 Relative effects of different factors on mechanical strain

The design of this study enabled the isolation of the effects of Ang II treatment from those of aneurysm formation. The percent change in strain from pre-op strain due to Ang II treatment alone, aneurysm formation at day 14, and aneurysm formation at day 28 for normal chow and high fat animals was determined (Figure 4-5). These data suggest that both the Ang II treatment and the actual formation of aneurysm play a role in reducing strain in the aorta. The results in Figure 4-5 also suggest that aneurysmal degeneration and physical remodeling of the wall may play a large role in decreasing circumferential strains. Mural thrombus was a

common finding in the Ang II mice. The thrombus likely contributed to the overall decrease in strain of the aneurismal aortic wall. However, the current study does not have enough power to tease out the component contributions of mural thrombus vs other factors on the decreased strain found in aneurismal segments.

Overall in this study, there were clear differences in aneurysm formation between the normal chow and high fat diet groups. At day 3 in the short term arm of our study, 0% (n=8) of normal chow animals had formed aneurysms. High fat animals at day 3, however, demonstrated an aneurysm formation rate of 50% (n=6). One of these high fat animals died of aortic arch aneurysm and rupture prior to day 3. In the long term arm, similar rates of aneurysm formation between normal chow and high fat animals was observed. At week 4 there was an aneurysm rate of 70% (including animals which died of aneurysmal arch rupture by week 4). In contrast an aneurysm formation rate of 88% was seen in high fat animals. We were not, however, able to distinguish a difference in pre-Ang II strain measurements in animals that subsequently develop aneurysms vs no aneurysms (no predictive capability).

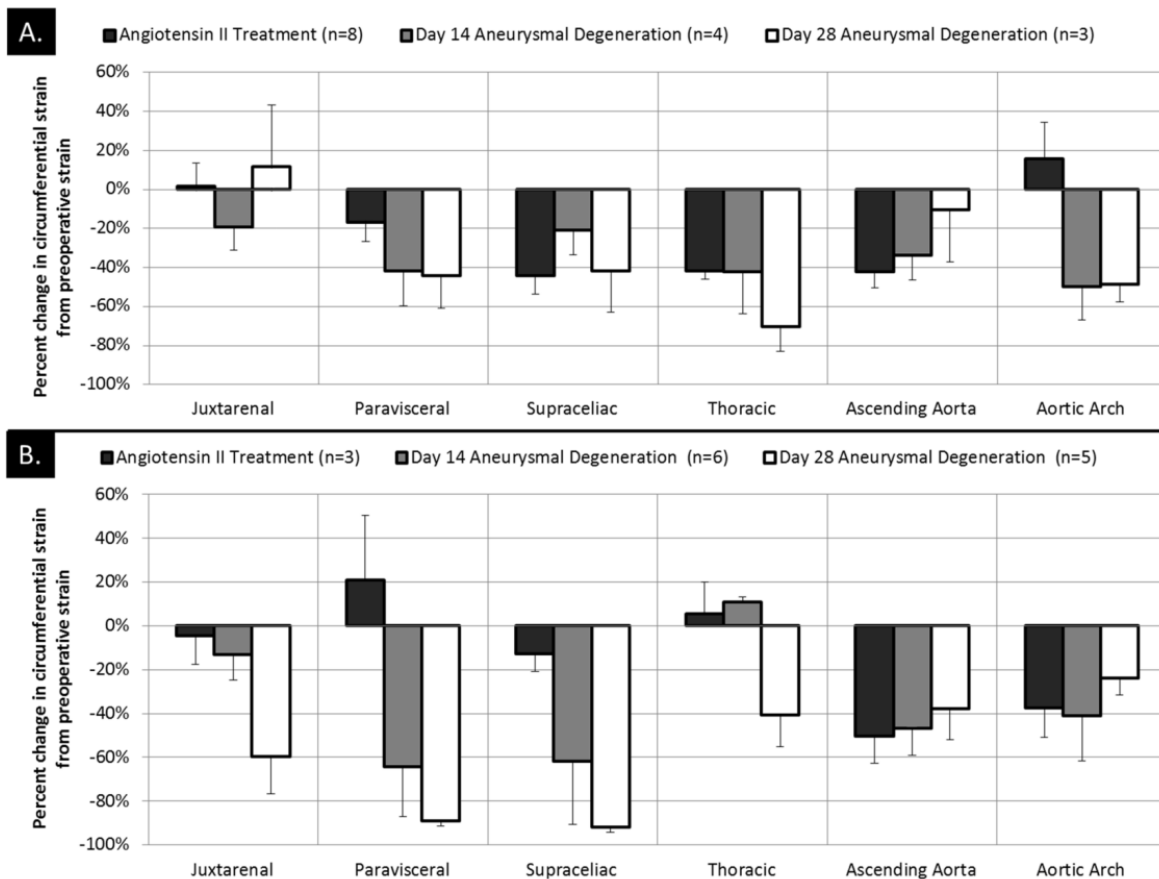


Figure 4-5: Effects of Ang II and aneurysmal degeneration on aortic wall strain. Data are reported as percent change in strain from pre-operative strain. The Ang II group contains only animals that did not have aneurysms at Day 3 from the early study. Day 14 and Day 28 aneurysmal degeneration groups only contain data from animals that had aneurysmal expansion (increase in size of 150% or more) detected via ultrasound scans. Data for normal chow and high fat groups are shown in (A) and (B), respectively.

4.4 Discussion

AAAs lead to over 15,000 deaths per year in the United States alone, and some even estimate the annual death rate from AAA to be as high as 30,000. Most are asymptomatic until catastrophic rupture, and ruptured AAAs continue to have high morbidity and mortality.²⁰⁴ Hence, there is an undeniable need to fully understand the pathophysiology of AAAs and to improve patient selection for expansion and rupture prediction and prevention.

The exact pathogenesis of AAA is complex and still unknown, but clinical risk factors are known which include smoking, male gender, age, family history, previous vascular disease,

hypertension, and hypercholesterolemia.¹⁷⁰ Biologically aortic wall inflammation and oxidative stress appear to hold a role in AAA formation.²⁰⁵ The immune system is also believed to be mechanistically involved in the development of AAAs, along with a reduction in the density of smooth muscle cells, elastin and collagen fibers, which are degraded by proteolytic enzymes (mostly matrix metalloproteinases).²⁰⁶ The aortic wall structurally depends on elastin and collagen, but in aneurysm disease medial elastin degradation (elastolysis) occurs, causing dilatation of the aorta.¹⁷⁰

Biomechanical forces stand as a pivotal factor in AAA development and rupture.^{190-192, 207} Peak AAA wall stress may be superior to maximum diameter in differentiating rupture risk.^{190, 192} Additionally, due to unevenly distributed wall stresses, overall AAA wall stress does not directly depend on maximum diameter.²⁰⁸

Ultrasound serves as a useful tool not only clinically for infrarenal aortic aneurysm surveillance, but also experimentally for quantification of aortic morphology and biomechanics. Contemporary high-frequency ultrasound represents a significant improvement over prior techniques in evaluating the aorta in murine AAA models. The approach is relatively non-invasive imaging, can be performed longitudinally, allows for examination of aneurysm prone/protected regions, and in combination with analytical approaches such as speckle tracking for strain analyses it provides more information than previous murine AAA imaging studies that only measured maximum aortic diameter. The primary downside is the expense of the device and technical expertise needed to acquire image data, though it has been shown that high-frequency ultrasound can be performed with relatively small intra-individual and inter-individual variance.³⁸ Other groups have used *in vivo* pulse wave velocity in non-aneurysm

studies to show that apoE^{-/-} mice infused with Ang II have significantly increased vessel stiffness compared with controls after 30 days.²⁰⁹ However, this report did not provide localized stiffness data. Other related imaging modalities are in development for *in vivo* murine studies—for example quantification of murine aortic cyclic strain and motion using 3D MR angiography in relation to its implications for AAA growth.³⁵

In the current experiment high frequency ultrasound was used to assess aortic wall strain in apoE^{-/-} mice at selected time points during Ang II-induced aortic aneurysm development. Wall strain correlated with the pathological events that occurred in different segments of the aorta. Baseline wall strain was measured in selected segments along the aorta, revealing a rather high strain in the ascending aorta, while the aortic arch manifested the lowest basic strain. As Ang II was given to our mice, the ascending segment did not manifest aneurysmal dilatation. However, as expected, the arch responded dramatically by developing aneurysms, some of which ruptured within the very early stage (3 days). Cao *et al.* described the phenomenon of early development of aneurysm with subsequent rupture, ranging at 25% of all mice.¹⁹⁶ In their series, 44% presented with arch aneurysms. The prevalence of early development of aortic aneurysm correlates with age. Also, it is assumed to represent a genetic predilection of some of the apoE^{-/-} mice, presenting with aortic arch structural aberration, which yields a stiffer vessel wall. The later phase of Ang II infusion (as assessed on days 14 through 28) was characterized by a significant reduction of wall strain in the supra-renal segment, namely the para-visceral, and supra-celiac regions. It is not surprising, therefore, that those segments are most affected by aneurysm formation in this model. Notably, the aneurysmal dilatation by itself leads to an increased vessel diameter, which further decreases

wall strain locally. The data collected via longitudinal non-invasive assessments emphasize the significance of anatomical localization of regional circumferential wall strain characteristics as a predictor for potential future events.

Dietary manipulations of murine models have emerged as a useful experimental tool,²¹⁰ and such manipulations are known to impact factors key to development of arterial aneurysms.²¹¹ Obesity has been shown to increase peri-aortic adipose tissue inflammation leading to enhanced incidence of AAA in the Ang II murine model. We sought to characterize the effect of these changes on the aortic wall elasticity and association with enhanced aneurysm formation. Under the conditions of our experiments we found no differences between normal chow mice and high fat mice in any region along the aorta preoperatively. This suggests that the hyperlipidemic state associated with short term high fat feeding alone does not significantly alter the structural components of the aortic wall, but rather enhances the inflammatory and remodeling response associated with Ang II treatment. There was no significant difference between atherosclerotic plaque deposition on the aortic wall observed at autopsy between the normal chow and high fat animals. However, longer term high fat feeding as well as more advanced age may lead to enhanced atherosclerotic changes that can result in loss of aortic elasticity and increased risk for aneurysmal degeneration, but this remains to be characterized in future investigations.

Potential parallel applications for high frequency ultrasound are numerous. Our methods could be used to quantify circumferential strain in other murine models of disease and after interventions (e.g. statins, anti-hypertensive therapies, anti-inflammatory agents, etc.). Furthermore, most AAAs are asymmetric. It has been shown that asymmetry/shape has a substantial influence on the distribution of wall stress within the aneurysm,¹⁹⁰ and our strategies

could be expanded to interrogate the effect of asymmetric circumferential strain on AAA formation and rupture. Clinically there are significant shortfalls with current AAA management pathways, as the fundamental strategy of using size imaging as a stand-alone to diagnose and provide prognostic information regarding AAA does not provide complete data to identify which AAAs are most likely to continue to increase in size and be at risk for rupture. A more complete ability to predict AAA progression may allow improved AAA management.²¹²

A limitation of this study is that blood pressure was not closely measured in the mice. However, it has been reported previously that blood pressure does not affect Ang II related AAA development²¹³, and it is likely that for the range of blood pressures for the experimental animals the impact on strain is minimal. Systemic blood pressure is necessary for calculation of stiffness index and other relevant hemodynamic parameters. We assumed that at day 3 no animals would develop gross aneurismal changes, and that any difference in strain measured would be from the effect of Ang II alone rather than contributions from structural changes from an enlarging aneurysm/thrombus. The combination of high fat feeding and high Ang II dose led to unexpected aneurysm development at day 3. It is possible that by reducing the dose of Ang II we could decrease the rate of early aneurysm formation and better determine the effects of the Ang II treatment alone. Finally, due to the resolution limitations of current ultrasound technology, we were unable to accurately differentiate between the intra-luminal and extra-luminal aortic wall. For these reasons, we only calculated and reported the circumferential strains (not radial strain) on the intra-luminal wall, which was clearly visible in the ultrasound images.

In conclusion, the combination of high-frequency ultrasound imaging and speckle tracking allows the quantification of the changes in circumferential strain of the aorta during AAA development in apoE^{-/-} mice infused with Ang II. The combination of these techniques demonstrated that the aorta significantly stiffens (has decreased strain) shortly after the infusion of Ang II into apoE^{-/-} mice and after aneurysm formation in these mice. Measurements at later time points revealed progressive decrease in strain in the supra-renal aorta, which is the segment most likely to be involved in aneurysm formation. The delineation of the biomechanical factors and natural history of AAA development in animal models of the disease in combination with our continuously improving armamentarium of biologic assays will provide insights into the factors associated with initiation and propagation of AAAs in humans.

4.5 Conclusions

The methodologies used to measure strains in this chapter represent a novel and useful approach to noninvasively determine wall strains in the murine model. In this chapter, we demonstrated that there are baseline differences in strain amongst aortic regions with the greatest arterial strain in the ascending aorta region. Additionally, we found that mechanical strains in several regions were reduced very soon after the induction of aneurysms in the apoE^{-/-} mouse model infused with Ang II. These reductions in strain demonstrate that our method can measure small enough strain changes to determine changes in a murine model with small sample sizes and that this method is sensitive enough to determine changes in aortic strains due to disease conditions. This method enables research that noninvasively examines changes in vascular strains in a variety of biological systems. In the following chapters of this dissertation, this method is applied to a novel model of vascular intimal hyperplasia.

5 Objective 2: Determination of the relationship between circumferential wall strain and intimal hyperplasia

Portions of this section are taken from The Journal of Vascular Surgery, In Press, John T Favreau, Chengwei Liu, Peng Yu, Ming Tao, Christine Mauro, Glenn R. Gaudette, C. Keith Ozaki, “Acute reductions in mechanical wall strain precede the formation of intimal hyperplasia in a murine model of arterial occlusive disease”, Copyright 2013, with permission from Elsevier (See Appendix A).

5.1 Introduction

In the first aim of this dissertation, we validated a novel method for measuring mechanical strains on the murine arterial wall using high frequency ultrasound. Having demonstrated the accuracy and precision of our method compared to another measurement technique, and applied our method to an *in vivo* model, our next objective is to determine what relationship exists between cyclic circumferential wall strain and intimal hyperplasia (IH).

In this chapter, we hypothesize that there is a direct positive relationship between reduced cyclic arterial wall strain and the formation of IH. To test this hypothesis, we combined a validated murine model of IH³⁷ with our method for measuring arterial wall strains *in vivo*⁴⁴ to unravel the relationship between wall strain and neointima formation.

5.2 Materials and methods

5.2.1 Study design

All animal experimental protocols used in this study complied with the Guide for the Care and Use of Laboratory Animals ²¹⁴ and were approved by our local Institutional Animal Care and Use Committee. Male C57BL/6J mice (n=10) were purchased from the Jackson Laboratory (Bar Harbor, ME) and maintained on a normal chow diet.

5.2.2 Mouse model

At eight weeks of age, general anesthesia was induced with 2% isoflurane gas in an induction chamber and then maintained via a nose cone with 1.0-1.5% isoflurane gas. A focal stenosis was created in the left distal common carotid artery (LCCA) as described previously.³⁷ Briefly, the LCCA was exposed and visualized via a midline incision using a surgical microscope (OPMI-MD, Carl Zeiss, Germany). A focal stenosis was created approximately 1mm proximal to the common carotid bifurcation by tying a 9-0 nylon suture around both the artery and a blunt 35 gauge needle (external diameter of 0.14 mm, item No. NF 35 BL; World Precision Instruments, Inc., Sarasota, FL). After removal of the needle, the vessel diameter was reduced by ~78%. Our previous studies have shown this diameter reduction will produce a reduction in luminal flow of ~85%.³⁷ After creation of the focal stenosis, the surgical incision was closed and mice were allowed to recover.

5.2.3 Ultrasound data acquisition

Ultrasound cine loops of both the LCCA and right common carotid artery (RCCA) were recorded preoperatively and on post-op day 27. For ultrasound acquisition, mice were anesthetized using 1-2% isoflurane and body temperature was maintained on a moveable platform heated to 37 °C. A chemical depilatory was used to remove hair from the neck and pre-warmed Aquasonic 100H ultrasound transmission gel (Parker Laboratories, Inc., Fairfield, NJ) was applied. Using a Visualsonics Vevo 2100 Ultrasound Imaging System with MS700 50 MHz linear array transducer (Visualsonics Inc., Toronto, ON, Canada), cine loops of cross-sections of both the RCCA and LCCA were recorded. For the LCCA, loops were recorded 1mm, 2mm and 3mm proximal to the focal stenosis and at similar locations for the RCCA (Figure 5-1). Cine loops for all time points and locations were recorded at 432 frames/s with 500 consecutive

frames acquired. Efforts were made to maintain depth of anesthesia with a heart rate of at least 475 beats/minute and a respiratory rate of 75-100 breaths/minute during all data collection.

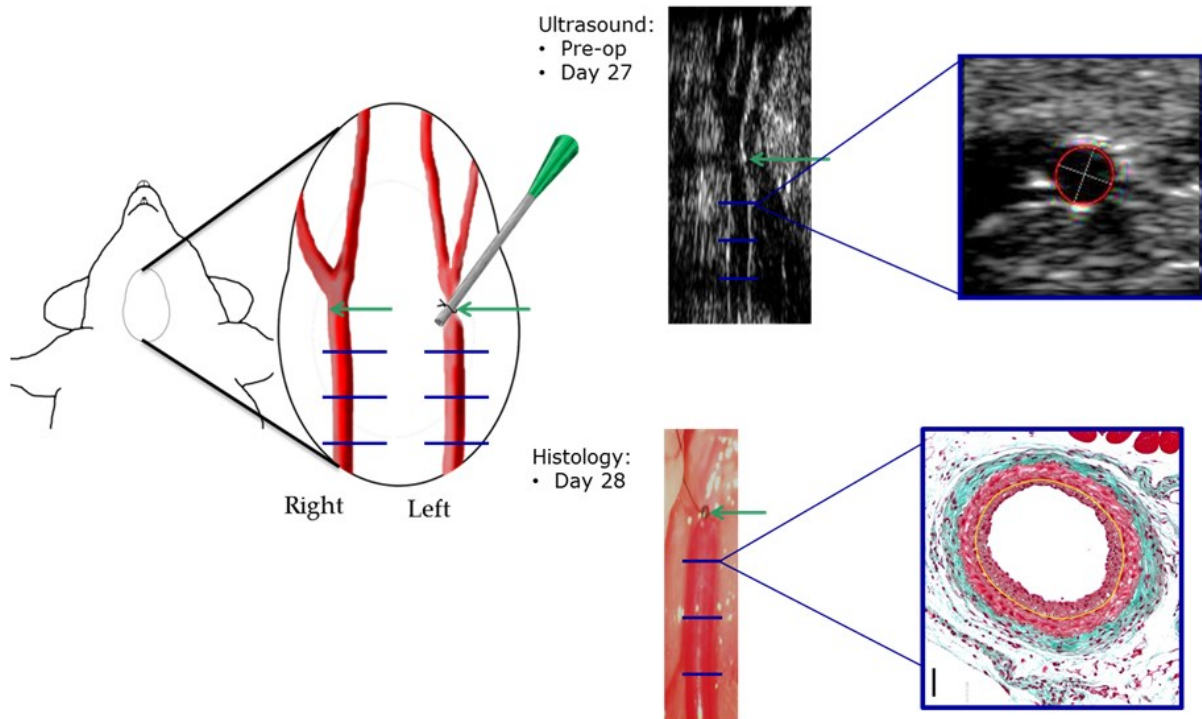


Figure 5-1: Objective 2 study design. A focal stenosis (green arrow) was made in the left common carotid artery 1mm proximal to the carotid bifurcation. Mechanical (via ultrasound) and histological parameters were assessed 1mm, 2mm, and 3mm proximal to the focal stenosis on the left side, and in corresponding locations on the contralateral side (blue lines).

5.2.4 Strain calculations

Ultrasound cine loops were loaded into VevoVasc software (Version 3.6.2.0, Visualsonics Inc.) and vascular walls were traced using the automatic edge detection tool. Movement of the carotid artery wall was then tracked through at least 5 cardiac cycles and vessel area was recorded over time. From the resulting area change curves, ideal vessel diameters were computed (assuming a circular cross-section) and circumferential wall strain curves (using Green's definition²¹⁵) were calculated across the 5 cardiac cycles. Average magnitude of cyclic wall strain from diastole to systole was calculated for each animal, time point and location.

Additionally, mean diastolic and systolic cross-sectional areas were computed and reported for each time point.

5.2.5 Tissue Harvest and Histology

On post-op day 28, mice were again anesthetized using 1-2% isoflurane anesthesia. The chest cavity was opened and the left ventricle of the heart was punctured with a 25 gauge cannula and blood was drained through an incision in the inferior vena cava. Lactated ringer's solution was perfused under physiological pressure (100 mmHg) for 2-3 minutes then replaced with 10% buffered formalin for 5 minutes. The LCCA and RCCA were collected and fixed in the same formalin solution overnight.

Tissue specimens were then dehydrated, cleared through several changes of ethanol and xylene and embedded in paraffin. Tissue cross-sections (6- μ m thick) were collected throughout the tissue. Using the carotid bifurcation as a reference for the RCCA and the focal stenosis as a reference for the LCCA, tissue cross-sections were collected 1mm, 2mm and 3mm proximal to the focal stenosis and at corresponding locations on the right (the same locations at which wall strain was assessed using ultrasound). At each location, Masson's trichrome stain was employed to visualize arterial structures via a microscope with high resolution camera (Axio A1 microscope with vision 4.7 software; Carl Zeiss). The lumen dimensions, internal elastic lamina (IEL) length and external elastic lamina (EEL) length were identified and traced. Assuming a circular cross-section *in vivo*, the areas and radii of the lumen, IEL and EEL were determined. From these values, mean intimal thickness, wall thickness, and intima:media thickness ratio were calculated.

5.2.6 Statistics

Data are presented as mean and standard error of the mean. All statistical analyses were completed in Sigmaplot version 11 (Systat Software Inc., San Jose, CA, USA). Statistical comparisons amongst spatial regions for strain, histological measurements and diameters were performed using a one way ANOVA followed by a Tukey post-hoc test. Differences between pre-op and post-op day 28 timepoints and between contralateral control and experimental artery were determined using a paired t-test (paired by animal). Statistical powers are reported for all negative statistical results. $P < 0.05$ was considered significant for all tests.

5.3 Results

All animals survived surgery to tissue harvest. Three of the 10 mice had occluded LCCAs on harvest and their morphology data were not included in any of the analyses. Histology was available on all of the remaining animals. Due to technical difficulties related to visualizing the relatively low flow artery and edema, some day 27 strain data was unusable and thus is missing. The baseline data for these animals was included in the strain analyses. Table 5-A summarizes the data available and used for the following analyses.

Table 5-A: Sample sizes used for strain and histological analyses

Timepoint	2mm Strain (# of Regions)	3mm Strain (# of Regions)	4mm Strain (# of Regions)	Histology (# of animals)
Day 0	10	10	10	
Day 27	8	8	8	
Day 28				7

5.3.1 Wall strain analysis

Wall strains at baseline (pre-op) were consistent in all regions of both the left and right common carotid artery with no significant differences (Figure 5-2; $p=0.56$; Power: 0.22). At day 27, strains were reduced compared to pre-op measurements ($p<0.001$). Strains on the contralateral artery remained unchanged compared to pre-op strains at day 27 ($p=0.719$; Power: 0.05). No regional differences in strain were seen amongst either the stenosis or contralateral locations at any time point.

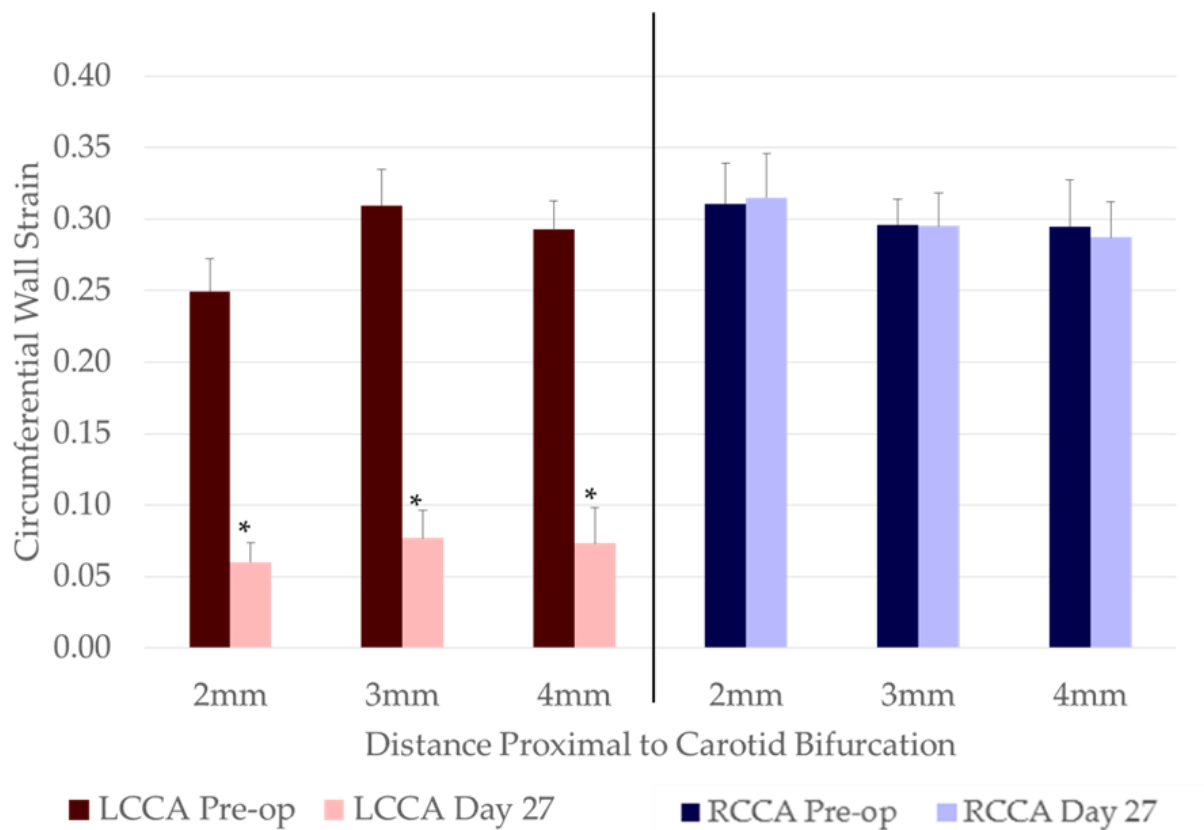


Figure 5-2: Regional differences in strain. Wall strains were assessed on the left (stenosed) and right (unaltered) common carotid artery in the regions shown in Figure 5-1. No differences amongst spatial locations were found on either side at any time point. (n=8 in all groups) *indicates $P<0.05$ compared to pre-op values (tested via paired t-test).

5.3.2 Histological analysis of wall adaptations

Histological analysis of tissues collected at day 28 was completed in all animals with a patent LCCA (n=7). Intimal thickness and wall thickness were computed at 2, 3 and 4 mm

proximal to the carotid bifurcation (regions which correspond to those where ultrasound data was acquired). IH occurred near the focal stenosis of the LCCA, but none was observed in the contralateral RCCA (Figure 5-3A). No regional differences were found in any calculated parameter amongst the three spatial regions. Mean wall thickness of the LCCA tended to be higher than that of RCCA, with a significantly 56% thicker wall 3 mm proximal to the bifurcation ($P = 0.012$) (Figure 5-3B).

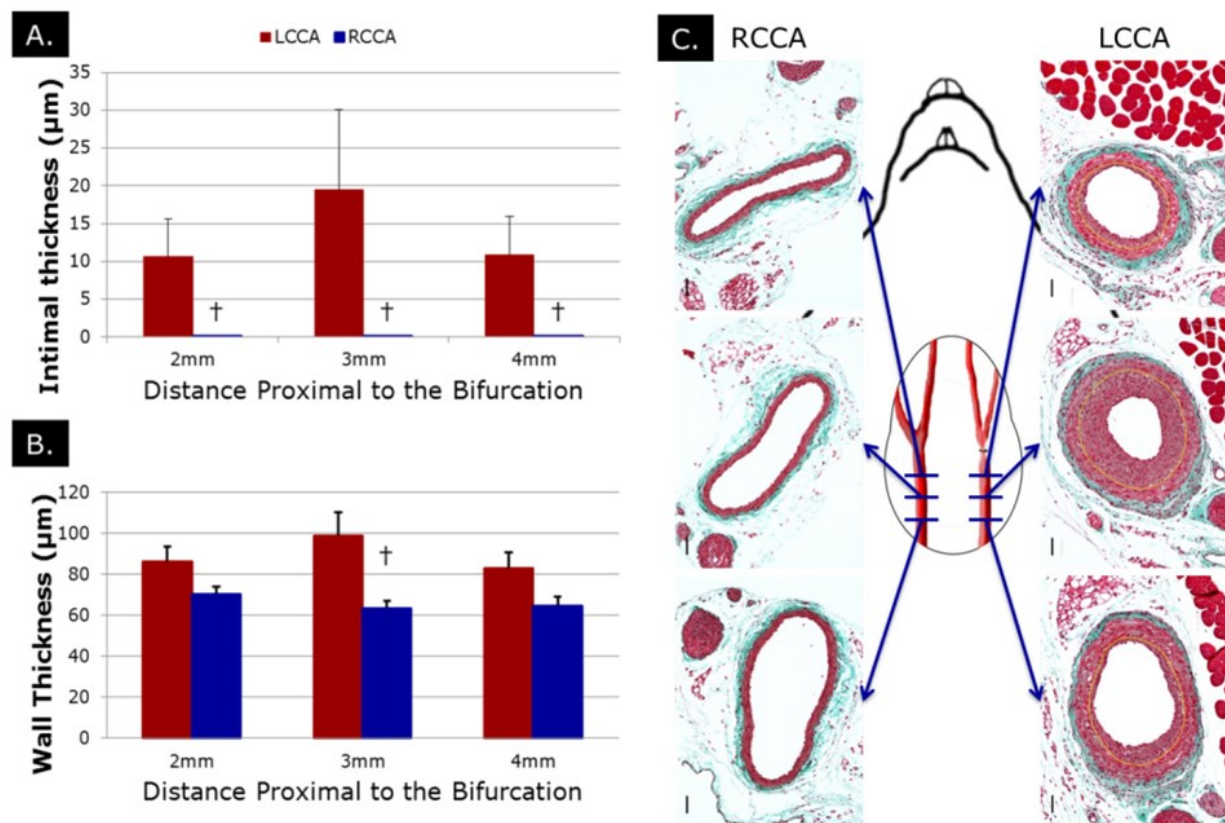


Figure 5-3: Morphological analysis of day-28 carotid arteries. (A) The intimal thickness of LCCA was significantly higher than that of RCCA at the same location. (B) LCCA tends to have higher wall thickness than its counterpart RCCA. (C) Representative histology for each of the three regions on the LCCA and RCCA. † indicates $P < .05$ compared to RCCA value at the same cross-sectional location (tested via paired t-test; $n=7$ in all groups).

5.3.3 Temporal progression of arterial cross-sectional areas

Arterial cross-sectional areas at both diastole and systole were assessed pre-op, and at post-op day 27. Since no differences among spatial positions of either the LCCA or RCCA were

noted, strain values for all regions were analyzed together. Diastolic cross-sections in all spatial regions (2, 3 and 4 mm proximal to the carotid bifurcation) on the focal stenosis side were decreased at post-op day 27 compared to pre-op area ($p=0.003$). On the contralateral (right) side, diastolic areas increased from pre-op to post-op day 27 ($0.10 \pm 0.01 \text{ mm}^2$ vs. $0.14 \pm 0.01 \text{ mm}^2$; $p<0.001$)

Systolic cross-sectional areas were the same for the LCCA and RCCA at pre-op ($0.15 \pm 0.01 \text{ mm}^2$ vs. $0.15 \pm 0.01 \text{ mm}^2$; $p=0.50$; Power: 0.05). Systolic cross-sectional areas in the LCCA were decreased compared to pre-op at post-op day 27 ($0.08 \pm 0.01 \text{ mm}^2$; $p<0.001$). In the RCCA, systolic cross-section increased compared to pre-op at day 27 ($0.20 \pm 0.01 \text{ mm}^2$; $p=0.01$) (Figure 5-4).

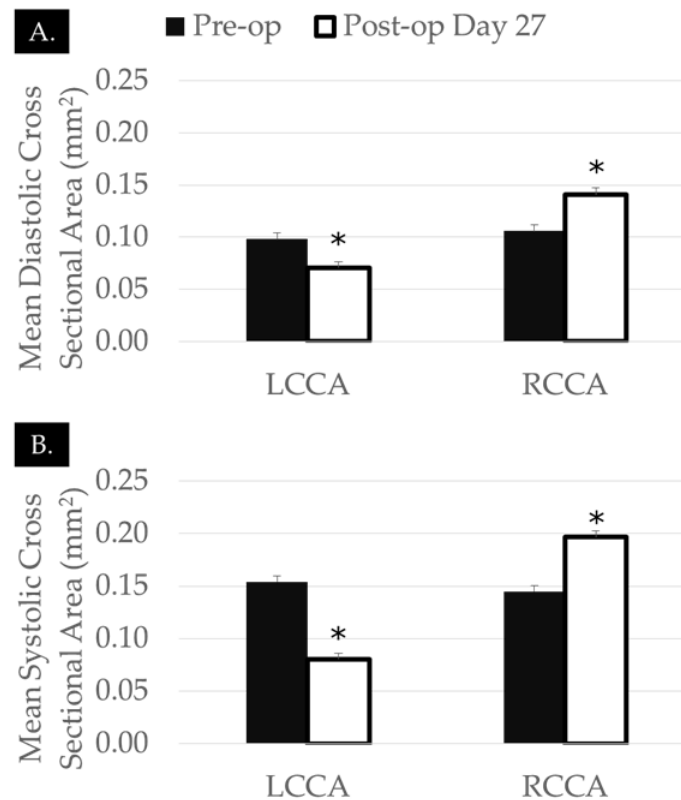


Figure 5-4: Changes in (A) diastolic and (B) systolic lumen area. *Indicates $P < .05$ compared to pre-op values (tested via paired t-test; $n=8$ in all groups)

5.3.4 Relationship between Day 27 strain and Histological outcome

As the results above demonstrate, we have found that there are no regional differences in circumferential wall strain amongst the 2mm, 3mm and 4mm locations proximal to the focal stenosis on either the stenosis vessel or contralateral control vessel. Additionally, we found no regional differences in either wall thickness or intimal thickness histological outcome amongst any of the regions. Consequently, we analyzed the relationship between day 27 strain and histological outcome as an aggregate of all of the regions, ignoring distance from the focal stenosis.

Qualitative analysis of a plot of circumferential wall strain vs. intimal thickness shows that all regions have reduced strain values at day 27. Further, regions with high amounts of intimal hyperplasia appear to have lower strains compared to those with no intimal hyperplasia which exhibit a wide range of strains. Finally, we once again observed no trends toward differences amongst the three regions.

Given the qualitative results in Figure 5-5, the differences in intimal thickness outcome were analyzed between regions with low strain and those with high strain. By examining a histogram of day 27 strains (Figure 5-6A), it was observed that the majority of strain values are in the range of 0.01- 0.08 and appear to be normally distributed. In Figure 5-6B, the neointima formation in the 4 regions that have high strains (>0.08) was compared. Although no statistical differences occur between the low and high strain groups in either the wall thickness ($p=0.357$) measure or intimal thickness ($p=0.145$) measure, there appears to be a trend toward increased intimal and wall thickness in the low strain group. Since only 4 regions fell into the high strain

group, lack of statistical significance here could be due to a type 2 statistical error given that statistical power for both tests was only 0.05.

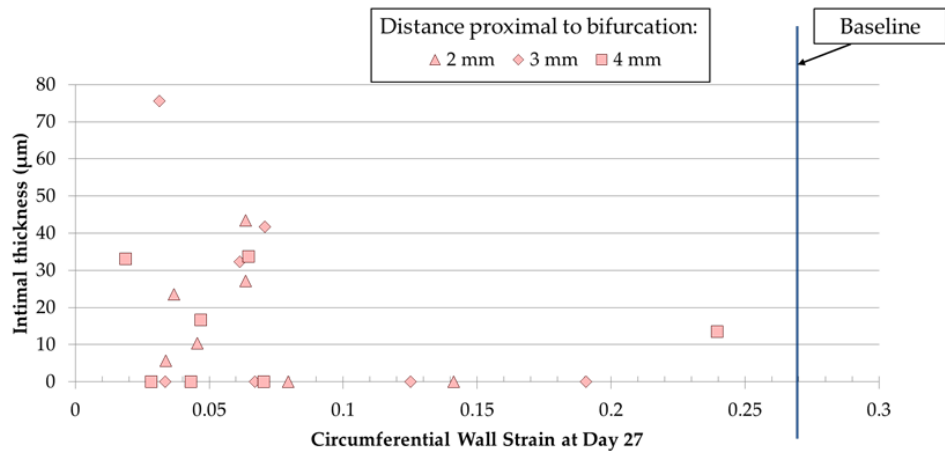


Figure 5-5: Relationship between day 27 strain and day 28 intimal thickness. Although there is a wide range of regions with low intimal thickness, regions with significant neointima formation are confined to the low strain range.

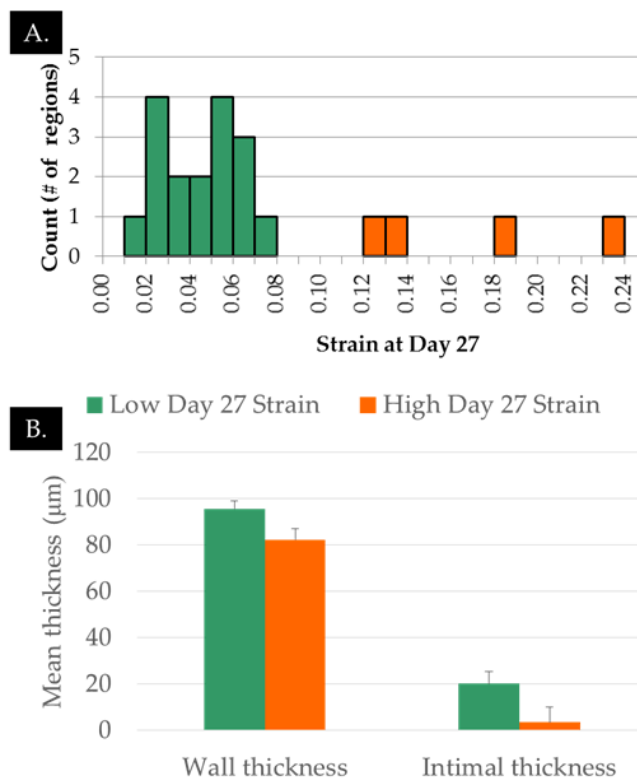


Figure 5-6: Quantitative relationship between day 27 strain and neointima formation. (A) Histogram analysis of wall strains in all regions at day 27. (B) Analysis of wall thickness and intimal thickness between regions of low strain (<0.1) and those of high strain (>0.1).

5.4 Discussion

In Objective 1 (Chapters 3 and 4), we demonstrated that our novel methods are capable of measuring circumferential wall strains in the murine vasculature. In the present chapter we demonstrate that there is a relationship between regional circumferential wall strain and the formation of intimal hyperplasia. In a previous study in our collaborator's lab, we found that using the murine focal stenosis model results in a ~85% reduction in wall shear stress and a subsequent formation of IH in the vessel 1 month later.³⁷ This finding is consistent with the large body of literature demonstrating a correlation between low wall shear stress and IH.^{82, 104, 134, 162, 216-224} Additionally, in this previous study, we showed that immediately after creation of the focal stenosis, there may be a trend toward strain reduction (as measured by an optical method) in the region proximal to the stenosis.³⁷ In this objective, we go on to demonstrate that a reduction in strain exists in nearly all regions at Day 27 post focal stenosis creation.

Oscillatory wall strain is a measure of how much the vessel wall dilates from diastolic to systolic pressure in the average cardiac cycle. Given that the stress in the vessel wall is related to strain through the mechanical properties of the wall, reductions in mechanical strain observed herein are likely due to either changes in wall stiffness or changes in wall stress. Increases in vascular wall stiffness would result in the vessel wall stretching less between the diastolic and systolic blood pressures—thereby reducing oscillatory wall strain. Alternatively, the blood pressure itself or the wall thickness could change and affect the wall stress, resulting in changes in wall strain. Increases in wall thickness or decreases in pulse pressure could both result in reductions in wall strain. Interestingly, changes in mechanical strain are not observed in the contralateral control artery. This finding is confounded by the data in Figure 5-4 that shows an

increase in both contralateral diastolic and systolic areas. This suggests that although the vessel area is increasing, both diastolic and systolic area are increasing proportionally to maintain a constant cyclic wall strain. On the stenosis (left) side, a decrease in both systolic and diastolic area was observed in addition to the reduction in strain, although the decrease appears to be greater in systolic area compared to diastolic area.

A major limitation of the studies in this chapter is that the blood pressure and arterial wall thickness were not assessed. Ideally, blood pressures and wall thicknesses would be measured along with strain on both the experimental and contralateral arteries. Due to the small size of the murine blood vessels, the outer wall of the carotid artery cannot be differentiated from the surrounding tissues via contemporary ultrasound. Additionally, measurement of blood pressures within the vessel is limited by the arterial size. Given that the mouse carotid artery is typically about 300-400µm in lumen diameter^{37, 225} Insertion of even the smallest commercially available pressure catheters (300 microns in diameter, Fiso LS 0.9 French, Harvard Apparatus, Holliston, MA) into the carotid artery would significantly impede blood flow and likely alter the entire *in vivo* model.

Despite the limitations of this study, the results show a promising trend toward a relationship between mechanical strain and intimal hyperplasia in our murine model. The data in Figure 5-6 indicate a division of regions showing low or high strain and a trend toward low strain regions having more intimal hyperplasia. Given that nearly 2/3 of the regions analyzed demonstrated IH at day 28, it is possible that a more clear relationship could be found at earlier time points when less IH formation had occurred. In Specific Aim 3 (Chapters 6 and 7), we will further assess the temporal relationship between IH and cyclic wall strain.

6 Objective 3A: Determine the temporal progression of wall strain in the focal stenosis model

Portions of this section are taken from The Journal of Vascular Surgery, In Press, John T Favreau, Chengwei Liu, Peng Yu, Ming Tao, Christine Mauro, Glenn R. Gaudette, C. Keith Ozaki, “Acute reductions in mechanical wall strain precede the formation of intimal hyperplasia in a murine model of arterial occlusive disease”, Copyright 2013, with permission from Elsevier (See Appendix A).

6.1 Introduction

In chapter 5 of this dissertation, we demonstrate that there is a relationship between reductions in mechanical strain and the formation of IH in a murine model. Although significant differences as a function of distance proximal to the focal stenosis were not observed in either strain or IH measurements, our data suggest that there may be a relationship between mechanical strain and IH in this model. To further understand this relationship, in this chapter we will aim to further delineate the progression of wall strain in this model. To accomplish this, wall strain was assessed at time points earlier than 28 days to determine when strain reductions occur in relation to IH at 28 days post-op. By examining more time points, we show how early detectable changes in strain occur in this model and gain a better understanding of when strains are reduced.

6.2 Materials and methods

6.2.1 Experimental Design

We will re-use histological data collected for the animals in Objective 2 and assess ultrasound data collected in the same animals at the day 4 timepoint. Arterial wall strains were assessed in the same locations described in Chapter 5 using our ultrasound-based methodology at day 4 after the surgical procedure. Day 4 strain outcomes were compared to day 28

histological outcomes presented in Objective 2. The experimental design for this aim is shown in Figure 6-1.

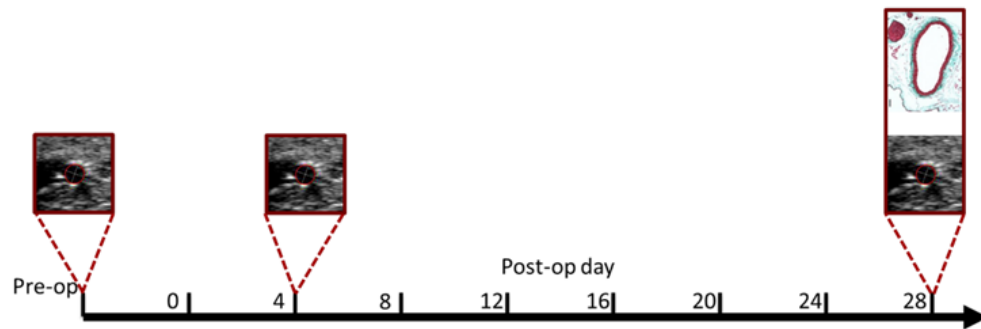


Figure 6-1: Schematic of Aim 3A study. A focal stenosis will be created using the methodology described in Chapter 5. Early strains, at day 4, will be compared to histological outcome at day 28.

6.2.2 Relationship between early strain and eventual intimal hyperplasia

Animals from Objective 2 are re-used for this chapter to determine the temporal progression of wall strains in this model. Ultrasound cine loops from day 4 post-op were collected and strain analyses were performed as described in Section 5.2.4. Cyclic wall strain, diastolic lumen area and systolic lumen area were assessed for the day 4 time point.

6.2.1 Statistics

Data are presented as mean and standard error of the mean. All statistical analyses were completed in Sigmaplot version 11 (Systat Software Inc., San Jose, CA, USA). Statistical comparisons amongst spatial regions for strain, histological measurements and diameters were performed using a one way ANOVA followed by a Tukey post-hoc test. Differences between pre-op, post-op day 4 and post-op day 28 time points were performed using a repeated measures ANOVA. Differences between contralateral control and experimental artery were

determined using a paired t-test (paired by animal). Statistical powers are reported for all negative statistical results. $P < 0.05$ was considered significant for all tests.

6.3 Results

All animals survived surgery to tissue harvest. Three of the 10 mice had occluded LCCAs on harvest and their morphology data were not included in any of the analyses. Histology was available on all of the remaining animals. Due to technical difficulties related to visualizing the relatively low flow artery and edema, some day 4 strain data was unusable and thus is missing. The baseline data for these animals was included in the strain analyses. Table 6-A summarizes the data available and used for the following analyses.

Table 6-A: Sample sizes used for strain and histological analyses on the LCCA. *The lumen of some vessels were not visible via ultrasound and were therefore excluded. † 3 arteries were fully occluded at day 28 and therefore were not used for histological analysis

Timepoint	2mm Strain (# of Regions)	3mm Strain (# of Regions)	4mm Strain (# of Regions)	Histology (# of animals)
Day 0	10	10	10	
Day 4	9*	8*	9*	
Day 27	8*	8*	8*	
Day 28				7†

6.3.1 Wall strain analysis

Wall strains at baseline (pre-op) were consistent in all regions of both the left and right common carotid artery with no significant differences (Figure 5-2; $p = 0.56$; Power: 0.05). At day 4, all regions on the focal stenosis (left) side were significantly reduced compared to pre-op strains ($p < 0.001$) while no changes in strain occurred on the contralateral (right) side ($p = 0.90$;

Power: 0.05). At day 27, strains remained reduced compared to pre-op measurements but did not significantly reduce further compared to strains at day 4 ($p=0.2$). Strains on the contralateral artery remained unchanged compared to pre-op strains at day 27. No regional differences in strain were seen amongst either the stenosis or contralateral locations at any time point.

6.3.2 Temporal progression of arterial cross-sectional areas

Arterial cross-sectional areas at both diastole and systole were assessed pre-op, and at post-op day 4 and day 27. Since no differences among spatial positions of either the LCCA or RCCA were noted, strain values for all regions were analyzed together. Diastolic cross-sections in all spatial regions (2, 3 and 4 mm proximal to the carotid bifurcation) on the focal stenosis side remained unchanged from pre-op to post-op day 4 ($0.10 \pm 0.01 \text{ mm}^2$ vs. $0.12 \pm 0.01 \text{ mm}^2$; $p=0.19$; Power: 0.96). However, diastolic cross-sectional areas were decreased at post-op day 27 compared to both pre-op area and post-op day 4 area ($0.07 \pm 0.01 \text{ mm}^2$; $p<0.001$). On the contralateral (right) side, diastolic areas increased from pre-op to post-op day 4 ($0.10 \pm 0.01 \text{ mm}^2$ vs. $0.13 \pm 0.01 \text{ mm}^2$; $p=0.009$) and remained increased at post-op day 27 compared to pre-op ($0.14 \pm 0.01 \text{ mm}^2$; $p<0.001$). Diastolic cross-sectional areas were statistically the same for the focal stenosis and contralateral arteries at pre-op and day 4, but contralateral cross-section was larger at post-op day 27 ($p<0.001$).

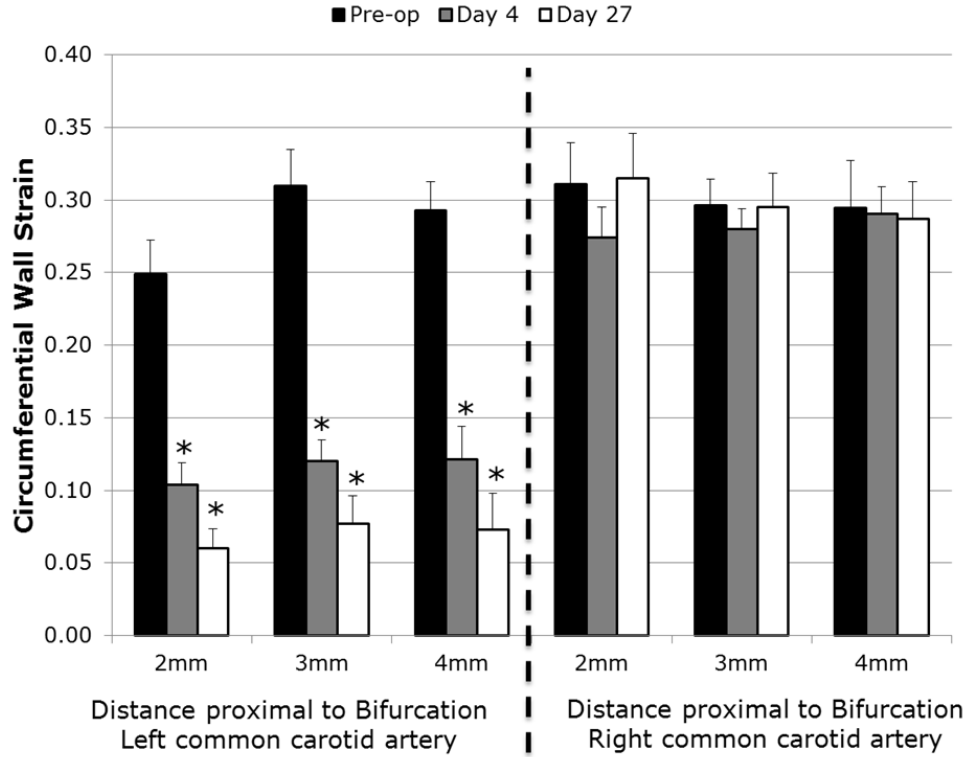


Figure 6-2: Regional differences in strain. Wall strains were assessed on the left (partially stenosed) and right (unaltered) common carotid artery in the regions shown in Figure 5-1. Average for each side indicates the average of all regions. No differences amongst spatial locations were found on either side at any time point. * indicates $P < 0.05$ compared to pre-op values ($n=8$ in all groups).

Systolic cross-sectional areas were the same for the LCCA and RCCA at pre-op (0.15 ± 0.01 mm² vs. 0.15 ± 0.01 mm²; $p=0.50$; Power: 0.05). Systolic cross-sectional areas in the LCCA were unchanged compared to pre-op at post-op day 4 (0.14 ± 0.01 mm²; $p=0.64$; Power: 0.9) but were decreased at post-op day 27 (0.08 ± 0.01 mm²; $p<0.001$). In the RCCA, systolic cross-section increased compared to pre-op at day 4 (0.17 ± 0.01 mm²; $p=0.004$) and continued to increase at post-op day 27 (0.20 ± 0.01 mm²; $p=0.01$) (Figure 5-4).

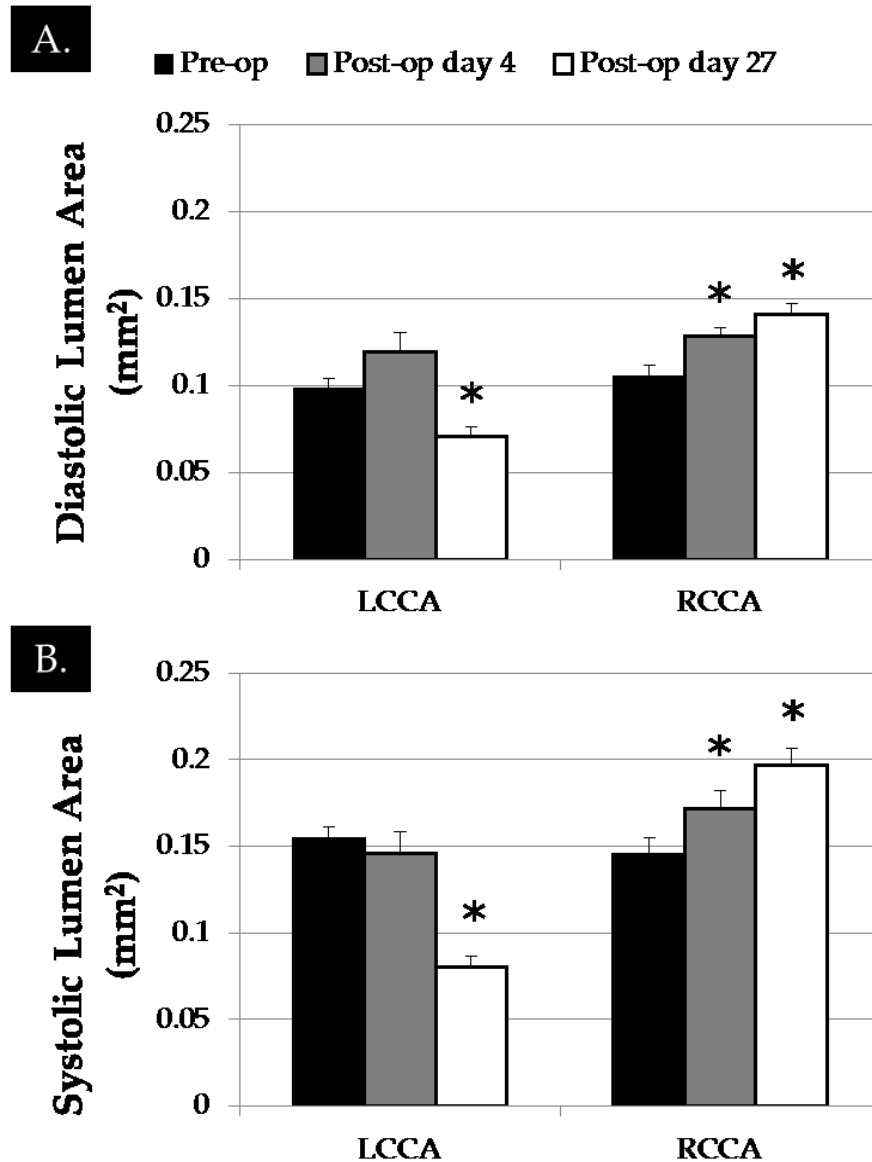


Figure 6-3: Changes in (A) diastolic and (B) systolic lumen area. *Indicates $P < .05$ compared to pre-op values; $n=8$ in all groups

6.3.3 Relationship between acute strain and subsequent intimal thickness

Analysis of the wall strain values in all regions at post-op day 4 using a histogram

demonstrated a range of results (Figure 6-4A). To further analyze the acute changes in wall

strain produced by this model, the LCCA data were divided into regions with strain >0.10

($n=13$) and those with strain ≤ 0.10 ($n=13$). The median was utilized as the threshold for the two

groups (the same cut off used in Aim 2). Of those regions with strains ≤ 0.10 at post-op day 4, all regions went on to form IH or to completely occlude by day 28. Regions with strain > 0.1 at post-op day 4, only 31% (4 regions) went on to form any detectable IH by day 28.

Diastolic cross-sections remained unchanged in the strain > 0.1 group from pre-op to day 4 ($0.10 \pm 0.01 \text{ mm}^2$ vs. 0.09 ± 0.01 ; $P=.93$; Power: 0.51) but were significantly reduced compared to pre-op at post-op day 27 ($0.06 \pm 0.01 \text{ mm}^2$; $P=.04$). Diastolic areas in the strain ≤ 0.1 group were increased from pre-op to post-op day 4 ($0.10 \pm 0.01 \text{ mm}^2$ vs. $0.15 \pm 0.02 \text{ mm}^2$) but returned to their pre-op levels at day 27 ($0.09 \pm 0.01 \text{ mm}^2$; $P=.40$ compared to pre-op; Power: 0.86; Figure 6-4B). Systolic areas, however, remained unchanged from pre-op to day 4 in both > 0.1 ($0.15 \pm 0.01 \text{ mm}^2$ vs. $0.12 \pm 0.02 \text{ mm}^2$; $P=.13$; Power: 0.99) and ≤ 0.1 ($0.16 \pm 0.01 \text{ mm}^2$ vs. $0.17 \pm 0.02 \text{ mm}^2$; $P=.89$; Power: 0.94) groups and both decreased below pre-op baseline by day 27 ($P=.005$ and $P=.01$, respectively; Figure 6-4C). The strain > 0.1 group had significantly smaller intimal thickness than the strain ≤ 0.1 group ($8 \pm 4 \text{ }\mu\text{m}$ vs. $32 \pm 7 \text{ }\mu\text{m}$; $P=.006$). Similarly, the strain > 0.1 group had both a smaller wall thickness ($82 \pm 7 \text{ }\mu\text{m}$ vs. $111 \pm 6 \text{ }\mu\text{m}$; $P=.009$) and intima:media area ratio (0.19 ± 0.10 vs. 0.81 ± 0.19 ; $P=0.006$; Figure 6-4D).

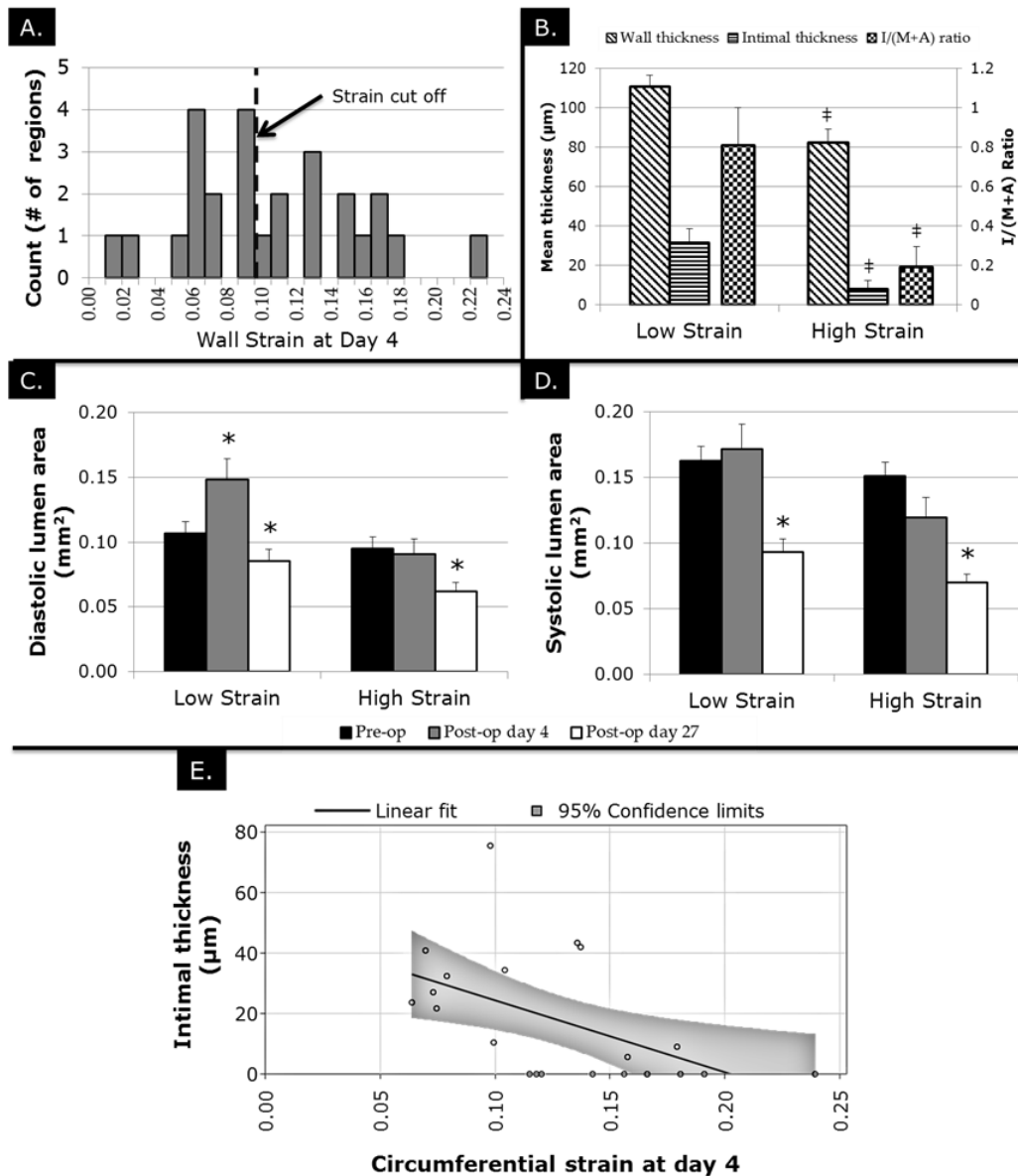


Figure 6-4: Differences in LCCA regions with low (<0.1) and high (>0.1) day 4 strain. (A) Histogram analysis showing the distribution of strain values amongst regions with cut off value. (B) Histological outcome of LCCA regions with low and high strain. ‡ indicates $P < 0.05$ vs. low strain values. (C) Changes in LCCA area at diastole over time in low and high strain groups. (D) Changes in LCCA area at systole over time in low and high strain groups. (E) Linear fit between wall strain at day 4 and intimal thickness at day 28 * indicates $P < 0.05$ compared to pre-op values.

6.4 Discussion

Given the results of Chapter 5, we believe that the temporal progression of strains may be important in regards to IH formation. Since we suspect that IH does not form before day 4, it is

important to determine exactly how early strain reductions occur and how early IH forms in this model. By experimentally demonstrating that strains reduce before IH forms, these experiments could effectively support our overall hypothesis: that reductions in oscillatory wall strain precede the formation of IH in a murine model of intimal hyperplasia.

Herein, we find that vessels with early (four days after focal stenosis) low wall strain consistently develop IH 28 days after creation of an outflow focal stenosis. Furthermore, only 31% of arteries that demonstrated high strain early went on to develop a measurable amount of IH. Such an analytical approach stands as a reasonable strategy to understand this small dataset. However, via multiple linear regression (intimal thickness as a dependent variable, wall strain and location proximal to the focal stenosis as independent variables), IH can be modeled as a linear combination of wall strain and distance proximal to the stenosis. Wall strain appears to account for the ability to predict IH ($P=0.007$) while location does not ($P=0.343$). Again, application of multiple linear regression to these data is limited by the small sample size and goodness of fit was suboptimal ($R^2=0.36$).

Wall strains measured herein were oscillatory, meaning that stretch from diastole to systole was measured. In order to better understand how wall strains are reduced in the short-term, diastolic and systolic areas were assessed. In the low strain group, a short-term reduction in diastolic lumen area was shown while no changes in systolic area were found. In the high strain group, no changes in diastolic or systolic area were observed. Our results demonstrate a decrease in LCCA vessel diameter in all mice by day 27 post-op, a finding that was previously reported at 2 weeks post-operatively in a similar flow model in rabbits.²²⁶ However, we reveal at

4 days that diastolic diameter increases significantly in animals that will eventually form IH, a phenomenon that has not been previously reported.

We speculate that the lower level of strain early is likely associated with altered vessel wall properties (biologic and mechanical). Though they have high heart rates, mice are known to have blood pressures similar to humans. Assuming a systolic pressure of 120 mmHg and a diastolic pressure of 80 mmHg, the 28 day wall modulus of elasticity (using a thin wall model based on the Law of Laplace and assuming linear vessel properties) yielded 152 ± 27 kPa for the low strain group and 100 ± 17 kPa in the high strain cohort. These computed elasticities fall in the same order of magnitude as those computed using more accurate (pressure based) measurements in previous studies.²²⁷ Although there was a trend toward higher modulus of elasticity in the low strain group, there is no statistical difference between the two groups ($P=.10$). These changes in strain could be directly related to changes in ECM or elastin content in the vessel wall. In particular, similar mechanical responses have been observed *in vitro* due to application of elastase to the vessel wall.²²⁸ Additionally, others have reported that expression of GAGs such as hyaluronic acid can be changed during an intimal hyperplastic response.²²⁹

The early reductions in mechanical strain demonstrated in this chapter have important implications to the relation between mechanical strain and IH in this model. Given that we do not expect significant IH to occur by the day 4 timepoint, it is possible that the early reductions in strain could be a result of important biological changes in the wall that occur as a result of the focal stenosis. In order to better understand the underlying cause of this reduction in strain, Chapter 7 will examine the temporal changes in IH and the acute (immediately post-op) changes in mechanical strain.

7 Objective 3B: Determine the temporal progression of intimal hyperplasia in the focal stenosis model

7.1 Introduction

The results presented in Chapter 5 (Objective 2) and Chapter 6 (Objective 3A) of this dissertation demonstrate compelling evidence for a temporal relationship between changes in wall strain and intimal hyperplasia in our murine model. In Chapter 6, we demonstrated that 100% of regions with low mechanical strain (<0.1) at day 4 went on to form IH by post-op day 28. In contrast, only 31% of regions with high mechanical strain (>0.1) went on to form IH. These findings suggest a promising link between changes in mechanical strain and IH.

From a mechanical standpoint, the reductions in mechanical strains seen at post-op day 27 (Chapter 5) were most likely due to the increased wall thickness, changes in diastolic diameter and/or changes in wall mechanical properties. Reduced strains observed at post-op day 4, however suggest a more mechanistic role of strain reduction in the formation of IH. Although it was not confirmed in the previous studies, we believed that it is highly unlikely that significant changes in wall thickness due to IH have occurred by post-op day 4, thus eliminating increased wall thickness as a key regulator of strain. An idea that is supported by previous literature in other murine models of IH.²³⁰⁻²³² In this chapter, we will assess IH formation via histology at day 4 to determine if the wall thickness has significantly changed by day 4 post-op.

A second possible cause of reduced strains at day 4 would be that placement of the suture immediately and directly causes reductions in mechanical strain. To assess this possibility, we measure strains immediately after focal stenosis creation and determine if reductions occur immediately upon focal stenosis creation. In this chapter, we aim to further understand the

relationship between oscillatory strain reduction and IH in order to present a clearer picture of the temporal progression of both mechanical strain and IH in this model.

7.2 Materials and methods

7.2.1 Experimental design

The validated focal stenosis model used in the previous aims was once again used in this objective. Thirty wild-type mice (C57BL/6J, The Jackson Laboratory) were randomly split into sham control (10 mice) and experimental (20 mice) groups. The experimental timeline for all Aim 3B studies is shown in Figure 7-1.

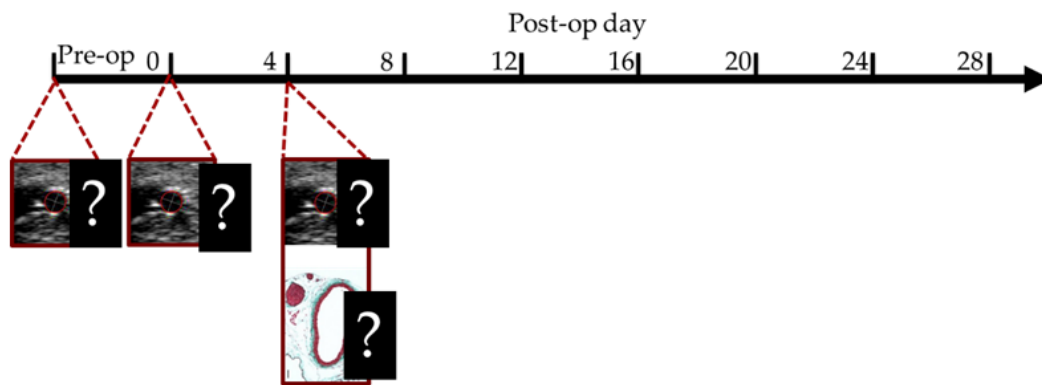


Figure 7-1: Experimental design for Aim 3B studies. Aim 3B animals were assessed via ultrasound at pre-op, immediately post-op and at post-op day 4. Animals were euthanized for histological analysis at day 4 to determine if significant IH is present at post-op day 4.

7.2.2 Ultrasound data acquisition

All sham and experimental animals were anesthetized and scanned using ultrasound 2-3 days prior to operation, immediately post-op and at post-op day 4 as described in section 5.2.3. Ultrasound cine loops were recorded at 2mm, 3mm and 4mm proximal to the carotid bifurcation on both the RCCA and LCCA. Data recorded in this Aim were collected using an MS700 ultrasound transducer and Visualsonics Vevo2100 system.

Each carotid was first visualized in longitudinal section to reveal the location of the bifurcation. At all time points, color Doppler cine loops were recorded in longitudinal section to

verify blood flow distal to the focal stenosis. After centering the probe on the carotid bifurcation, the probe was rotated 90 degrees to reveal a cross-sectional view of the artery. A stage micrometer was then used to move the probe 2mm, 3mm and 4mm with respect to the animal. At each location, 1000 frame cine loops were recorded at 534 frames per second for strain analysis. Ultrasound cross-sectional cine loops were analyzed using VevoVasc software using the same methodology described in Section 5.2.4.

7.2.3 Focal stenosis model

For experimental animals the same focal stenosis model employed in Chapter 5 was used (see section 5.2.2). For sham animals, the LCCA was surgically exposed following the same procedure used for experimental animals. After LCCA exposure, sham animal surgical sites were closed without manipulating the LCCA. All sham and experimental animals were scanned using ultrasound immediately post-op.

At post-op day 4, experimental, and sham animals were anesthetized and scanned via ultrasound for a final time. Animals were then transported to the O.R. and perfusion fixed as described in section 5.2.5.

7.2.4 Quantification of Intimal Thickness and Wall Thickness

In order to quantify wall morphology, a custom, semi-automated MatLab (Mathworks) script was developed to measure the cross-sectional area and average wall thicknesses of individual vascular layers. Sections of each vessel at 2, 3 and 4 mm proximal to the carotid bifurcation were stained using Masson's Trichrome (see Appendix B for protocol). Trichrome sections were imaged on a Leica DMLB2 upright microscope fitted with a DFC 480 c-mount microscope camera (Leica Microsystems, Buffalo Grove, IL). The resulting images were loaded into MatLab. To determine lumen area, the images were converted to grayscale and

automatically thresholded to yield a black and white image. The lumen was selected and the pixel area was automatically quantified. Internal elastic lamina, external elastic lamina and outer vessel perimeters were then manually traced in MatLab. Cross-sectional areas of each region (in pixels) were then converted to physical areas (based on a scaled image taken on the same scope camera and objective). Wall thickness and intimal thickness were computed as described in section 5.2.5. Thickness values were averaged from 3 sections in each artery. Appendix D provides further details on the methods used to determine intimal and wall thicknesses.

7.2.5 Assessment of cell type markers

In order to determine which cell types are present in the arterial wall at day 4, a triple immunohistochemical stain was developed to assess 3 different cell types related to the vascular wall and IH. Myosin heavy chain, a marker of contractile smooth muscle cells,²³³ was stained along with CD31 (PECAM-1),²³⁴ a marker of vascular endothelial cells. Finally, the presence of leukocytes was assessed using CD45, an antigen common to all leukocytes.²³⁵ Briefly, tissue sections were rehydrated through several changes of xylenes and ethanols. Heat induced epitope retrieval was completed using a pH 6.0 Citrate buffer and pressure cooker. Sections were permeabilized with triton-x, blocked with normal goat serum and simultaneously treated with mouse anti-myosin heavy chain, rabbit anti cd-31 and rat anti-mouse cd45 overnight at 4°C. Sections were then simultaneously treated with Alexa-fluor 488 goat anti-rat, Alexa-fluor 568 goat anti-rabbit and Alexa-fluor 633 goat anti-mouse. Sections were then counter stained with Hoechst 33342 dye and coverslipped (for details of the staining process used here, see

Appendix B). Healthy mouse heart sections and intestine sections were run simultaneously as positive and primary delete controls.

Stained sections were imaged on a laser confocal microscope (Leica TCS SP5, Leica Microsystems, Buffalo Grove, IL) with 4 photomultiplier tubes set to sequential mode. Maximum projection images of sections were imaged at 40x and 63x oil where appropriate.

7.2.6 Assessment of cell proliferation

To assess cellular proliferation, sections were immunostained simultaneously for alpha smooth muscle actin and ki-67, markers of smooth muscle cells and proliferating cells respectively. Briefly, tissue sections were rehydrated through several changes of xylenes and ethanols. Heat induced epitope retrieval was completed using a pH 9.0 tris-EDTA buffer and pressure cooker. Sections were permeabilized with triton-x, blocked with normal goat serum and simultaneously treated with mouse anti alpha smooth muscle actin and rabbit anti ki-67 overnight at 4°C. Sections were then simultaneously treated with Alexa-fluor 488 goat anti-mouse and Alexa-fluor 568 goat anti-rabbit. Sections were then counter stained with Hoechst 33342 dye and coverslipped (for details of the staining process used here, see Appendix B). Mouse intestine controls were run simultaneously as positive and primary delete controls. Sections were imaged with confocal microscopy as described in section 7.2.5.

7.2.7 Assessment of glycosaminoglycan synthesis

To assess GAG synthesis, the protocol described by Shukla and colleagues²³⁶ was used. Briefly, tissue sections were rehydrated through several changes of xylenes and ethanols and permeabilized with triton-x. Negative controls were digested with hyaluronidase in a sodium acetate buffer at 37°C for 1 hr. Tissue sections were then blocked with goat serum and bovine serum albumin and incubated simultaneously with hyaluronic acid binding protein and rabbit

anti-mouse versican overnight at 4°C. Sections were then treated with Alexafluor 488 goat anti-rabbit and Alexafluor 568 Streptavidin for 1 hr at room temperature. Sections were counterstained with Hoechst dye and coverslipped. Sections were imaged with confocal microscopy as described in section 7.2.5.

7.2.8 Statistical Analyses

Data are presented as mean and standard error of the mean. All statistical analyses were completed in Sigmaplot version 11 (Systat Software Inc., San Jose, CA, USA). Statistical comparisons amongst spatial regions for strain, histological measurements and diameters were performed using a one way ANOVA followed by a Tukey post-hoc test. Differences between pre-op, post-op day 4 and post-op day 28 time points were performed using a repeated measures ANOVA. Differences between contralateral control and experimental artery were determined using a paired t-test (paired by animal). Statistical powers are reported for all negative statistical results. $P < 0.05$ was considered significant for all tests.

7.3 Results

All animals survived to tissue harvest and ultrasound data acquisition for all regions and all time points was successful. Additionally, blood flow was evident distal to all focal stenoses at day 4 as assessed using color Doppler ultrasound. Strain data for all animals and regions was available and is reported below. Histology for half of the animals discussed in the methods section was sent to another lab for additional analysis. Thus, histology for 10 experimental animals and 5 sham animals is reported below.

7.3.1 Ultrasound strain analysis

Mean oscillatory wall strains in sham controls (sham LCCA), contralateral controls (experimental RCCA) and experimental LCCAs were consistent at pre-op (0.27 ± 0.01 vs $0.29 \pm$

0.01 vs 0.28 ± 0.01 , $p=0.50$; Power: 0.05). Shortly after focal stenosis placement (post-op day 0), LCCA strains did not change compared to pre-op in either the sham or experimental group (sham: 0.24 ± 0.02 , $p=0.24$ (Power: 0.12) vs. pre-op; experimental: 0.26 ± 0.01 , $p=0.43$ (Power: 1.0)). At post-op day 4, experimental LCCA strains were significantly reduced (0.18 ± 0.01) compared to pre-op values ($p<.0001$), sham controls (0.26 ± 0.01 ; $p<.001$) and contralateral controls (0.24 ± 0.01 ; $p<.001$). Strain data averaged by animal are shown in Figure 7-2.

Data were also analyzed by spatial region (2mm, 3mm and 4mm proximal to the bifurcation). No differences were found amongst the three spatial regions at any timepoint in either the sham control LCCA or the experimental LCCA. Experimental LCCA strains were reduced in all 3 regions at day 4 compared to pre-op, post-op day 0 and sham post-op day 4 data. Figure 7-3 shows the regional changes in mechanical strain.

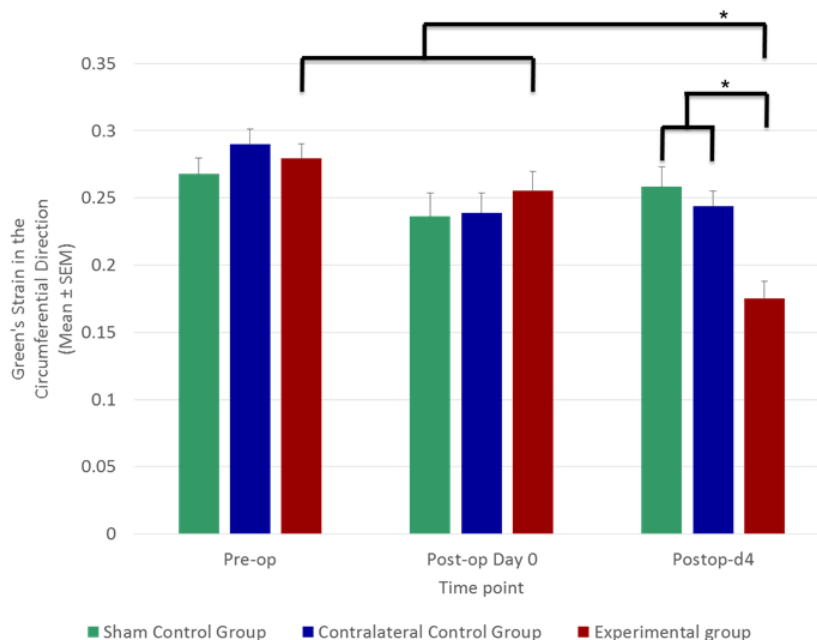


Figure 7-2: Average oscillatory wall strain. Average wall strain at Pre-op, Post-op Day 0 and Post-op day 4. Averages are for Sham control (n=10), Contralateral RCCA control (n=20) and Experimental LCCA (n=20) * indicates $p<0.001$; n=10 in sham group and n=20 in contralateral control and experimental group.

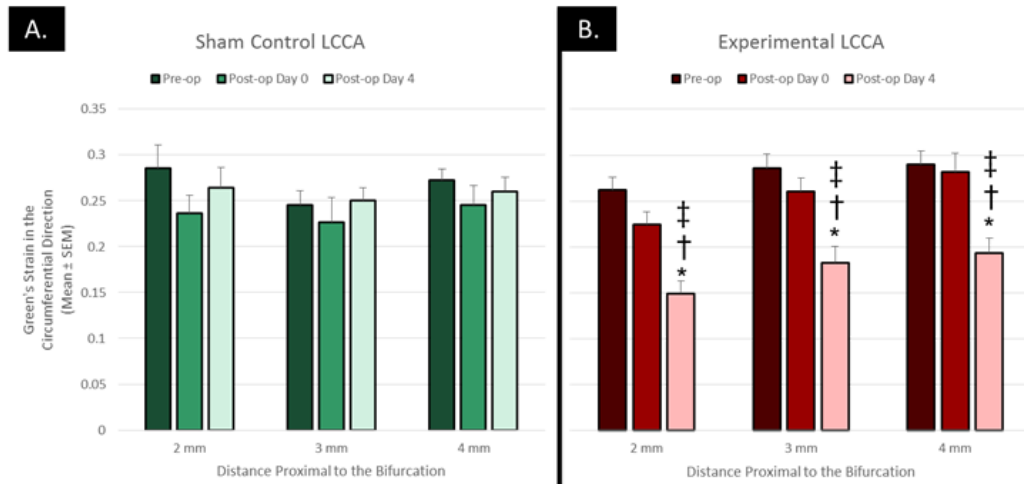


Figure 7-3: Average regional oscillatory wall strains. Regional wall strains were consistent amongst the three regions assessed at all time points. * indicates $p < 0.05$ vs. sham control. † indicates $p < 0.05$ vs. Pre-op. ‡ indicates $p < 0.05$ vs. post-op day 0. ; $n=10$ in sham group and $n=20$ in experimental group.

As in the data presented in Aim 3A, strains were significantly reduced in many animals at day 4. Figure 7-4 shows the changes in strain levels over time in the experimental animals vs. both controls. Individual data points (for each animal) are plotted to demonstrate progression of strain levels.

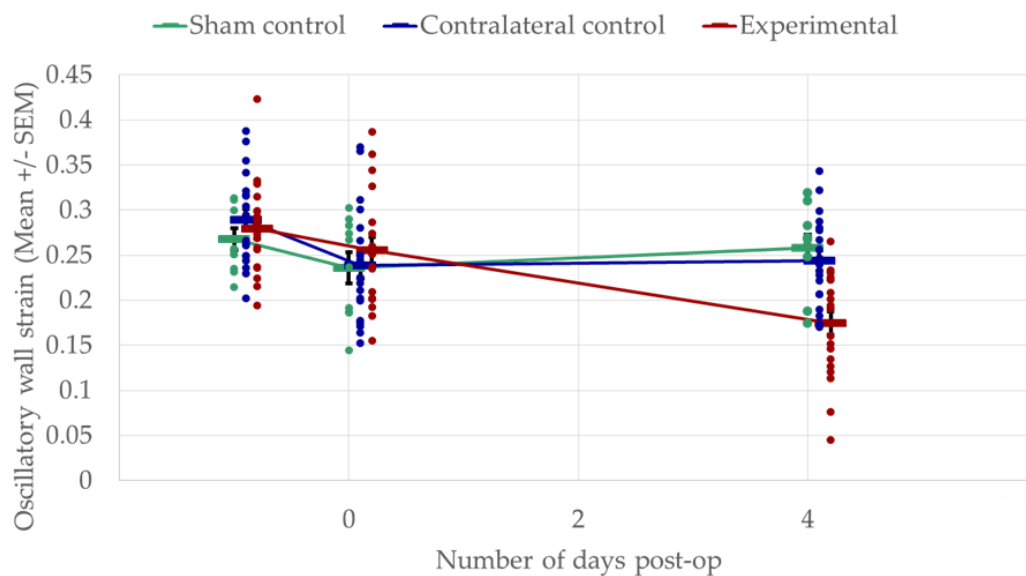


Figure 7-4: Progression of strain in control and experimental arteries. Strains in both control groups remain approximately constant throughout the study. Strains in experimental arteries, however, are reduced at day 4 post-op.

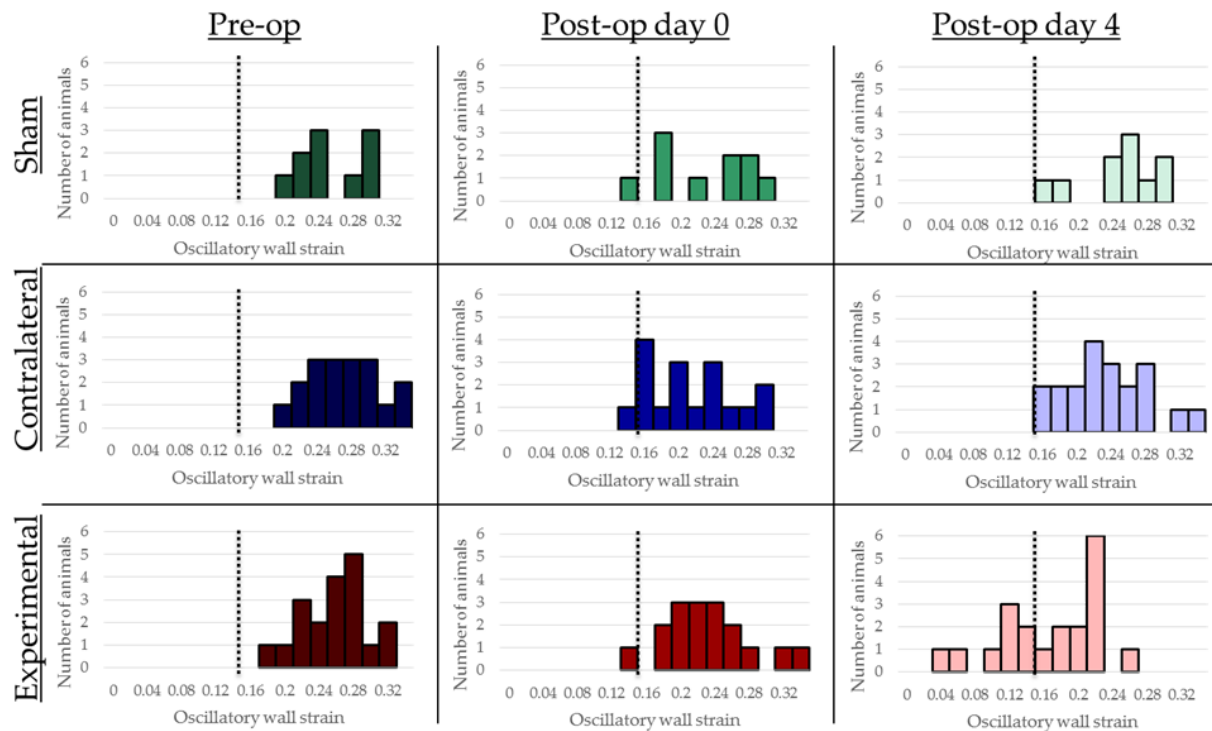


Figure 7-5: Histogram analysis of strain data at each time point. Strain levels were fairly consistent in all time points and groups except for the strain levels in the experimental animals at day 4 post-op. Dotted line through post-op day 4 data indicates the minimum control strain cut off used to analyze strain in the document.

7.3.2 Changes in wall cross-sectional area

Wall cross-sectional areas were measured at diastole and systole using ultrasound. Diastolic areas were the same in sham, contralateral and experimental arteries at pre-op ($0.13 \pm .02 \text{ mm}^2$ vs. $0.14 \pm 0.02 \text{ mm}^2$ vs. $0.15 \pm 0.02 \text{ mm}^2$; $p=0.36$; Power: 0.06). Similarly, systolic areas were the same in sham, contralateral and experimental arteries at pre-op ($0.20 \pm .03 \text{ mm}^2$ vs. $0.22 \pm 0.03 \text{ mm}^2$ vs. $0.22 \pm 0.03 \text{ mm}^2$; $p=0.17$; Power: 0.18). Sham control arteries remained unchanged from pre-op at both post-op day 0 and day 4. At post-op day 0, contralateral control diastolic and systolic areas were both significantly increased compared to pre-op ($0.18 \pm 0.04 \text{ mm}^2$, $p=0.002$ and $0.26 \pm 0.04 \text{ mm}^2$, $p<0.001$ respectively). Conversely, experimental diastolic and systolic areas were significantly decreased at post-op day 4 compared to pre-op ($0.12 \pm 0.02 \text{ mm}^2$, $p=0.17$ and $0.17 \pm 0.03 \text{ mm}^2$, $p<0.001$ respectively). At post-op day 4, contralateral control diastolic and

systolic areas returned to their pre-op levels ($0.15 \pm 0.04 \text{ mm}^2$, $p=0.80$ vs. pre-op; Power: 0.91 and $0.22 \pm 0.06 \text{ mm}^2$, $p=0.99$ vs pre-op, Power: 0.80; respectively). Experimental artery diastolic areas increased back to pre-op levels at day 4 but still had significantly reduced systolic areas ($0.13 \pm 0.04 \text{ mm}^2$, $p=0.32$ vs. pre-op, Power: 0.58; and $0.17 \pm 0.05 \text{ mm}^2$, $p<0.001$ vs pre-op; respectively). Figure 7-6 shows the changes in diastolic and systolic area over time throughout the Aim 3B experiments.

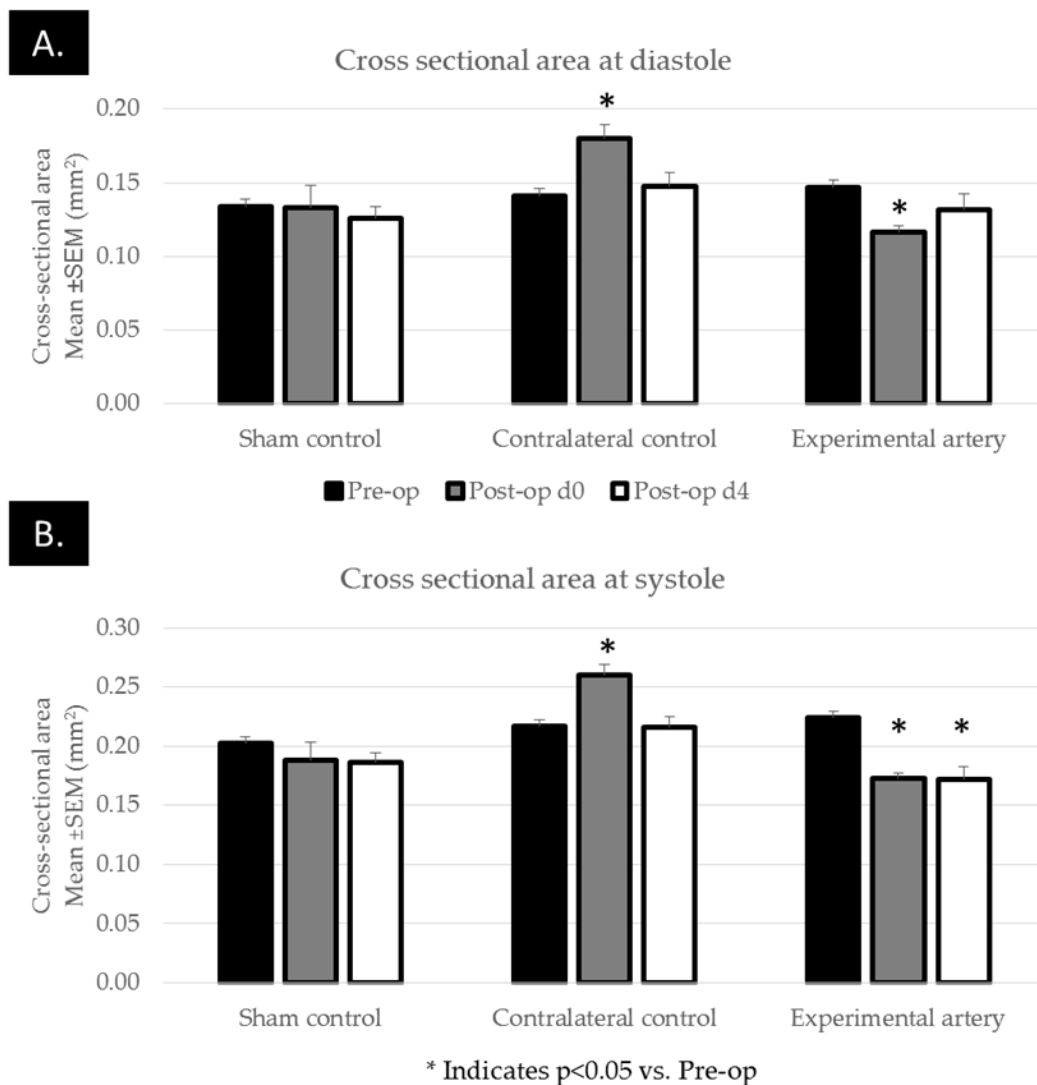


Figure 7-6: Changes in arterial cross-sectional area throughout the experiment A) Changes in diastolic cross-sectional area over time. B) Changes in systolic area over time. * indicates $p<0.05$; $n=10$ in sham group and $n=20$ in contralateral control and experimental group.

7.3.3 Histological analysis of intimal thickness

Masson's trichrome stain on day 4 tissues was used to assess the mean intimal thickness, and wall thickness for all vessels. Figure 7-7 shows representative images of vessels from each group with the manual tracing overlaid.

Intimal thickness at day 4 was consistent amongst the three groups with no statistical differences amongst the groups. Intimal thickness for sham, contralateral and experimental arteries were $2.5 \pm 0.3 \mu\text{m}$, $2.1 \pm 0.3 \mu\text{m}$ and $2.6 \pm 0.1 \mu\text{m}$ respectively ($p=0.12$; Power: 0.25). Intimal thicknesses are plotted in Figure 7-8A. Additionally, no significant differences in total wall thickness were observed between control and experimental arteries. Sham, contralateral and experimental arteries had total wall thicknesses of $53.9 \pm 3.5 \mu\text{m}$, $64.6 \pm 4.8 \mu\text{m}$ and $58.3 \pm 3.4 \mu\text{m}$ respectively ($p=0.69$; Power: 0.05; Figure 7-8B).

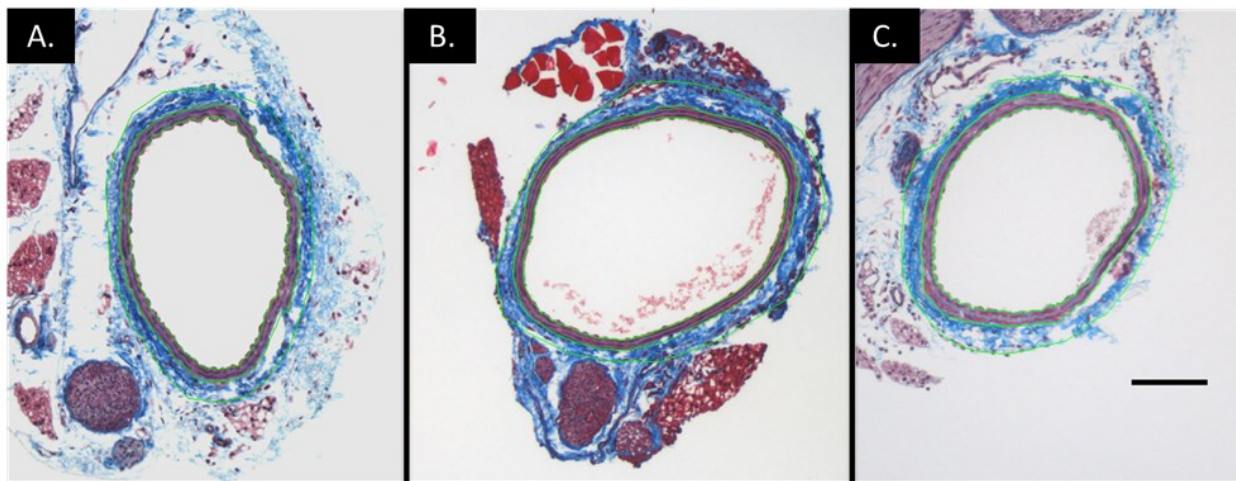


Figure 7-7: Use of Masson's Trichrome to find thickness of vessel layers. Representative sections are shown with overlaid green tracings of the two lamina and the outer extent of the vessel. Wall thickness values were computed using these tracings. A) Sham control, B) Contralateral control, C) Experimental LCCA. Scale bar: 100μm

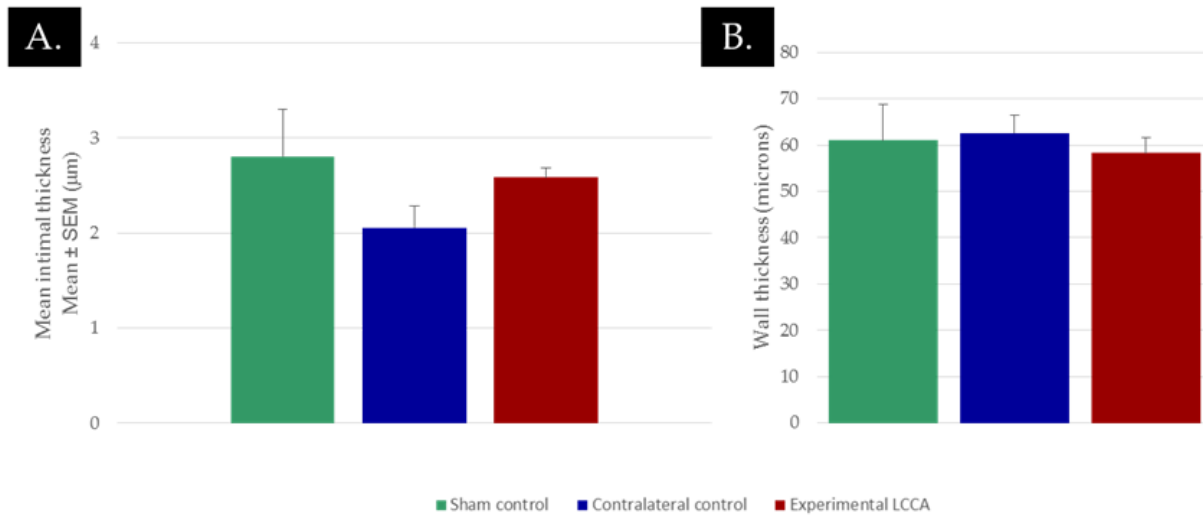


Figure 7-8: Intimal thickness and wall thickness at day 4. A) Intimal thickness at day 4. B) Wall thickness at day 4; n=5 in sham group and n=10 in contralateral control and experimental group.

7.3.4 Relationship between strain and diameter

Strain magnitudes were divided into high and low strains in two different ways. In Figure 7-9 A-C (left), strain was cut off based on the lowest observed control strain value (0.16, see dotted lines in Figure 7-5). A trend toward increased diastolic and systolic areas (Figure 7-9B, C) was observed between pre-op and post-op day 4. This trend was not present in the high strain group. Strain was also cut off at 0.1 (the cutoff used in Aim 3A of this work). The lower cutoff clearly exacerbated the increase in areas. Given that only 2 animals fell below the 0.1 cutoff, statistical measures were not employed on areas.

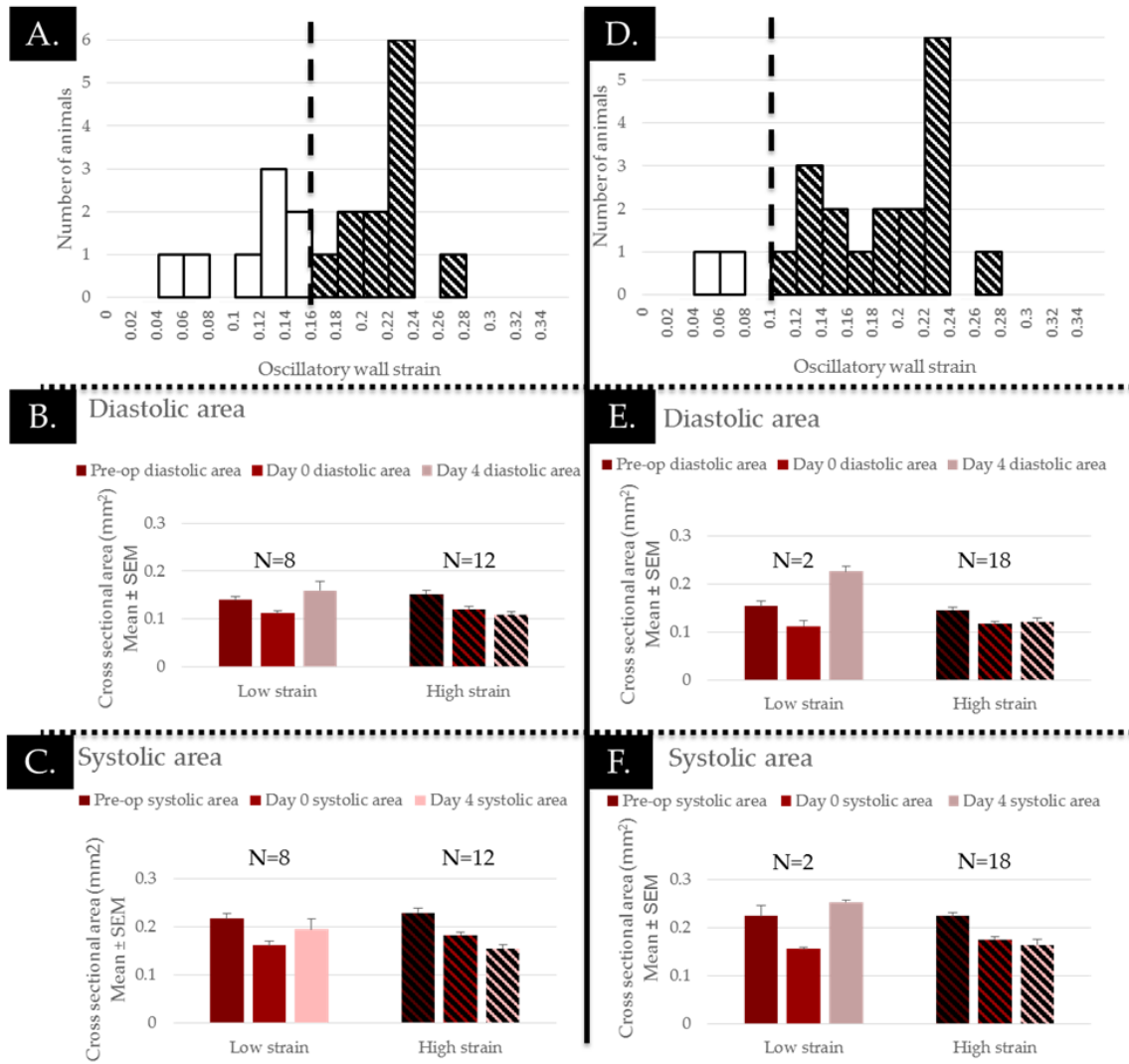


Figure 7-9: Differences in cross-sectional area between low and high strain groups. A) Histogram of day 4 strain values with strain cut off at 0.16 (minimum control value). B) Diastolic areas for low strains (<0.16) and high strains (>0.16). C) Systolic areas for low strains (<0.16) and high strains (>0.16). D) Histogram of day 4 strain values with strain cut off at 0.10 (value used in aim 3A). E) Diastolic areas for low strains (<0.1) and high strains (>0.1). F) Systolic areas for low strains (<0.1) and high strains (>0.1).

7.3.5 Immunohistochemical analysis

The medial layer of the vessel appeared normal at day 4, with consistent expression of myosin heavy chain throughout. Similarly, consistent expression of CD-31 was visible along the luminal surface suggesting that the endothelium was intact at day 4. Interestingly, cells expressing CD-45 were also observed at the luminal surface in 40% of experimental arteries

examined but not in control arteries. At some points, these cells appear to be disrupting the layer of CD-31 positive cells, while other regions demonstrate co-expression of CD-31 and CD-45. Based on IHC analysis of only 1-2 sections per artery, however, there does not appear to be a correlation between CD45 expression and low strain magnitude. Figure 7-10 shows a representative image of an experimental artery stained for expression of all three markers.

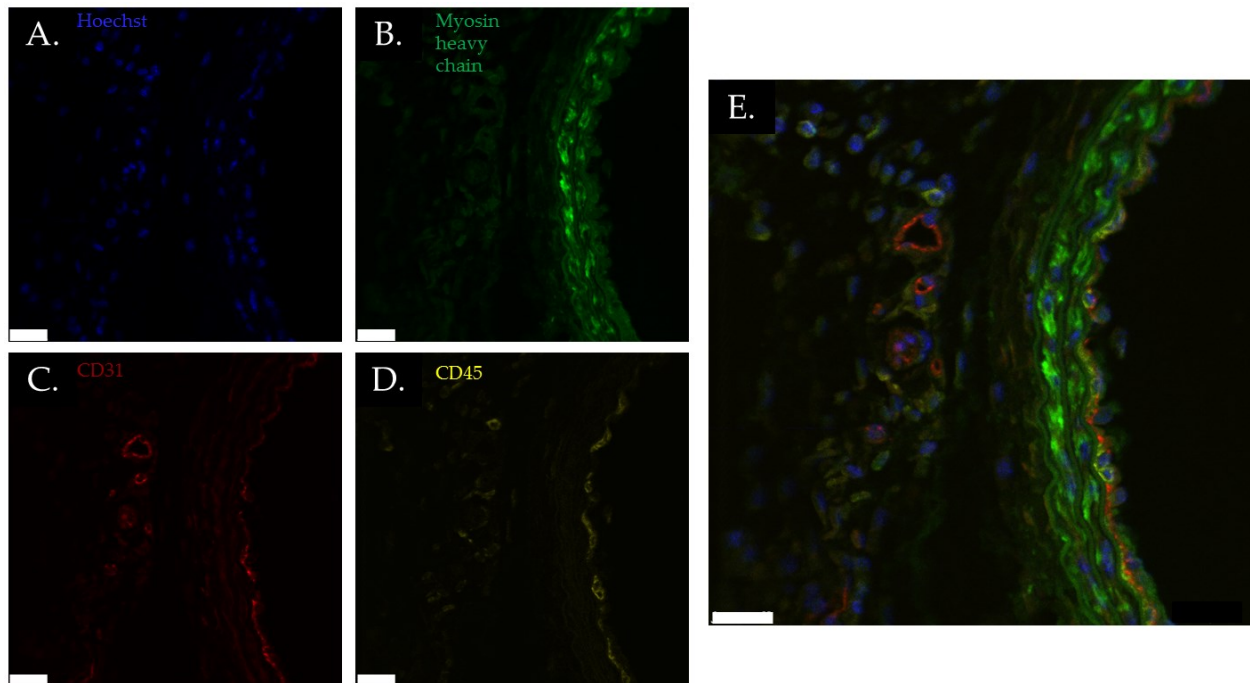


Figure 7-10: Myosin heavy chain, CD-31 and CD-45 expression. A) Hoechst dye indicating nuclei (blue), B) Myosin Heavy Chain indicating contractile smooth muscle cells (green), C) CD-31 a marker expressed by endothelial cells, D) CD-45, an antigen common to leukocytes. E) Merge of all images. All scale bars: 25 μ m.

In addition to cell types, expression of Ki-67, a marker of proliferating cells was assessed. Ki-67 expression was found in the vessel wall or on the luminal surface in 90% of animals assessed (n=10). Qualitative assessment of Ki-67 positive cells suggests that cells are recruited to both the lumen and adventitial layer of the vessel wall. Ki-67 positive cells were not found at the wall of any control sections.

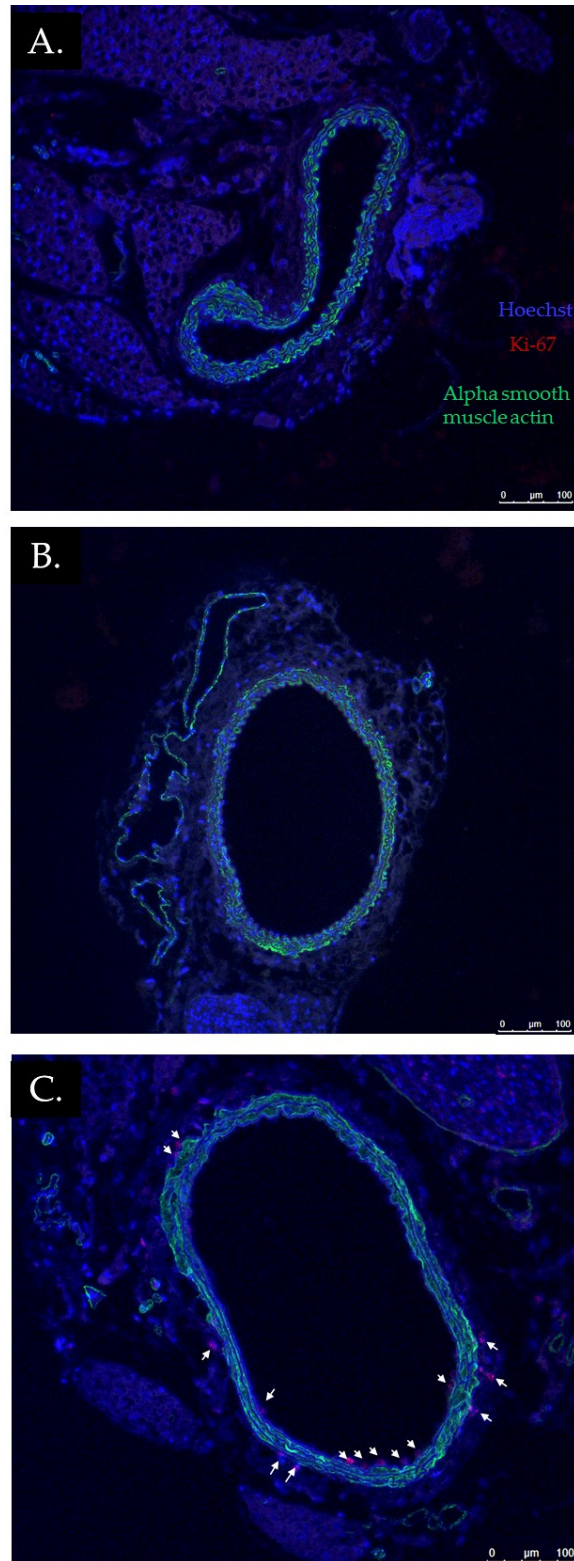


Figure 7-11: Ki-67 and α SMA expression in control and experimental arteries. A) Sham control artery, B) Contralateral control artery, C) Experimental artery. Immunofluorescence stain show nuclei in blue (Hoechst 33342), alpha smooth muscle actin in green, and ki-67 in red. White arrows indicate cells at the vessel wall expressing ki-67.

Finally, synthesis of the GAGs hyaluronic acid and versican was assessed. No versican synthesis was observed in arteries in any of the experimental groups. HA expression was seen in experimental animals but no obvious qualitative differences in expression levels were observed between control and experimental arteries (Figure 7-12).

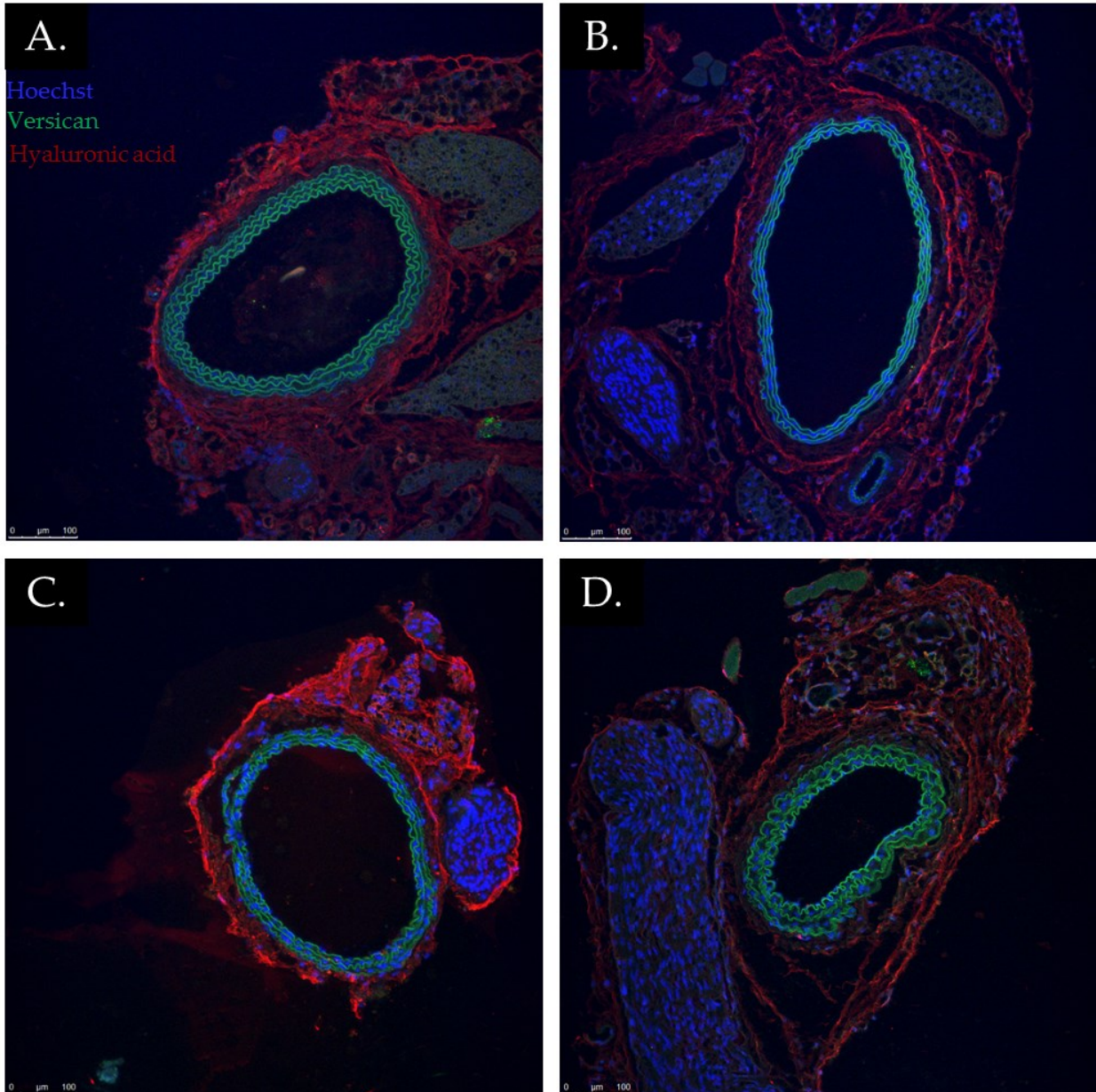


Figure 7-12: Hyaluronic acid and versican expression in control and experimental arteries. A) Baseline (no surgery) control artery. B) Sham control artery. C) Contralateral control artery. D) Experimental artery. Stain shows nuclei (Hoechst) in blue, versican in green and hyaluronic acid in red.

7.4 Discussion

In the earlier chapters of this dissertation, we demonstrated a promising relationship between early reductions in mechanical strain and the eventual formation of intimal hyperplasia. The major assumption made in those chapters, however, was that significant intimal hyperplasia had not formed by the day 4 timepoint. In this chapter, we both verify our assumption from previous chapters and enhance our understanding of early changes in the vessel wall at the cellular level.

In support of our findings in chapter 6, we observed a significant reduction in mechanical strain at day 4 compared to pre-op in our experimental group but no changes in the control groups. Interestingly, the reductions in strain observed in this study were not as severe as those seen in the chapter 6 study (with day 4 strains in this chapter of 0.18 ± 0.01 and the chapter 6 strains of 0.11 ± 0.02). We suspect that this difference between the two studies is likely due to biological variability and variability due to different surgeons performing the surgery. Another interesting difference between this study and the previous study is that changes in strain here appear to be due to decreases in systolic area rather than increases in diastolic area. Despite the minor differences between the day 4 outcomes between this study and the chapter 5 study, it remains clear that reductions in strain occur at day 4 in this model.

In addition to pre-op and day 4 data, we also assessed strains immediately after creating the stenosis. Reductions in oscillatory strain were not observed immediately after placement of the stenosis. This suggests that reductions in strain are not an immediate mechanical effect of focal stenosis creation, but rather a change in mechanical properties caused a biological reaction to focal stenosis creation.

Diastolic and systolic areas were also assessed using ultrasound. Data in Figure 7-6 demonstrates that, shortly after stenosis formation, the experimental cross-sectional area at both diastole and systole are decreased while the contralateral control areas are increased. By day 4, however, the contralateral control arteries return to their baseline levels while the experimental systolic area remains reduced. To better compare the data from this aim to the data in Aim 3A, area data was stratified using a strain cutoff. In Figure 7-9, strains were cut off using the lowest control artery strains at day 4, as well as the 0.1 cutoff used in Aim 3A. These data show a similar trend toward increase in diastolic area at day 4 to that found in Aim 3A. Additionally, systolic areas are seen to decrease in low strain groups at day 4. These data demonstrate the importance of assessing oscillatory wall strain at day 4. Although vessel diameters may vary from animal to animal and need to be assessed before IH formation. Strain, on the other hand, can provide evidence of changes in wall properties based on data from only one time point.

Intimal and wall thicknesses were assessed at day 4 to improve our understanding of the temporal progression of IH in this model. The data in this chapter support our assumption in previous chapters that IH has not formed at the day 4 timepoint in this model. No significant differences in wall thickness or intimal thickness were observed at day 4 amongst the three groups. We do, however, observe differences between control arteries and experimental arteries at the cellular level. Recruitment of leukocytes to the vascular wall appears to occur at or before the day 4 timepoint as well as some interruption in the expression of CD-31 at the arterial lumen; both hallmark signs of the beginnings of IH.^{14, 237} Additionally, staining for Ki-67 demonstrates some proliferating cells in the vicinity of the vessel wall.

The lack of significant IH at day 4 observed in this chapter, combined with the day 4 reductions in strain observed in chapter 5 and this chapter suggest an important mechanistic role for strain reduction in the formation of IH. Since we demonstrate that wall thickness increases have not occurred at day 4 and other research suggests that pressure reductions will not occur in the region proximal to the stenosis,²³⁵ the culmination of our data suggests that early changes in wall mechanical properties drive the reductions in strain we observed. By observing these changes the methods described herein have potential to help predict the formation of IH in this model.

8 Conclusions and Future Work

8.1 Conclusions

Coronary and peripheral artery diseases remain a major cause of morbidity and mortality in the United States.¹ Although the underlying causes of these diseases remain largely unknown, evidence suggests that a major initiating factor of these diseases is Intimal Hyperplasia (IH).^{3, 6-9} A number of researchers have correlated local differences in the mechanical environment with neointimal formation and arteriosclerosis.^{14, 19, 20} Despite the extensive evidence suggesting the role of shear stress in IH formation, others have demonstrated that shear based explanations alone fail to predict IH.^{27, 28} In this dissertation, we demonstrate that arteries form IH in response to changes in a different mechanical force, oscillatory wall strain. Herein, we hypothesized that reductions in oscillatory wall strain precede the formation of IH in our murine model of IH.

In order to test this hypothesis, we developed a novel method to noninvasively measure mechanical strains on the murine arterial wall. Although the murine model is attractive as a research tool, mouse studies are complicated by both the small vessel size and high heart rates seen in the murine model. To overcome these issues, we first adapted the combination of high frequency ultrasound with speckle tracking from the cardiac literature⁴⁰⁻⁴² for use in the measurement of oscillatory wall strains in the mouse artery.⁴⁴ In the first objective of Aim 1, we used an *in vitro* vascular phantom to show a correlation between ultrasound-based strains and a previously validated optics-based strain measurement system.^{181, 183} To test the *in vivo* measurement capabilities of our strain measurement approach, in objective 1B, we applied our approach to a mouse model of aortic aneurysms. In this *in vivo* study, we demonstrated the ability of our measurement approach to measure significant changes in aortic strains due to a vascular disease in the murine model.

The methods and data presented in this dissertation provide compelling evidence suggesting a correlation between early reductions in mechanical strain and the eventual formation of IH. The animal model discussed herein and developed by Tao *et al.*³⁷ is unique in that it does not directly injure or occlude any blood vessel unlike most other models.²³⁰⁻²³² Interestingly, we still reveal a similar intimal hyperplastic response to those studied previously.^{161, 230, 231} Given that both the original model study,³⁷ and subsequent study²³⁸ using this model both report that only a subpopulation of mice given a focal stenosis go on to form IH, we suspect that biological variation amongst the animals plays a role in clinical outcome at day 28. Herein we suggest that changes in the mechanical environment, particularly circumferential wall strain, play a key role in determining neointimal formation.

We found that reductions in strain at 27 days after focal stenosis occur in the regions of the carotid artery with the most hyperplasia, while those with higher strains had less neointima formation. Even though this phenomenon supports our hypothesis, the significant increase in wall thickness seen at day 28 likely played a role in causing strain reductions. From a mechanical standpoint, we expect that one of three changes will result in mechanical strain reduction. Increases in wall thickness directly increase the load bearing cross-sectional area over which wall forces are applied; our data in Aim 2 demonstrate that increased cross-sectional area has occurred at day 28. Decreases in luminal pulse pressure could also play a role in decreasing vascular strain. Since strains measured in this studied are measured proximal to the focal stenosis, we do not expect that there is any change in pressures in these animals. Finally, an increase in wall stiffness could cause a decrease in wall strain. At day 27, we expect this to be true as well due to the reported increase in collagen content in our model.³⁷ To assess whether

the strain reductions were caused by increased wall thickness or by other factors, we assessed strains and IH at earlier time points.

Herein, we probed the temporal changes in both IH and mechanical strain in the focal stenosis model. In Objective 3A, we re-examined histological data from Aim 2 and compared histological outcome at day 28 to strains at just 4 days after focal stenosis creation. The results of this objective demonstrated that the reductions in strain we saw at day 28 had already occurred at day 4 post-op. This finding suggests that the changes in strain may precede the formation of IH. The results of Objective 3A also revealed that, on a region by region basis, some regions had low strain at day 4 while others had higher strains (close to baseline). Further, we discovered that there was statistically lower IH formation at day 28 post-op in regions with high day 4 strains vs. regions with low day 4 strain.

The final piece of evidence needed to fully support the overall hypothesis of this dissertation was to show that IH does not form by day 4 post-op. In objective 3B we examined both neointimal formation at post-op day 4 and the changes in strain found immediately post-op. Our quantification of intimal and wall thickness at day 4 post-op demonstrated no significant changes in gross wall morphology at day 4. These data suggest that the reductions in strain both precede IH in this model and are not due solely to increases in wall thickness. Additionally, post-op day 0 data (Objective 3B) demonstrated that no immediate decrease in strain occurs after focal stenosis creation. This evidence suggests that changes in wall morphology between post-op day 0 and day 4 results in the strain reductions we find in this model.

Previous models of IH in the mouse model have identified that cellular proliferation and inflammatory cell recruitment to the region are the events that initiate eventual intimal hyperplasia.^{14, 237} In this study, we find that, similar to other studies, leukocytes (CD45+ cells) are recruited to the endothelial wall by day 4. This suggests that the beginning of an inflammatory response is occurring. One group has demonstrated that a circulating cell type, the fibrocyte, which is known to express cd45 is recruited to the vascular wall at the onset of intimal hyperplasia.²³⁹ Additionally, Varcoe *et al.* identified that these fibrocytes also expressed cd31 when recruited to the vascular wall, a phenomenon we observed in Aim 3B.²⁴⁰ Similarly, we observed cells in the vascular wall that co-expressed CD31 and CD45.

To support our cellular findings, we also examined ki-67 expression to probe proliferation at the vessel wall. Our findings demonstrate that the majority of experimental arteries at day 4 contain cells that express Ki-67, a marker of proliferating cells. This finding is significant because cellular proliferation is considered a hallmark of intimal hyperplastic responses.^{14, 86} In addition to cellular recruitment, we assessed expression of GAGs in the vascular wall at day 4. Looking at both versican and hyaluronic acid (HA) expression, we observed no obvious differences in the expression of either GAG at day 4. Chajara *et al.* previously demonstrated that rat aortas express HA in the neointima 14 days after balloon injury as well as expression in the adventitia at baseline.²²⁹ Given that our day 4 histology was completed prior to neointima formation, we did not see HA synthesis at the wall. Versican expression was also assessed. At day 4, we did not observe versican expression in any experimental or control arteries. This suggests that versican expression does not occur in this model or that it occurs downstream of strain reduction.

The clinical relevance of this model differs from that of previous models in that it does not focus on deliberate endothelial injury as the underlying cause of IH. Many previous studies focus on the effects of either balloon angioplasty or wire injury (or denudation) of the endothelium on subsequent IH.^{14, 108, 237} Interestingly, we and others have found that IH forms without causing any apparent injury to the endothelium. As a result, the relevance of both this model³⁷ and the subsequent work in this dissertation is mainly to the underlying mechanisms of IH, without endothelial injury. Based on the data at hand, we suspect that reductions in luminal flow lead to structural changes in the vessel wall between the focal stenosis creation and day 4 post-op. These changes result in oscillatory strain reduction and eventually lead to leukocyte infiltration, cellular proliferation and intimal hyperplasia.

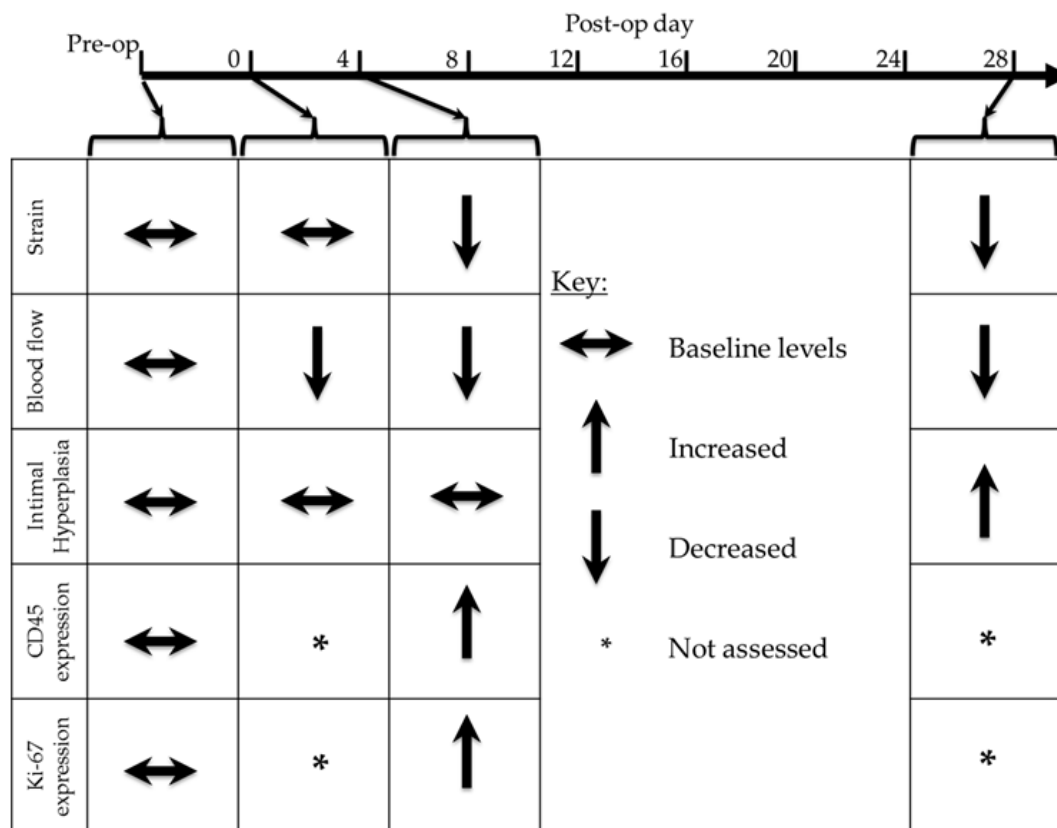


Figure 8-1: Summary of the results of this dissertation.

8.2 Limitations

The experiments in this dissertation are limited by a number of factors. First and foremost, the present study did not directly decouple the effects of other mechanical forces on the wall from mechanical strain. Namely, we did not compute wall tensile stress or wall shear stress in these studies. In order to assess wall stress, it would have been necessary to measure luminal pressures in the carotids during the study. Unfortunately, given the relatively large size of the smallest commercially available pressure catheters (0.9 French size/300 μm) compared to the inner diameter of the mouse carotid artery (300-400 μm),^{37, 225} insertion of a pressure catheter would likely impede or change blood flow in the artery. Despite this limitation, others have assessed systemic pressure changes in similar flow reduction models and have not observed significant pressure changes in the proximal region.²³⁵ Blood flow through the stenosed blood vessel was also not assessed. In the published study describing the focal stenosis model, an average of 85% reduction in blood flow was reported immediately after stenosis.³⁷ We have not, however, determined if a correlation exists between different levels of blood flow and resultant IH in this model. Given that all of the comparisons made in this study are between animals of the same age and strain, with focal stenoses made by the same lab team, it is not likely that measurable differences in blood flow through the arteries would be observed.

The results in Objective 1A demonstrated a large difference between strains measured via ultrasound at the tubing lumen and strains measured via HDM at the tubing outer wall. Theoretical analysis of these relations assuming constant tubing wall volume demonstrated this difference in strains was largely due to the thickness of the tubing. Although others have used

thin wall assumptions to simplify modelling of carotid arteries²⁴¹ our results suggest that some arteries must be considered as thick walled vessels depending on the ratio of vessel wall thickness to radius. In our silicone tubing vessel analog, the ratio of wall thickness to outer radius was 0.25 while sham arteries at day 4 had a ratio of only 0.13 ± 0.02 (by histology). This much smaller ratio would likely allow for accurate determination of wall strains using thin wall assumptions. In our day 28 arteries, however, the ratio of wall thickness to wall radius averaged 0.46 ± 0.13 . In the case of day 28 arteries, thick wall assumptions should apply. Future studies should carefully consider the wall thickness of arteries with IH to determine if thin wall assumptions apply. Despite this limitation in approach, we expect the luminal surface of the vessel, the region where we measured strain with ultrasound, to have the highest wall stress and strain. ²⁴²Limitations to our strain measurement methodologies are also recognized. Only 1 dimensional strain was assessed in this study. Given the lack of contrast between the outer wall of the carotid artery and the surrounding tissue, we were only able to measure luminal strains in the circumferential direction and longitudinal strains were not assessed. Given that the circumferential strain is known to be the most prominent strain on the vessel wall, it is likely that the greatest changes in strains will be observed in the circumferential direction. Finally, our ultrasound approach is limited by our ability to orient the probe perpendicular to the artery in 3 dimensions. Variations in probe angle can lead to smaller or larger diameter measurements using ultrasound, which may increase animal to animal variability in diameter measurements. Since we measure oscillatory strains based on systolic and diastole without changing probe angles, we do not suspect this variation significantly affected strain our measurements.

8.3 Future work

In this dissertation, we developed a novel method of measuring murine arterial strains noninvasively and demonstrate a promising correlation between oscillatory strain reduction and IH formation in this model. We identified that changes in wall tensile stress and wall shear stress may also play a role in IH formation in this model. Consequently, it will be important in future studies to directly assess these mechanical factors and determine their relation to IH outcome in this model. As a result of these limitations, a crucial future step would be to measure pressure simultaneously with strain measurements. Since we believe that insertion of a pressure catheter into the carotid would result in extreme changes in local hemodynamics, simultaneous systemic pressure recordings should be used (in either the aorta or femoral artery) to estimate carotid pressure. Additionally, future studies should use either pulsed wave Doppler ultrasonography or a flow probe to measure flow through the carotid artery.

In the results of this dissertation we identified that changes in mechanical strain, particularly those driven by increased diastolic area, lead to IH formation. This finding suggests that compositional changes in the arterial wall are causing changes in its mechanical properties. The major component of the arterial wall that contributes to its ability to distend under pressure is elastin.²⁴³ The mechanical results presented herein suggest that, assuming luminal pressure does not change significantly, the stiffness of the artery may be increasing in the first few days after creation of the focal stenosis. Interestingly, *in vitro* research into abdominal aortic aneurysms has demonstrated that elastin degradation assays result in increased vascular stiffness and increased vessel diameters.²²⁸ This similarity between *in vitro* elastin degradation and our *in vivo* results suggests a mechanism that may drive strain changes in our model.

Future studies should look in greater detail into the structural changes in elastin in our model of IH. Others have accomplished this using multi-photon microscopy and have demonstrated that fibers can be extracted and angles can be quantified.²⁴⁴ Application of such a tool to our model could allow for direct comparison of elastin structural changes to reductions in mechanical strain. In collaboration with Yanhang Zhang, Ph.D. at Boston University, we have begun to analyze the elastin and collagen structure of blood vessels from our murine model using two-photon microscopy (Figure 8-2). The results of these preliminary analyses demonstrate that elastin structure at the vessel's medial surface appears to be less organized at day 4 in experimental animals compared to baseline arteries. Others have demonstrated that inhibition of matrix metalloproteinases (MMPs) prevents elastin breakdown and minimizes IH in arteriovenous grafts.²⁴⁵ This evidence suggests that release of MMPs from leukocytes recruited to the vessel wall may result in the elastin breakdown observed by the Zhang lab; which could produce the strain reductions presented in this dissertation. Future studies should focus on quantifying the elastin organization and orientation using two-photon microscopy images.

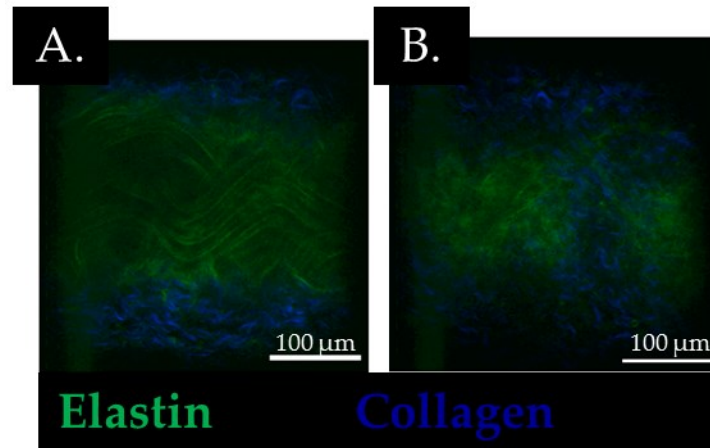


Figure 8-2: Two-photon microscopy analysis of medial elastin and collagen View of the internal surface of a murine artery showing collagen and elastin structure. A) Baseline artery demonstrating wavy, structured elastin structure and B) Day 4 experimental artery showing less structured elastin interrupted by collagen. Tissue processing and image acquisition courtesy of Ming-Jay Chow, Raphael Turcotte and Yanhang Zhang Ph.D. from Boston University

In addition to assessment of elastin structure, the mechanisms behind IH in this model could be better understood by determining the point at which IH cannot be reversed. Given that our results suggest that creating a focal stenosis leads to structural changes and mechanical strain reductions and leads to IH, it may be important to understand if removal of the suture at day 4 would return the artery to its initial strain levels and if removal of the suture would prevent formation of IH at day 28.

Another major finding in this dissertation is the presence of leukocytes and proliferating cells at the vessel wall as early as day 4. Since the immunohistochemical analyses presented herein are decidedly preliminary, it will be necessary for future studies to analyze the cellular activity in greater detail. In particular, regional differences in leukocyte recruitment (differences along the length of the vessel) should be assessed. Additionally, leukocytes and proliferating cells should be counted in each region of the vessel and correlated with oscillatory wall strain levels. This can be accomplished by counting nuclei that either co-express Ki67 or which are

surrounded by CD45 staining. Future work should also aim to assess the specific cell types seen proliferating at the wall and the specific type of leukocytes seen at the wall (i.e. markers that identify macrophages such as CD68).

Further, this dissertation could provide the groundwork for future therapies for treating IH. The data herein suggest that mechanical strain reductions play a role in IH formation. Given the elastin degradation observed by the Zhang lab using two-photon imaging, an important first therapeutic step would likely be to increase the cyclic stretch on the vessel wall by either increasing elastin content in the vascular wall or providing mechanical support to the vessel via some other means, such as an external cuff. A number of previous studies have demonstrated that external reinforcement of vein grafts can reduce intimal hyperplasia and medial thickening.²⁴⁶⁻²⁴⁹ The data presented herein suggest that by adding external support to arteries may reduce IH as well. Additionally, our data suggest that the compliance of the external supporting the vessel may be important. By changing the mechanical stretch applied to the vessel wall, our data suggest that IH formation could be reduced.

Finally, the results of this study could provide the foundation for future clinical applications. Ultrasound imaging is commonly used in the clinical setting to assess patients with vascular diseases. The approach described herein could be used on top of existing clinical US scans to provide noninvasive measurements of arterial wall strains. The ability to determine the structural properties of arteries based on noninvasive strain measurements could be applied as a first level determination of susceptibility to IH and the vascular diseases that result from it. Vessels with inherently low strain could have altered mechanical properties that make them prone to failure. In the work described herein, we demonstrate that strains below around 10 -

14% in the murine model may cause susceptibility to IH. If a similar strain threshold level could be determined in human arteries, this parameter could provide additional data to physicians and aid in determination of the appropriate vascular intervention. If this correlation exists in human arteries, it may allow for more efficient prediction of arterial susceptibility to occlusion. For example, patients with low oscillatory wall strain will likely need an intervention to overcome the rapid progression of IH. Patients with high oscillatory wall strain may not need an immediate intervention. The relationships demonstrated in this dissertation could be used to improve the diagnosis of vascular disease.

Works Cited

1. Go AS, Mozaffarian D, Roger VL, Benjamin EJ, Berry JD, Borden WB, Bravata DM, Dai S, Ford ES, Fox CS, Franco S, Fullerton HJ, Gillespie C, Hailpern SM, Heit JA, Howard VJ, Huffman MD, Kissela BM, Kittner SJ, Lackland DT, Lichtman JH, Lisabeth LD, Magid D, Marcus GM, Marelli A, Matchar DB, McGuire DK, Mohler ER, Moy CS, Mussolino ME, Nichol G, Paynter NP, Schreiner PJ, Sorlie PD, Stein J, Turan TN, Virani SS, Wong ND, Woo D, Turner MB, American Heart Association Statistics C, Stroke Statistics S. Heart disease and stroke statistics--2013 update: A report from the american heart association. *Circulation*. 2013;127:e6-e245
2. Conte MS. Technical factors in lower-extremity vein bypass surgery: How can we improve outcomes? *Semin Vasc Surg*. 2009;22:227-233
3. Subbotin VM. Analysis of arterial intimal hyperplasia: Review and hypothesis. *Theor Biol Med Model*. 2007;4:41
4. Teirstein PS, Massullo V, Jani S, Popma JJ, Russo RJ, Schatz RA, Guarneri EM, Steuterman S, Sirkin K, Cloutier DA, Leon MB, Tripuraneni P. Three-year clinical and angiographic follow-up after intracoronary radiation : Results of a randomized clinical trial. *Circulation*. 2000;101:360-365
5. Monahan TS, Owens CD. Risk factors for lower-extremity vein graft failure. *Semin Vasc Surg*. 2009;22:216-226
6. Yutani C, Imakita M, Ishibashi-Ueda H, Tsukamoto Y, Nishida N, Ikeda Y. Coronary atherosclerosis and interventions: Pathological sequences and restenosis. *Pathology international*. 1999;49:273-290
7. Miyao Y, Kugiyama K, Kawano H, Motoyama T, Ogawa H, Yoshimura M, Sakamoto T, Yasue H. Diffuse intimal thickening of coronary arteries in patients with coronary spastic angina. *Journal of the American College of Cardiology*. 2000;36:432-437
8. Luo H, Nishioka T, Eigler NL, Forrester JS, Fishbein MC, Berglund H, Siegel RJ. Coronary artery restenosis after balloon angioplasty in humans is associated with circumferential coronary constriction. *Arteriosclerosis, thrombosis, and vascular biology*. 1996;16:1393-1398
9. Kipshidze N, Dangas G, Tsapenko M, Moses J, Leon MB, Kutryk M, Serruys P. Role of the endothelium in modulating neointimal formation: Vasculoprotective approaches to attenuate restenosis after percutaneous coronary interventions. *Journal of the American College of Cardiology*. 2004;44:733-739
10. Hung M-J, Cherng W-J, Yang N-I, Cheng C-W, Li L-F. Relation of high-sensitivity c-reactive protein level with coronary vasospastic angina pectoris in patients without hemodynamically significant coronary artery disease. *The American journal of cardiology*. 2005;96:1484-1490
11. Cin VG, Pekdemir H, Camsar A, Çiçek D, Akkus MN, Parmaksız T, Katırcıbaşı T, Döven O. Diffuse intimal thickening of coronary arteries in slow coronary flow. *Japanese heart journal*. 2003;44:907-919
12. Stary HC, Chandler AB, Dinsmore RE, Fuster V, Glagov S, Insull W, Jr., Rosenfeld ME, Schwartz CJ, Wagner WD, Wissler RW. A definition of advanced types of atherosclerotic lesions and a histological classification of atherosclerosis. A report from the committee on vascular lesions of the council on arteriosclerosis, american heart association. *Circulation*. 1995;92:1355-1374
13. Glagov S. Intimal hyperplasia, vascular modeling, and the restenosis problem. *Circulation*. 1994;89:2888-2891
14. Newby AC, Zaltsman AB. Molecular mechanisms in intimal hyperplasia. *J. Pathol*. 2000;190:300-309
15. Geng YJ, Libby P. Evidence for apoptosis in advanced human atheroma. Colocalization with interleukin-1 beta-converting enzyme [see comments]. *Am.J.Pathol*. 1995;147:251-266

16. Schwartz SM, Campbell GR, Campbell JH. Replication of smooth muscle cells in vascular disease. *Circulation Research*. 1986;58:427-444
17. O'Brien ER, Alpers CE, Stewart DK, Ferguson M, Tran N, Gordon D, Benditt EP, Hinohara T, Simpson JB, Schwartz SM. Proliferation in primary and restenotic coronary atherectomy tissue. Implications for antiproliferative therapy. *Circulation Research*. 1993;73:223-231
18. Bjorkerud S. Short communication lesions , especially in inflammatory cells. 1996;149:367-380
19. Holmes DR, Jr., Savage M, LaBlanche JM, Grip L, Serruys PW, Fitzgerald P, Fischman D, Goldberg S, Brinker JA, Zeiher AM, Shapiro LM, Willerson J, Davis BR, Ferguson JJ, Popma J, King SB, 3rd, Lincoff AM, Tcheng JE, Chan R, Granett JR, Poland M. Results of prevention of restenosis with tranilast and its outcomes (presto) trial. *Circulation*. 2002;106:1243-1250
20. Fu K, Corbley MJ, Sun L, Friedman JE, Shan F, Papadatos JL, Costa D, Lutterodt F, Sweigard H, Bowes S, Choi M, Boriack-Sjodin PA, Arduini RM, Sun D, Newman MN, Zhang X, Mead JN, Chuaqui CE, Cheung HK, Zhang X, Cornebise M, Carter MB, Josiah S, Singh J, Lee WC, Gill A, Ling LE. Sm16, an orally active tgf-beta type i receptor inhibitor prevents myofibroblast induction and vascular fibrosis in the rat carotid injury model. *Arteriosclerosis, thrombosis, and vascular biology*. 2008;28:665-671
21. Newby AC. Matrix metalloproteinase inhibition therapy for vascular diseases. *Vascul Pharmacol*. 2012;56:232-244
22. Kuzuya M, Kanda S, Sasaki T, Tamaya-Mori N, Cheng XW, Itoh T, Itohara S, Iguchi A. Deficiency of gelatinase a suppresses smooth muscle cell invasion and development of experimental intimal hyperplasia. *Circulation*. 2003;108:1375-1381
23. Ku DN, Giddens DP, Zarins CK, Glagov S. Pulsatile flow and atherosclerosis in the human carotid bifurcation. Positive correlation between plaque location and low oscillating shear stress. *Arteriosclerosis*. 1985;5:293-302
24. Cho A, Reidy MA. Matrix metalloproteinase-9 is necessary for the regulation of smooth muscle cell replication and migration after arterial injury. *Circ Res*. 2002;91:845-851
25. Wentzel JJ, Krams R, Schuurbijs JC, Oomen JA, Kloet J, Der Giessen WJ, Serruys PW, Slager CJ. Relationship between neointimal thickness and shear stress after wallstent implantation in human coronary arteries. *Circulation*. 2001;103:1740-1745
26. Richter Y, Groothuis A, Seifert P, Edelman ER. Dynamic flow alterations dictate leukocyte adhesion and response to endovascular interventions. *J.Clin.Invest*. 2004;113:1607-1614
27. Ryer EJ, Hom RP, Sakakibara K, Nakayama KI, Nakayama K, Faries PL, Liu B, Kent KC. Pkcdelta is necessary for smad3 expression and transforming growth factor beta-induced fibronectin synthesis in vascular smooth muscle cells. *Arteriosclerosis, thrombosis, and vascular biology*. 2006;26:780-786
28. Lemson MS, Tordoir JH, Daemen MJ, Kitslaar PJ. Intimal hyperplasia in vascular grafts. *Eur J Vasc Endovasc Surg*. 2000;19:336-350
29. Abdel Aziz MT, Atta HM, Mahfouz S, Fouad HH, Roshdy NK, Ahmed HH, Rashed La, Sabry D, Hassouna aa, Hasan NM. Therapeutic potential of bone marrow-derived mesenchymal stem cells on experimental liver fibrosis. *Clinical biochemistry*. 2007;40:893-899
30. Aggarwal S, Pittenger MF. Human mesenchymal stem cells modulate allogeneic immune cell responses. *Blood*. 2005;105:1815-1822
31. Zwolak RM, Adams MC, Clowes AW. Kinetics of vein graft hyperplasia - association with tangential stress. *Journal of vascular surgery*. 1987;5:126-136
32. Wolinsky H, Glagov S. A lamellar unit of aortic medial structure and function in mammals. *Circ Res*. 1967;20:99-111

33. Lu X, Zhao JB, Wang GR, Gregersen H, Kassab GS. Remodeling of the zero-stress state of femoral arteries in response to flow overload. *American journal of physiology. Heart and circulatory physiology*. 2001;280:H1547-1559
34. Herold V, Wellen J, Ziener CH, Weber T, Peter K-hH, Eberhard N, Axel R, Bauer WR, Jakob PM, Sarkar SK. In vivo comparison of atherosclerotic plaque progression with vessel wall strain and blood flow velocity in apoe – / – mice with mr microscopy at 17 . 6 t. *Magnetic Resonance Materials In Physics Biology And Medicine*. 2009;22:159-166
35. Goergen CJ, Barr KN, Huynh DT, Eastham-Anderson JR, Choi G, Hedehus M, Dalman RL, Connolly AJ, Taylor CA, Tsao PS, Greve JM. In vivo quantification of murine aortic cyclic strain, motion, and curvature: Implications for abdominal aortic aneurysm growth. *Journal of magnetic resonance imaging : JMRI*. 2010;32:847-858
36. Danpinid A, Luo J, Vappou J, Terdtoon P, Konofagou EE. In vivo characterization of the aortic wall stress – strain relationship. *Ultrasonics*. 2010;50:654-665
37. Tao M, Mauro CR, Yu P, Favreau JT, Nguyen B, Gaudette GR, Ozaki CK. A simplified murine intimal hyperplasia model founded on a focal carotid stenosis. *Am J Pathol*. 2013;182:277-287
38. Barisione C, Charnigo R, Howatt DA, Moorlegghen JJ, Rateri DL, Daugherty A. Rapid dilation of the abdominal aorta during infusion of angiotensin ii detected by noninvasive high-frequency ultrasonography. *Journal of vascular surgery*. 2006;44:372-376
39. Martin-McNulty B, Vincelette J, Vergona R, Sullivan ME, Wang YX. Noninvasive measurement of abdominal aortic aneurysms in intact mice by a high-frequency ultrasound imaging system. *Ultrasound Med Biol*. 2005;31:745-749
40. Bauer M, Cheng S, Jain M, Ngoy S, Theodoropoulos C, Trujillo A, Lin FC, Liao R. Echocardiographic speckle-tracking based strain imaging for rapid cardiovascular phenotyping in mice. *Circ Res*. 2011;108:908-916
41. Mondillo S, Galderisi M, Mele D, Cameli M, Lomoriello VS, Zaca V, Ballo P, D'Andrea A, Muraru D, Losi M, Agricola E, D'Errico A, Buralli S, Sciomer S, Nistri S, Badano L. Speckle-tracking echocardiography: A new technique for assessing myocardial function. *J Ultrasound Med*. 2011;30:71-83
42. Dandel M, Hetzer R. Echocardiographic strain and strain rate imaging--clinical applications. *Int J Cardiol*. 2009;132:11-24
43. Leung DY, Ng AC. Emerging clinical role of strain imaging in echocardiography. *Heart Lung Circ*. 2010;19:161-174
44. Favreau JT, Nguyen BT, Gao I, Yu P, Tao M, Schneiderman J, Gaudette GR, Ozaki CK. Murine ultrasound imaging for circumferential strain analyses in the angiotensin ii abdominal aortic aneurysm model. *Journal of vascular surgery*. 2012;56:462-469
45. Marieb EN, Hoehn K. *Human anatomy and physiology*. San Francisco: Benjamin Cummings; 2007.
46. Wagenseil JE, Mecham RP. Vascular extracellular matrix and arterial mechanics. *Physiological Reviews*. 2009;89:957-989
47. Burton AC. Relation of structure to function of the tissues of the wall of blood vessels. *Physiol Rev*. 1954;34:619-642
48. Dingemans KP, Teeling P, Lagendijk JH, Becker AE. Extracellular matrix of the human aortic media: An ultrastructural histochemical and immunohistochemical study of the adult aortic media. *Anat Rec*. 2000;258:1-14
49. Clark JM, Glagov S. Transmural organization of the arterial media. The lamellar unit revisited. *Arteriosclerosis*. 1985;5:19-34
50. Leung DY, Glagov S, Mathews MB. Elastin and collagen accumulation in rabbit ascending aorta and pulmonary trunk during postnatal growth. Correlation of cellular synthetic response with medial tension. *Circ Res*. 1977;41:316-323

51. Berry CL, Greenwald SE, Rivett JF. Static mechanical properties of the developing and mature rat aorta. *Cardiovascular research*. 1975;9:669-678
52. Miller H, Poon S, Hibbert B, Rayner K, Chen YX, O'Brien ER. Modulation of estrogen signaling by the novel interaction of heat shock protein 27, a biomarker for atherosclerosis, and estrogen receptor beta: Mechanistic insight into the vascular effects of estrogens. *Arteriosclerosis, thrombosis, and vascular biology*. 2005;25:e10-14
53. Garvin MR, Labinaz M, Pels K, Walley VM, Mizgala HF, O'Brien ER. Arterial expression of the plasminogen activator system early after cardiac transplantation. *Cardiovascular research*. 1997;35:241-249
54. O'Brien ER, Bennett KL, Garvin MR, Zderic TW, Hinohara T, Simpson JB, Kimura T, Nobuyoshi M, Mizgala H, Purchio A, Schwartz SM. Beta ig-h3, a transforming growth factor-beta-inducible gene, is overexpressed in atherosclerotic and restenotic human vascular lesions. *Arteriosclerosis, thrombosis, and vascular biology*. 1996;16:576-584
55. Kural MH, Cai M, Tang D, Gwyther T, Zheng J, Billiar KL. Planar biaxial characterization of diseased human coronary and carotid arteries for computational modeling. *Journal of biomechanics*. 2012;45:790-798
56. Eberth JF, Cardamone L, Humphrey JD. Evolving biaxial mechanical properties of mouse carotid arteries in hypertension. *Journal of biomechanics*. 2011;44:2532-2537
57. John LCH. Biomechanics of coronary artery and bypass graft disease: Potential new approaches. *The Annals of thoracic surgery*. 2009;87:331-338
58. Chen C, Korshunov VA, Massett MP, Yan C, Berk BC. Impaired vasorelaxation in inbred mice is associated with alterations in both nitric oxide and super oxide pathways. *J Vasc Res*. 2007;44:504-512
59. Chatzizisis YS, Coskun AU, Jonas M, Edelman ER, Feldman CL, Stone PH. Role of endothelial shear stress in the natural history of coronary atherosclerosis and vascular remodeling: Molecular, cellular, and vascular behavior. *Journal of the American College of Cardiology*. 2007;49:2379-2393
60. Tanner FC, Largiadier T, Greutert H, Yang Z, Luscher TF. Nitric oxide synthase gene transfer inhibits biological features of bypass graft disease in the human saphenous vein. *J Thorac.Cardiovasc.Surg*. 2004;127:20-26
61. Passerini AG, Milsted A, Rittgers SE. Shear stress magnitude and directionality modulate growth factor gene expression in preconditioned vascular endothelial cells. *Journal of vascular surgery*. 2003;37:182-190
62. Berceli SA, Jiang Z, Blalock TD, Pfahnl CL, Schultz GS, Ozaki CK. Shear stress regulates connective tissue growth factor (ctgf) in vein graft remodeling. *J Surg Res*. 2003;114:241
63. Berceli SA, Jiang Z, Klingman NV, Pfahnl CL, Abouhamze ZS, Frase CD, Schultz GS, Ozaki CK. Differential expression and activity of matrix metalloproteinases during flow-modulated vein graft remodeling. *J Vasc.Surg*. 2004;39:1084-1090
64. Jiang Z, Berceli SA, Pfahnl CL, Wu L, Goldman D, Tao M, Kagayama M, Matsukawa A, Ozaki CK. Wall shear modulation of cytokines in early vein grafts. *Journal of vascular surgery*. 2004;40:345-350
65. Jiang Z, Shukla A, Miller BL, Espino DR, Tao M, Berceli SA, Ozaki CK. Tumor necrosis factor-alpha and the early vein graft. *J Vasc Surg*. 2007;45:169-176
66. Jiang Z, Wu L, Miller BL, Goldman DR, Fernandez CM, Abouhamze ZS, Ozaki CK, Berceli SA. A novel vein graft model: Adaptation to differential flow environments. *American journal of physiology. Heart and circulatory physiology*. 2004;286:H240-245
67. Ozaki CK, Jiang Z, Berceli SA. Tnf-alpha and shear stress-induced large artery adaptations. *J Surg Res*. 2007;141:299-305

68. Ozaki CK, Jiang Z, Berceci SA. Tnf- α and shear stress induced large artery adaptations. *Journal of Surgery Research*. 2007;141:299-305
69. Joshi AK, Leask RL, Myers JG, Ojha M, Butany J, Ethier CR. Intimal thickness is not associated with wall shear stress patterns in the human right coronary artery. *Arteriosclerosis, thrombosis, and vascular biology*. 2004;24:2408-2413
70. Evju O, Valen-Sendstad K, Mardal KA. A study of wall shear stress in 12 aneurysms with respect to different viscosity models and flow conditions. *Journal of biomechanics*. 2013
71. Lehoux S, Castier Y, Tedgui A. Molecular mechanisms of the vascular responses to haemodynamic forces. *J Intern.Med*. 2006;259:381-392
72. Bassiouny HS, White S, Glagov S, Choi E, Giddens DP, Zarins CK. Anastomotic intimal hyperplasia: Mechanical injury or flow induced. *Journal of vascular surgery*. 1992;15:708-716
73. Schwartz LB, O'Donohoe MK, Purut CM, Mikat EM, Hagen PO, McCann RL. Myointimal thickening in experimental vein grafts is dependent on wall tension. *J. Vasc. Surg*. 1992;15:176-186
74. Glagov S, Bassiouny HS, Sakaguchi Y, Goudet CA, Vito RP. Mechanical determinants of plaque modeling, remodeling and disruption. *Atherosclerosis*. 1997;131 S13-S14
75. Fung YC. *A first course in continuum mechanics*. Englewood Cliffs, NJ: Prentice Hall; 1993.
76. Boekhoven RW, Rutten MCM, van Sambeek MR, van de Vosse FN, Lopata RGP. Echo-computed tomography strain imaging of healthy and diseased carotid specimens. *Ultrasound Med Biol*. 2014
77. Morrison T, Choi G, Zarins C. Circumferential and longitudinal cyclic strain of the human thoracic aorta: Age-related changes. *Journal of vascular surgery*. 2009;49:1029-1036
78. Fung Y-C. *Biomechanics: Mechanical properties of living tissues*. 1993
79. Guo X, Kassab GS. Distribution of stress and strain along the porcine aorta and coronary arterial tree. *American journal of physiology. Heart and circulatory physiology*. 2004;286:H2361-2368
80. Gupta V, Grande-Allen KJ. Effects of static and cyclic loading in regulating extracellular matrix synthesis by cardiovascular cells. *Cardiovascular research*. 2006;72:375-383
81. Greenwald SE, Berry CL. Improving vascular grafts: The importance of mechanical and haemodynamic properties. *J.Pathol*. 2000;190:292-299
82. Mattsson EJ, Kohler TR, Vergel SM, Clowes AW. Increased blood flow induces regression of intimal hyperplasia. *Arterioscler.Thromb.Vasc.Biol*. 1997;17:2245-2249
83. Dobrin PB, Littooy FN, Endean ED. Mechanical factors predisposing to intimal hyperplasia and medial thickening in autogenous vein grafts. *Surgery*. 1989;105:393-400
84. Wentzel JJ, Kloet J, Andhyiswara I, Oomen JA, Schuurbijs JC, de Smet BJ, Post MJ, de Kleijn D, Pasterkamp G, Borst C, Slager CJ, Krams R. Shear-stress and wall-stress regulation of vascular remodeling after balloon angioplasty: Effect of matrix metalloproteinase inhibition. *Circulation*. 2001;104:91-96
85. Libby P, Schwartz D, Brogi E, Tanaka H, Clinton SK. A cascade model for restenosis. A special case of atherosclerosis progression. *Circulation*. 1992;86:III47-III52
86. Mills B, Robb T, Larson DF. Intimal hyperplasia: Slow but deadly. *Perfusion*. 2012;27:520-528
87. Schwartz SM, deBlois D, O'Brien ER. The intima. Soil for atherosclerosis and restenosis. *Circ.Res*. 1995;77:445-465
88. Cizek SM, Bedri S, Talusan P, Silva N, Lee H, Stone JR. Risk factors for atherosclerosis and the development of preatherosclerotic intimal hyperplasia. *Cardiovascular pathology : the official journal of the Society for Cardiovascular Pathology*. 2007;16:344-350
89. Schillinger M, Exner M, Sabeti S, Amighi J, Wagner O, Ahmadi R, Minar E. Excessive carotid intimal neointimal formation predicts late cardiovascular events. *Journal of endovascular therapy : an official journal of the International Society of Endovascular Specialists*. 2004;11:229-239
90. Goel SA, Guo LW, Liu B, Kent KC. Mechanisms of post-intervention arterial remodelling. *Cardiovascular research*. 2012;96:363-371

91. Fung Y-c. *Biomechanics: Circulation*. New York: Springer Verlag; 1997.
92. Stone PH, Coskun AU, Kinlay S, Clark ME, Sonka M, Wahle A, Ilegbusi OJ, Yeghiazarians Y, Popma JJ, Orav J, Kuntz RE, Feldman CL. Effect of endothelial shear stress on the progression of coronary artery disease, vascular remodeling, and in-stent restenosis in humans: In vivo 6-month follow-up study. *Circulation*. 2003;108:438-444
93. Paszkowiak JJ, Dardik A. Arterial wall shear stress: Observations from the bench to the bedside. *Vasc.Endovascular.Surg*. 2003;37:47-57
94. Gimbrone MA, Jr., Topper JN, Nagel T, Anderson KR, Garcia-Cardena G. Endothelial dysfunction, hemodynamic forces, and atherogenesis. *Annals of the New York Academy of Sciences*. 2000;902:230-239; discussion 239-240
95. Palumbo R, Gaetano C, Antonini A, Pompilio G, Bracco E, Rönstrand L, Heldin C-H, Capogrossi MC. Different effects of high and low shear stress on platelet-derived growth factor isoform release by endothelial cells: Consequences for smooth muscle cell migration. *Arteriosclerosis, thrombosis, and vascular biology*. 2002;22:405-411
96. Arenas IA, Xu Y, Davidge ST. Age-associated impairment in vasorelaxation to fluid shear stress in the female vasculature is improved by tnfr- α antagonism. *Am J Physiol Heart Circ.Physiol*. 2006;290:H1259-H1263
97. Bao X, Lu C, Frangos JA. Temporal gradient in shear but not steady shear stress induces pdgf- α and mcp-1 expression in endothelial cells: Role of no, nf kappa b, and egr-1. *Arterioscler.Thromb.Vasc.Biol*. 1999;19:996-1003
98. Garanich JS, Pahakis M, Tarbell JM. Shear stress inhibits smooth muscle cell migration via nitric oxide-mediated downregulation of matrix metalloproteinase-2 activity. *American journal of physiology. Heart and circulatory physiology*. 2005;288:H2244-2252
99. Guzman RJ, Abe K, Zarins CK. Flow-induced arterial enlargement is inhibited by suppression of nitric oxide synthase activity in vivo. *Surgery*. 1997;122:273-279
100. Marano G, Palazzesi S, Vergari A, Ferrari AU. Protection by shear stress from collar-induced intimal thickening: Role of nitric oxide. *Arteriosclerosis, thrombosis, and vascular biology*. 1999;19:2609-2614
101. Tronc F, Wassef M, Esposito B, Henrion D, Glagov S, Tedgui A. Role of no in flow-induced remodeling of the rabbit common carotid artery. *Arterioscler.Thromb.Vasc.Biol*. 1996;16:1256-1262
102. Zhang Y, He X, Chen X, Ma H, Liu D, Luo J, Du Z, Jin Y, Xiong Y, He J, Fang D, Wang K, Lawson WE, Hui JC, Zheng Z, Wu G. Enhanced external counterpulsation inhibits intimal hyperplasia by modifying shear stress responsive gene expression in hypercholesterolemic pigs. *Circulation*. 2007;116:526-534
103. Dancu MB, Berardi DE, Vanden Heuvel JP, Tarbell JM. Asynchronous shear stress and circumferential strain reduces endothelial no synthase and cyclooxygenase-2 but induces endothelin-1 gene expression in endothelial cells. *Arteriosclerosis, thrombosis, and vascular biology*. 2004;24:2088-2094
104. Andrews AM, Jaron D, Buerk DG, Kirby PL, Barbee KA. Direct, real-time measurement of shear stress-induced nitric oxide produced from endothelial cells in vitro. *Nitric oxide : biology and chemistry / official journal of the Nitric Oxide Society*. 2010;23:335-342
105. Stepp DW, Merkus D, Nishikawa Y, Chilian WM. Nitric oxide limits coronary vasoconstriction by a shear stress-dependent mechanism. *American journal of physiology. Heart and circulatory physiology*. 2001;281:H796-803
106. Colotti C, Vittorini S, Ottaviano V, Maltinti M, Angeli V, Del Ry S, Giannessi D. Nitric oxide treatment reduces neo-intimal formation and modulates osteopontin expression in an ex-vivo human model of intimal hyperplasia. *Cytokine*. 2009;46:228-235

107. Hou D, Narciso H, Kamdar K, Zhang P, Barclay B, March KL. Stent-based nitric oxide delivery reducing neointimal proliferation in a porcine carotid overstretch injury model. *Cardiovascular and interventional radiology*. 2005;28:60-65
108. Harnek J, Zoucas E, de Sa VP, Ekblad E, Arner A, Stenram U. Intimal hyperplasia in balloon dilated coronary arteries is reduced by local delivery of the no donor, sin-1 via a cgmp-dependent pathway. *BMC cardiovascular disorders*. 2011;11:30
109. Markos F, Ruane O'Hora T, Noble MIM. What is the mechanism of flow-mediated arterial dilatation. *Clin Exp Pharmacol Physiol*. 2013;40:489-494
110. Kumagai R, Lu X, Kassab GS. Role of glycocalyx in flow-induced production of nitric oxide and reactive oxygen species. *Free Radic Biol Med*. 2009;47:600-607
111. Liu X, Fan Y, Deng X. Mechanotransduction of flow-induced shear stress by endothelial glycocalyx fibers is torque determined. *ASAIO J*. 2011;57:487-494
112. Zwolak RM, Adams MC, Clowes aW. Kinetics of vein graft hyperplasia: Association with tangential stress. *Journal of vascular surgery*. 1987;5:126-136
113. Langille BL, Brownlee RD, Adamson SL. Perinatal aortic growth in lambs: Relation to blood flow changes at birth. *Am J Physiol*. 1990;259:H1247-1253
114. Levy BI, Michel JB, Salzmann JL, Azizi M, Poitevin P, Safar M, Camilleri JP. Effects of chronic inhibition of converting enzyme on mechanical and structural properties of arteries in rat renovascular hypertension. *Circ Res*. 1988;63:227-239
115. Intengan HD, Schiffrin EL. Vascular remodeling in hypertension: Roles of apoptosis, inflammation, and fibrosis. *Hypertension*. 2001;38:581-587
116. Ailawadi G, Eliason JL, Upchurch GR. Current concepts in the pathogenesis of abdominal aortic aneurysm. *Journal of vascular surgery*. 2003;38:584-588
117. Gambillara V, Thacher T, Silacci P, Stergiopulos N. Effects of reduced cyclic stretch on vascular smooth muscle cell function of pig carotids perfused ex vivo. *Am J Hypertens*. 2008;21:425-431
118. Chandrasekar B, Nelson JF, Colston JT, Freeman GL. Calorie restriction attenuates inflammatory responses to myocardial ischemia-reperfusion injury. *American journal of physiology. Heart and circulatory physiology*. 2001;280:H2094-2102
119. Schmid H, Grytsan A, Poshtan E, Watton PN, Itskov M. Influence of differing material properties in media and adventitia on arterial adaptation--application to aneurysm formation and rupture. *Comput Methods Biomech Biomed Engin*. 2013;16:33-53
120. Sommer G, Regitnig P, Költringer L, Holzapfel GA. Biaxial mechanical properties of intact and layer-dissected human carotid arteries at physiological and supraphysiological loadings. *American journal of physiology. Heart and circulatory physiology*. 2010;298:H898-912
121. Holzapfel GA, Sommer G, Gasser CT, Regitnig P. Determination of layer-specific mechanical properties of human coronary arteries with nonatherosclerotic intimal thickening and related constitutive modeling. *American journal of physiology. Heart and circulatory physiology*. 2005;289:H2048-2058
122. Kulik TJ, Alvarado SP. Effect of stretch on growth and collagen synthesis in cultured rat and lamb pulmonary arterial smooth muscle cells. *J Cell Physiol*. 1993;157:615-624
123. Sumpio BE, Banes AJ, Link WG, Johnson G. Enhanced collagen production by smooth muscle cells during repetitive mechanical stretching. *Arch Surg*. 1988;123:1233-1236
124. O'Callaghan CJ, Williams B. Mechanical strain-induced extracellular matrix production by human vascular smooth muscle cells: Role of tgf-beta(1). *Hypertension*. 2000;36:319-324
125. Lee RT, Yamamoto C, Feng Y, Potter-Perigo S, Briggs WH, Landschulz KT, Turi TG, Thompson JF, Libby P, Wight TN. Mechanical strain induces specific changes in the synthesis and organization of proteoglycans by vascular smooth muscle cells. *The Journal of biological chemistry*. 2001;276:13847-13851

126. Gusic RJ, Myung R, Petko M, Gaynor JW, Gooch KJ. Shear stress and pressure modulate saphenous vein remodeling ex vivo. *Journal of biomechanics*. 2005;38:1760-1769
127. Lawrence AR, Gooch KJ. Differences in transmural pressure and axial loading ex vivo affect arterial remodeling and material properties. *J Biomech Eng*. 2009;131:101009
128. Haghighipour N, Tafazzoli-Shadpour M, Shokrgozar MA, Amini S. Effects of cyclic stretch waveform on endothelial cell morphology using fractal analysis. *Artif Organs*. 2010;34:481-490
129. Liu SQ, Moore MM, Yap C. Prevention of mechanical stretch-induced endothelial and smooth muscle cell injury in experimental vein grafts. *J Biomech Eng*. 2000;122:31-38
130. Huynh TT, Davies MG, Trovato MJ, Svendsen E, Hagen PO. Alterations in wall tension and shear stress modulate tyrosine kinase signaling and wall remodeling in experimental vein grafts. *J. Vasc. Surg*. 1999;29:334-344
131. Hellstrand P, Albinsson S. Stretch-dependent growth and differentiation in vascular smooth muscle: Role of the actin cytoskeleton. *Can.J Physiol Pharmacol*. 2005;83:869-875
132. Cornelissen J, Armstrong J, Holt CM. Mechanical stretch induces phosphorylation of p38-mapk and apoptosis in human saphenous vein. *Arterioscler.Thromb.Vasc Biol*. 2004;24:451-456
133. Kohler TR, Jawien A. Flow affects development of intimal hyperplasia after arterial injury in rats. *Arterioscler.Thromb*. 1992;12:963-971
134. Doriot PA, Dorsaz PA, Dorsaz L, De Benedetti E, Chatelain P, Delafontaine P. In-vivo measurements of wall shear stress in human coronary arteries. *Coron Artery Dis*. 2000;11:495-502
135. Pantos I, Patatoukas G, Efstathopoulos EP, Katritsis D. In vivo wall shear stress measurements using phase-contrast mri. *Expert Rev Cardiovasc Ther*. 2007;5:927-938
136. Reneman RS, Hoeks APG. Wall shear stress as measured in vivo: Consequences for the design of the arterial system. *Med Biol Eng Comput*. 2008;46:499-507
137. Spencer MP, Reid JM. Quantitation of carotid stenosis with continuous-wave (c-w) doppler ultrasound. *Stroke; a journal of cerebral circulation*. 1979;10:326-330
138. de Monchy CC, Lepage L, Boutron I, Leye M, Detaint D, Hyafil F, Brochet E, Iung B, Vahanian A, Messika-Zeitoun D. Usefulness of the right parasternal view and non-imaging continuous-wave doppler transducer for the evaluation of the severity of aortic stenosis in the modern area. *Eur J Echocardiogr*. 2009;10:420-424
139. Nascimben Matheus C, Caldeira de Oliveira Guirro E. Change in blood flow velocity demonstrated by doppler ultrasound in upper limb after axillary dissection surgery for the treatment of breast cancer. *Breast Cancer Res Treat*. 2011;127:697-704
140. Mynard JP, Wasserman BA, Steinman DA. Errors in the estimation of wall shear stress by maximum doppler velocity. *Atherosclerosis*. 2013;227:259-266
141. Puri R, Leong DP, Nicholls SJ, Liew GYL, Nelson AJ, Carbone A, Copus B, Wong DT, Beltrame JF, Worthley SG, Worthley MI. Coronary artery wall shear stress is associated with endothelial dysfunction and expansive arterial remodelling in patients with coronary artery disease. *EuroIntervention*. 2014
142. Park DW, Kruger GH, Rubin JM, Hamilton J, Gottschalk P, Dodde RE, Shih AJ, Weitzel WF. Quantification of ultrasound correlation-based flow velocity mapping and edge velocity gradient measurement. *J Ultrasound Med*. 2013;32:1815-1830
143. Filardi V. Carotid artery stenosis near a bifurcation investigated by fluid dynamic analyses. *Neuroradiol J*. 2013;26:439-453
144. Safar ME, London GM. Arterial and venous compliance in sustained essential hypertension. *Hypertension*. 1987;10:133-139
145. Holzapfel GA, Gasser TC, Ogden RW. A new constitutive framework for arterial wall mechanics and a comparative study of material models. *J Elasticity*. 2000;61:1-48

146. Hoskins PR, Hardman D. Three-dimensional imaging and computational modelling for estimation of wall stresses in arteries. *Br J Radiol.* 2009;82 Spec No 1:S3-17
147. Kuhl E, Maas R, Himpel G, Menzel A. Computational modeling of arterial wall growth. Attempts towards patient-specific simulations based on computer tomography. *Biomech Model Mechanobiol.* 2007;6:321-331
148. Ohayon J, Gharib AM, Garcia A, Heroux J, Yazdani SK, Malvè M, Tracqui P, Martinez M-A, Doblare M, Finet G, Pettigrew RI. Is arterial wall-strain stiffening an additional process responsible for atherosclerosis in coronary bifurcations?: An in vivo study based on dynamic ct and mri. *American journal of physiology. Heart and circulatory physiology.* 2011;301:H1097-1106
149. Tham DM, Martin-mcnulty B, Wang Y-x, Cunha VD, Wilson W, Athanassious CN, Powers AF, Sullivan ME, Rutledge JC, Kirabo A, Kearns PN, Jarajapu YP, Sasser JM, Oh SP, Maria B, Kasahara H, Cardounel AJ, Baylis C, Wagner K-u, Peter P. Angiotensin ii injures the arterial wall causing increased aortic stiffening in apolipoprotein e-deficient mice levels of reactive oxygen species. *American Journal Of Physiology.* 2011
150. Mahmoud A, Frisbee J. In vivo vascular wall tissue characterization using a strain tensor measuring (stm) technique for flow-mediated vasodilation analyses. *Physics in Medicine.* 2009;54:6217-6238
151. Deleaval F, Bouvier A, Finet G, Cloutier G, Yazdani SK, Le Floc'h S, Clarysse P, Pettigrew RI, Ohayon J. The intravascular ultrasound elasticity-palpography technique revisited: A reliable tool for the in vivo detection of vulnerable coronary atherosclerotic plaques. *Ultrasound Med Biol.* 2013;39:1469-1481
152. Kim EK, Chang S-A, Jang SY, Kim Y, Kim SM, Oh JK, Choe YH, Kim D-K. Assessment of regional aortic stiffness with cardiac magnetic resonance imaging in a healthy asian population. *Int J Cardiovasc Imaging.* 2013;29 Suppl 1:57-64
153. Lin AP, Bennett E, Wisk LE, Gharib M, Fraser SE, Wen H. Circumferential strain in the wall of the common carotid artery: Comparing displacement-encoded and cine mri in volunteers. *Magn Reson Med.* 2008;60:8-13
154. Draney MT, Herfkens RJ, Hughes TJR, Pelc NJ, Wedding KL, Zarins CK, Taylor CA. Quantification of vessel wall cyclic strain using cine phase contrast magnetic resonance imaging. *Ann Biomed Eng.* 2002;30:1033-1045
155. Masson I, Beaussier H, Boutouyrie P, Laurent S, Humphrey JD, Zidi M. Carotid artery mechanical properties and stresses quantified using in vivo data from normotensive and hypertensive humans. *Biomech Model Mechanobiol.* 2011;10:867-882
156. Niu L, Qian M, Song R, Meng L, Liu X, Zheng H. A 2d non-invasive ultrasonic method for simultaneous measurement of arterial strain and flow pattern. *Clin Physiol Funct Imaging.* 2012;32:323-329
157. Behfar A, Yamada S, Crespo-Diaz R, Nesbitt JJ, Rowe La, Perez-Terzic C, Gaussin V, Homsy C, Bartunek J, Terzic A. Guided cardiopoiesis enhances therapeutic benefit of bone marrow human mesenchymal stem cells in chronic myocardial infarction. *Journal of the American College of Cardiology.* 2010;56:721-734
158. Wu X, Cheng J, Li P, Yang M, Qiu S, Liu P, Du J. Mechano-sensitive transcriptional factor egr-1 regulates insulin-like growth factor-1 receptor expression and contributes to neointima formation in vein grafts. *Arteriosclerosis, thrombosis, and vascular biology.* 2010;30:471-476
159. Gusic RJ, Petko M, Myung R, William Gaynor J, Gooch KJ. Mechanical properties of native and ex vivo remodeled porcine saphenous veins. *Journal of biomechanics.* 2005;38:1770-1779
160. Ballyk PD, Walsh C, Butany J, Ojha M. Compliance mismatch may promote graft — artery intimal hyperplasia by altering suture-line stresses. *Annals of Vascular Surgery.* 1998;31:229-237

161. Cheng C, Tempel D, van Haperen R, van der Baan A, Grosveld F, Daemen MJ, Krams R, de Crom R. Atherosclerotic lesion size and vulnerability are determined by patterns of fluid shear stress. *Circulation*. 2006;113:2744-2753
162. Cunningham KS, Gotlieb AI. The role of shear stress in the pathogenesis of atherosclerosis. *Lab Invest*. 2005;85:9-23
163. Haruguchi H, Teraoka S. Intimal hyperplasia and hemodynamic factors in arterial bypass and arteriovenous grafts: A review. *J Artif Organs*. 2003;6:227-235
164. Sho M, Sho E, Singh TM, Komatsu M, Sugita A, Xu C, Nanjo H, Zarins CK, Masuda H. Subnormal shear stress-induced intimal thickening requires medial smooth muscle cell proliferation and migration. *Exp.Mol.Pathol*. 2002;72:150-160
165. Song RH, Kocharyan HK, Fortunato JE, Glagov S, Bassiouny HS. Increased flow and shear stress enhance in vivo transforming growth factor-beta1 after experimental arterial injury. *Arterioscler.Thromb.Vasc.Biol*. 2000;20:923-930
166. Stein JH, Korcarz CE, Hurst RT, Lonn E, Kendall CB, Mohler ER, Najjar SS, Rembold CM, Post WS. Use of carotid ultrasound to identify subclinical vascular disease and evaluate cardiovascular disease risk: A consensus statement from the american society of echocardiography carotid intima-media thickness task force endorsed by the society for vascular medicine. *Journal of the American Society of Echocardiography*. 2008;21:93-111
167. Rodriguez-Macias KA, Lind L, Naessen T. Thicker carotid intima layer and thinner media layer in subjects with cardiovascular diseases: An investigation using noninvasive high-frequency ultrasound. *Atherosclerosis*. 2006;189:393-400
168. Garvin RP, Duryee MJ, Klassen LW, Thiele GM, Anderson DR. Ultrasound imaging in an animal model of vascular inflammation following balloon injury. *Ultrasound in Medicine & Biology*. 2012;38:1552-1558
169. Daugherty A, Cassis LA. Mouse models of abdominal aortic aneurysms. *Arteriosclerosis, thrombosis, and vascular biology*. 2004;24:429-434
170. Thompson RW. Basic science of abdominal aortic aneurysms: Emerging therapeutic strategies for an unresolved clinical problem. *Curr.Opin.Cardiol*. 1996;11:504-518
171. Park DW, Kruger GH, Rubin JM, Hamilton J, Gottschalk P, Dodde RE, Shih AJ, Weitzel WF. In vivo vascular wall shear rate and circumferential strain of renal disease patients. *Ultrasound in Medicine & Biology*. 2013;39:241-252
172. Mahmoud AM, Sandoval C, Teng B, Schnermann JB, Martin KH, Jamal Mustafa S, Mukdadi OM. High-resolution vascular tissue characterization in mice using 55 mhZ ultrasound hybrid imaging. *Ultrasonics*. 2013;53:727-738
173. Peng Y, Popovic ZB, Sopko N, Drinko J, Zhang Z, Thomas JD, Penn MS. Speckle tracking echocardiography in the assessment of mouse models of cardiac dysfunction. *American journal of physiology. Heart and circulatory physiology*. 2009;297:H811-820
174. Greaby R, Zderic V, Vaezy S. Pulsatile flow phantom for ultrasound image-guided hifu treatment of vascular injuries. *Ultrasound in medicine & biology*. 2007;33:1269-1276
175. McVeigh ER. Mri of myocardial function: Motion tracking techniques. *Magnetic resonance imaging*. 1996;14:137-150
176. Van Leuven SL, Waldman LK, McCulloch aD, Covell JW. Gradients of epicardial strain across the perfusion boundary during acute myocardial ischemia. *The American journal of physiology*. 1994;267:H2348-2362
177. Graf S, Garipey J, Maddonneau M, Armentano R, Mansour S, Barra J, Simon A, Levenson J. Experimental and clinical validation of arterial diameter waveform and intimal media thickness obtained from b-mode ultrasound image processing. *Ultrasound in medicine* 1999;25:1353-1363

178. Nayar SK, Watanabe M, Noguchi M. Real-time focus range sensor. *IEEE Transactions on Pattern Analysis and Machine Intelligence*. 1996;18:1186-1198
179. Konrath R, Schroder W. Telecentric lenses for imaging in particle image velocimetry : A new stereoscopic approach. *Experiments in Fluids*. 2002;33:703-708
180. Watanabe M, Nayar S. Telecentric optics for focus analysis. *Analysis and Machine Intelligence*,. 1997;19:1360-1365
181. Kelly DJ, Azeloglu EU, Kochupura PV, Sharma GS, Gaudette GR. Accuracy and reproducibility of a subpixel extended phase correlation method to determine micron level displacements in the heart. *Medical engineering & physics*. 2007;29:154-162
182. Favreau JT, Yu P, Ozaki CK, Gaudette GR. A novel method for recording wall strain in a murine vein graft model. *Bioengineering Conference (NEBEC), 2011 IEEE 37th Annual Northeast*. 2011;⑥:1-2
183. West AR, Zaman N, Cole DJ, Walker MJ, Legant WR, Boudou T, Chen CS, Favreau JT, Gaudette GR, Cowley EA, Maksym GN. Development and characterization of a 3d multicell microtissue culture model of airway smooth muscle. *Am J Physiol Lung Cell Mol Physiol*. 2013;304:L4-L16
184. Brum J, Bia D, Benech N, Balay G, Armentano RL, Negreira C. Arterial diameter measurement using high resolution ultrasonography: In vitro validation. *Conf Proc IEEE Eng Med Biol Soc*. 2011;2011:203-206
185. Foroosh H, Zerubia JB, Berthod M. Extension of phase correlation to subpixel registration. *IEEE transactions on image processing : a publication of the IEEE Signal Processing Society*. 2002;11:188-200
186. Kelly DJ, Rosen AB, Schuldt AJ, Kochupura PV, Doronin SV, Potapova IA, Azeloglu EU, Badylak SF, Brink PR, Cohen IS, Gaudette GR. Increased myocyte content and mechanical function within a tissue-engineered myocardial patch following implantation. *Tissue Eng Part A*. 2009;15:2189-2201
187. Aihara H, Soga Y, Kuramitsu S. Serial optical coherence tomography assessments at 2- and 4-month follow-up after paclitaxel-eluting stenting of the superficial femoral artery. *Cardiovasc Interv Ther*. 2014
188. Dong L, Maehara A, Nazif TM, Pollack AT, Saito S, Rabbani LE, Apfelbaum MA, Dalton K, Moses JW, Jorde UP, Xu K, Mintz GS, Mancini DM, Weisz G. Optical coherence tomographic evaluation of transplant coronary artery vasculopathy with correlation to cellular rejection. *Circ Cardiovasc Interv*. 2014;7:199-206
189. Fujimoto JG, Pitris C, Boppart SA, Brezinski ME. Optical coherence tomography: An emerging technology for biomedical imaging and optical biopsy. *Neoplasia*. 2000;2:9-25
190. Vorp DA, Raghavan ML, Webster MW. Mechanical wall stress in abdominal aortic aneurysm: Influence of diameter and asymmetry. *Journal of vascular surgery*. 1998;27:632-639
191. Vorp DA. Biomechanics of abdominal aortic aneurysm. *Journal of biomechanics*. 2007;40:1887-1902
192. Fillinger MF, Marra SP, Raghavan ML, Kennedy FE. Prediction of rupture risk in abdominal aortic aneurysm during observation: Wall stress versus diameter. *Journal of vascular surgery*. 2003;37:724-732
193. He CM, Roach MR. The composition and mechanical properties of abdominal aortic aneurysms. *Journal of vascular surgery*. 1994;20:6-13
194. Daugherty A, Manning MW, Cassis LA. Angiotensin ii promotes atherosclerotic lesions and aneurysms in apolipoprotein e-deficient mice. *J Clin Invest*. 2000;105:1605-1612
195. Wang YX, Martin-McNulty B, Freay AD, Sukovich DA, Halks-Miller M, Li WW, Vergona R, Sullivan ME, Morser J, Dole WP, Deng GG. Angiotensin ii increases urokinase-type plasminogen activator expression and induces aneurysm in the abdominal aorta of apolipoprotein e-deficient mice. *Am J Pathol*. 2001;159:1455-1464

196. Cao RY, Amand T, Ford MD, Piomelli U, Funk CD. The murine angiotensin ii-induced abdominal aortic aneurysm model: Rupture risk and inflammatory progression patterns. *Front Pharmacol.* 2010;1:1-7
197. Manning MW, Cassi LA, Huang J, Szilvassy SJ, Daugherty A. Abdominal aortic aneurysms: Fresh insights from a novel animal model of the disease. *Vasc Med.* 2002;7:45-54
198. Daugherty A, Manning MW, Cassis LA. Antagonism of at2 receptors augments angiotensin ii-induced abdominal aortic aneurysms and atherosclerosis. *Br J Pharmacol.* 2001;134:865-870
199. Bergoeing MP, Arif B, Hackmann AE, Ennis TL, Thompson RW, Curci JA. Cigarette smoking increases aortic dilatation without affecting matrix metalloproteinase-9 and -12 expression in a modified mouse model of aneurysm formation. *Journal of vascular surgery.* 2007;45:1217-1227
200. Sho E, Sho M, Nanjo H, Kawamura K, Masuda H, Dalman RL. Hemodynamic regulation of cd34+ cell localization and differentiation in experimental aneurysms. *Arteriosclerosis, thrombosis, and vascular biology.* 2004;24:1916-1921
201. Chiou AC, Chiu B, Oppat WF, Matsumura JS, Chisholm RL, Pearce WH. Transrectal ultrasound assessment of murine aorta and iliac arteries. *J Surg Res.* 2000;88:193-199
202. Knipp BS, Ailawadi G, Sullivan VV, Roelofs KJ, Henke PK, Stanley JC, Upchurch GR, Jr. Ultrasound measurement of aortic diameters in rodent models of aneurysm disease. *J Surg Res.* 2003;112:97-101
203. McFadden EP, Chaabane L, Contard F, Guerrier D, Briguet A, Douek P, Soulas EC. In vivo magnetic resonance imaging of large spontaneous aortic aneurysms in old apolipoprotein e-deficient mice. *Invest Radiol.* 2004;39:585-590
204. Roger VL, Go AS, Lloyd-Jones DM, Adams RJ, Berry JD, Brown TM, Carnethon MR, Dai S, de Simone G, Ford ES, Fox CS, Fullerton HJ, Gillespie C, Greenlund KJ, Hailpern SM, Heit JA, Ho PM, Howard VJ, Kissela BM, Kittner SJ, Lackland DT, Lichtman JH, Lisabeth LD, Makuc DM, Marcus GM, Marelli A, Matchar DB, McDermott MM, Meigs JB, Moy CS, Mozaffarian D, Mussolino ME, Nichol G, Paynter NP, Rosamond WD, Sorlie PD, Stafford RS, Turan TN, Turner MB, Wong ND, Wylie-Rosett J, Roger VL, Turner MB. Heart disease and stroke statistics--2011 update: A report from the american heart association. *Circulation.* 2011;123:e18-e209
205. Diehm N, Dick F, Schaffner T, Schmidli J, Kalka C, Di Santo S, Voelzmann J, Baumgartner I. Novel insight into the pathobiology of abdominal aortic aneurysm and potential future treatment concepts. *Prog Cardiovasc Dis.* 2007;50:209-217
206. Sakalihasan N, Limet R, Defawe OD. Abdominal aortic aneurysm. *Lancet.* 2005;365:1577-1589
207. Steinman DA, Vorp DA, Ethier CR. Computational modeling of arterial biomechanics: Insights into pathogenesis and treatment of vascular disease. *Journal of vascular surgery.* 2003;37:1118-1128
208. McGloughlin TM, Doyle BJ. New approaches to abdominal aortic aneurysm rupture risk assessment: Engineering insights with clinical gain. *Arteriosclerosis, thrombosis, and vascular biology.* 2010;30:1687-1694
209. Hartley CJ, Reddy AK, Madala S, Martin-McNulty B, Vergona R, Sullivan ME, Halks-Miller M, Taffet GE, Michael LH, Entman ML, Wang YX. Hemodynamic changes in apolipoprotein e-knockout mice. *American journal of physiology. Heart and circulatory physiology.* 2000;279:H2326-2334
210. Rossmeis M, Rim JS, Koza RA, Kozak LP. Variation in type 2 diabetes--related traits in mouse strains susceptible to diet-induced obesity. *Diabetes.* 2003;52:1958-1966
211. Police SB, Thatcher SE, Charnigo R, Daugherty A, Cassis LA. Obesity promotes inflammation in periaortic adipose tissue and angiotensin ii-induced abdominal aortic aneurysm formation. *Arteriosclerosis, thrombosis, and vascular biology.* 2009;29:1458-1464

212. Moxon JV, Parr A, Emeto TI, Walker P, Norman PE, Golledge J. Diagnosis and monitoring of abdominal aortic aneurysm: Current status and future prospects. *Curr Probl Cardiol.* 2010;35:512-548
213. Cassis LA, Gupte M, Thayer S, Zhang X, Charnigo R, Howatt DA, Rateri DL, Daugherty A. Ang ii infusion promotes abdominal aortic aneurysms independent of increased blood pressure in hypercholesterolemic mice. *American journal of physiology. Heart and circulatory physiology.* 2009;296:H1660-1665
214. Public health service policy on humane care and use of laboratory animals. *Office of Laboratory Animal Welfare, National Institutes of Health, Bethesda, MD.* 2002
215. Alexander J, Hafley G, Harrington R. Efficacy and safety of edifoligide, an e2f transcription factor decoy, for prevention of vein graft failure following coronary artery bypass graft surgery: Prevent iv: A. *JAMA: the journal of the american medical association.* 2005;294:2446-2454
216. Ainslie KM, Garanich JS, Dull RO, Tarbell JM. Vascular smooth muscle cell glycocalyx influences shear stress-mediated contractile response. *J Appl.Physiol.* 2005;98:242-249
217. Asakura T, Karino T. Flow patterns and spatial distribution of atherosclerotic lesions in human coronary arteries. *Circ.Res.* 1990;66:1045-1066
218. Baldwin ZK, Chandiwal A, Huang W, Vosicky JE, Balasubramanian V, Curi MA, Schwartz LB. Slower onset of low shear stress leads to less neointimal thickening in experimental vein grafts. *Ann.Vasc Surg.* 2006;20:106-113
219. Chiu JJ, Lee PL, Chen CN, Lee CI, Chang SF, Chen LJ, Lien SC, Ko YC, Usami S, Chien S. Shear stress increases icam-1 and decreases vcam-1 and e-selectin expressions induced by tumor necrosis factor-[alpha] in endothelial cells. *Arterioscler.Thromb.Vasc.Biol.* 2004;24:73-79
220. Johnson GA, Hung TK, Brant AM, Borovetz HS. Experimental determination of wall shear rate in canine carotid arteries perfused in vitro. *J.Biomech.* 1989;22:1141-1150
221. Keynton RS, Evancho MM, Sims RL, Rodway NV, Gobin A, Rittgers SE. Intimal hyperplasia and wall shear in arterial bypass graft distal anastomoses: An in vivo model study. *J.Biomech.Eng.* 2001;123:464-473
222. Kraiss LW, Kirkman TR, Kohler TR, Zierler B, Clowes AW. Shear stress regulates smooth muscle proliferation and neointimal thickening in porous polytetrafluoroethylene grafts. *Arterioscler.Thromb.* 1991;11:1844-1852
223. Krams R, Wentzel JJ, Oomen JA, Schuurbiens JC, Andhyiswara I, Kloet J, Post M, de Smet B, Borst C, Slager CJ, Serruys PW. Shear stress in atherosclerosis, and vascular remodelling. *Semin.Interv.Cardiol.* 1998;3:39-44
224. Osterberg K, Mattsson E. Intimal hyperplasia in mouse vein grafts is regulated by flow. *J Vasc Res.* 2005;42:13-20
225. Harmon EY, Fronhofer V, Keller RS, Feustel PJ, Brosnan MJ, von der Thüsen JH, Loegering DJ, Lennartz MR. Ultrasound biomicroscopy for longitudinal studies of carotid plaque development in mice: Validation with histological endpoints. *PLoS One.* 2012;7:e29944
226. Cheng Y, Makarova N, Tsukahara R. Lysophosphatidic acid-induced arterial wall remodeling: Requirement of ppar γ ³ but not lpa 1 or lpa 2 gpcr. *Cellular signalling.* 2009;21:1874-1884
227. Chiu J, Chien S. Effects of disturbed flow on vascular endothelium: Pathophysiological basis and clinical perspectives. *Physiological Reviews.* 2011:327-387
228. Chow M-J, Mondonedo JR, Johnson VM, Zhang Y. Progressive structural and biomechanical changes in elastin degraded aorta. *Biomech Model Mechanobiol.* 2013;12:361-372
229. Chajara A, Delpech B, Courel MN, Leroy M, Basuyau JP, Lévesque H. Effect of aging on neointima formation and hyaluronan, hyaluronidase and hyaluronectin production in injured rat aorta. *Atherosclerosis.* 1998;138:53-64

230. Kumar A, Lindner V. Remodeling with neointima formation in the mouse carotid artery after cessation of blood flow. *Arteriosclerosis, thrombosis, and vascular biology*. 1997;17:2238-2244
231. Lindner V, Fingerle J, Reidy MA. Mouse model of arterial injury. *Circ.Res*. 1993;73:792-796
232. Lindner V, Reidy MA. Expression of basic fibroblast growth factor and its receptor by smooth muscle cells and endothelium in injured rat arteries. An en face study. *Circ.Res*. 1993;73:589-595
233. Miano JM, Cserjesi P, Ligon KL, Periasamy M, Olson EN. Smooth muscle myosin heavy chain exclusively marks the smooth muscle lineage during mouse embryogenesis. *Circulation Research*. 1994;75:803-812
234. Nam D, Ni C-W, Rezvan A, Suo J, Budzyn K, Llanos A, Harrison D, Giddens D, Jo H. Partial carotid ligation is a model of acutely induced disturbed flow, leading to rapid endothelial dysfunction and atherosclerosis. *American journal of physiology. Heart and circulatory physiology*. 2009;297:H1535-1543
235. Korshunov VA, Berk BC. Flow-induced vascular remodeling in the mouse: A model for carotid intima-media thickening. *Arterioscler. Thromb. Vasc. Biol*. 2003;23:2185-2191
236. Shukla S, Nair R, Rolle MW, Braun KR, Chan CK, Johnson PY, Wight TN, McDevitt TC. Synthesis and organization of hyaluronan and versican by embryonic stem cells undergoing embryoid body differentiation. *The journal of histochemistry and cytochemistry : official journal of the Histochemistry Society*. 2010;58:345-358
237. Hui D. Intimal hyperplasia in murine models. *Current drug targets*. 2008;9:251-260
238. Favreau JT, Liu C, Yu P, Tao M, Mauro C, Gaudette GR, Ozaki CK. Acute reductions in mechanical wall strain precede the formation of intimal hyperplasia in a murine model of arterial occlusive disease. *Journal of vascular surgery*. 2013
239. Chen D, Ma L, Tham E-L, Maresh S, Lechler RI, McVey JH, Dorling A. Fibrocytes mediate intimal hyperplasia post-vascular injury and are regulated by two tissue factor-dependent mechanisms. *J Thromb Haemost*. 2013;11:963-974
240. Varcoe RL, Mikhail M, Guiffre AK, Pennings G, Vicaretti M, Hawthorne WJ, Fletcher JP, Medbury HJ. The role of the fibrocyte in intimal hyperplasia. *J Thromb Haemost*. 2006;4:1125-1133
241. Tang DL, Yang C, Ku DN. A 3-d thin-wall model with fluid-structure interactions for blood flow in carotid arteries with symmetric and asymmetric stenoses. *Comput Struct*. 1999;72:357-377
242. Huang X, Yang C, Zheng J, Bach R, Muccigrosso D, Woodard PK, Tang D. Higher critical plaque wall stress in patients who died of coronary artery disease compared with those who died of other causes: A 3d fsi study based on ex vivo mri of coronary plaques. *Journal of biomechanics*. 2014;47:432-437
243. Zhang P-F, Su H-J, Zhang M, Li J-F, Liu C-X, Ding S-F, Miao Y, Chen L, Li X-N, Yi X, Zhang Y. Atherosclerotic plaque components characterization and macrophage infiltration identification by intravascular ultrasound elastography based on b-mode analysis: Validation in vivo. *Int J Cardiovasc Imaging*. 2011;27:39-49
244. Koch RG, Tsamis A, D'Amore A, Wagner WR, Watkins SC, Gleason TG, Vorp DA. A custom image-based analysis tool for quantifying elastin and collagen micro-architecture in the wall of the human aorta from multi-photon microscopy. *Journal of biomechanics*. 2014;47:935-943
245. Rotmans JL, Velema E, Verhagen HJM, Blankensteijn JD, de Kleijn DPV, Stroes ESG, Pasterkamp G. Matrix metalloproteinase inhibition reduces intimal hyperplasia in a porcine arteriovenous-graft model. *Journal of vascular surgery*. 2004;39:432-439
246. Vijayan V, Smith FC, Angelini GD, Bulbulia RA, Jeremy JY. External supports and the prevention of neointima formation in vein grafts. *Eur.J.Vasc.Endovasc.Surg*. 2002;24:13-22
247. Jeremy JY, Gadsdon P, Shukla N, Vijayan V, Wyatt M, Newby AC, Angelini GD. On the biology of saphenous vein grafts fitted with external synthetic sheaths and stents. *Biomaterials*. 2007;28:895-908

- 248. Kohler TR, Kirkman TR, Clowes AW. The effect of rigid external support on vein graft adaptation to the arterial circulation. *Journal of vascular surgery*. 1989;9:277-285
- 249. Zilla P, Human P, Wolf M, Lichtenberg W, Rafiee N, Bezuidenhout D, Samodien N, Schmidt C, Franz T. Constrictive external nitinol meshes inhibit vein graft intimal hyperplasia in nonhuman primates. *J Thorac Cardiovasc Surg*. 2008;136:717-725

Appendix A: Reprint permissions

Permissions for Chapter 4

ELSEVIER LICENSE TERMS AND CONDITIONS

Jun 14, 2013

This is a License Agreement between John T Favreau ("You") and Elsevier ("Elsevier") provided by Copyright Clearance Center ("CCC"). The license consists of your order details, the terms and conditions provided by Elsevier, and the payment terms and conditions.

All payments must be made in full to CCC. For payment instructions, please see information listed at the bottom of this form.

Supplier

Elsevier Limited

The Boulevard, Langford Lane

Kidlington, Oxford, OX5 1GB, UK

Registered Company

1982084

Number

Customer name

John T Favreau

Customer address

60 Prescott Street

WORCESTER, MA 01605

License number

3167660763375

License date	Jun 14, 2013
Licensed content publisher	Elsevier
Licensed content publication	Journal of Vascular Surgery
Licensed content title	Murine ultrasound imaging for circumferential strain analyses in the angiotensin II abdominal aortic aneurysm model
Licensed content author	John T. Favreau, Binh T. Nguyen, Ian Gao, Peng Yu, Ming Tao, Jacob Schneiderman, Glenn R. Gaudette, C. Keith Ozaki
Licensed content date	August 2012
Licensed content volume number	56
Licensed content issue number	2
Number of pages	8
Start Page	462
End Page	469

Type of Use	reuse in a dissertation/dissertation
Portion	full article
Format	both print and electronic
Are you the author of this Elsevier article?	Yes
Will you be translating?	No
Order reference number	None
Title of your dissertation/dissertation	Cyclic mechanical strain reduction temporally precedes arterial intimal hyperplasia in a murine model
Expected completion date	May 2014
Estimated size (number of pages)	100
Elsevier VAT number	GB 494 6272 12
Permissions price	0.00 USD
VAT/Local Sales Tax	0.00 USD / None GBP
Total	0.00 USD
Terms and Conditions	

INTRODUCTION

1. The publisher for this copyrighted material is Elsevier. By clicking "accept" in connection with completing this licensing transaction, you agree that the following terms and conditions apply to this transaction (along with the Billing and Payment terms and conditions established by Copyright Clearance Center, Inc. ("CCC"), at the time that you opened your Rightslink account and that are available at any time at <http://myaccount.copyright.com>).

GENERAL TERMS

2. Elsevier hereby grants you permission to reproduce the aforementioned material subject to the terms and conditions indicated.

3. Acknowledgement: If any part of the material to be used (for example, figures) has appeared in our publication with credit or acknowledgement to another source, permission must also be sought from that source. If such permission is not obtained then that material may not be included in your publication/copies. Suitable acknowledgement to the source must be made, either as a footnote or in a reference list at the end of your publication, as follows:

“Reprinted from Publication title, Vol /edition number, Author(s), Title of article / title of chapter, Pages No., Copyright (Year), with permission from Elsevier [OR APPLICABLE SOCIETY COPYRIGHT OWNER].” Also Lancet special credit - “Reprinted from The Lancet, Vol. number, Author(s), Title of article, Pages No., Copyright (Year), with permission from Elsevier.”

4. Reproduction of this material is confined to the purpose and/or media for which permission is hereby given.

5. Altering/Modifying Material: Not Permitted. However figures and illustrations may be altered/adapted minimally to serve your work. Any other abbreviations, additions, deletions and/or any other alterations shall be made only with prior written authorization of Elsevier Ltd. (Please contact Elsevier at permissions@elsevier.com)

6. If the permission fee for the requested use of our material is waived in this instance, please be advised that your future requests for Elsevier materials may attract a fee.

7. Reservation of Rights: Publisher reserves all rights not specifically granted in the combination of (i) the license details provided by you and accepted in the course of this licensing transaction, (ii) these terms and conditions and (iii) CCC's Billing and Payment terms and conditions.

8. License Contingent Upon Payment: While you may exercise the rights licensed immediately upon issuance of the license at the end of the licensing process for the transaction, provided that you have disclosed complete and accurate details of your proposed use, no license is finally effective unless and until full payment is received from you (either by publisher or by CCC) as provided in CCC's Billing and Payment terms and conditions. If full payment is not received on a timely basis, then any license preliminarily granted shall be deemed automatically revoked and shall be void as if never granted. Further, in the event that you breach any of these terms and conditions or any of CCC's Billing and Payment terms and conditions, the license is automatically

revoked and shall be void as if never granted. Use of materials as described in a revoked license, as well as any use of the materials beyond the scope of an unrevoked license, may constitute copyright infringement and publisher reserves the right to take any and all action to protect its copyright in the materials.

9. Warranties: Publisher makes no representations or warranties with respect to the licensed material.

10. Indemnity: You hereby indemnify and agree to hold harmless publisher and CCC, and their respective officers, directors, employees and agents, from and against any and all claims arising out of your use of the licensed material other than as specifically authorized pursuant to this license.

11. No Transfer of License: This license is personal to you and may not be sublicensed, assigned, or transferred by you to any other person without publisher's written permission.

12. No Amendment Except in Writing: This license may not be amended except in a writing signed by both parties (or, in the case of publisher, by CCC on publisher's behalf).

13. Objection to Contrary Terms: Publisher hereby objects to any terms contained in any purchase order, acknowledgment, check endorsement or other writing prepared by you, which terms are inconsistent with these terms and conditions or CCC's Billing and Payment terms and conditions. These terms and conditions, together with CCC's Billing and Payment terms and conditions (which are incorporated herein), comprise the entire agreement between you and publisher (and CCC) concerning this licensing

transaction. In the event of any conflict between your obligations established by these terms and conditions and those established by CCC's Billing and Payment terms and conditions, these terms and conditions shall control.

14. Revocation: Elsevier or Copyright Clearance Center may deny the permissions described in this License at their sole discretion, for any reason or no reason, with a full refund payable to you. Notice of such denial will be made using the contact information provided by you. Failure to receive such notice will not alter or invalidate the denial. In no event will Elsevier or Copyright Clearance Center be responsible or liable for any costs, expenses or damage incurred by you as a result of a denial of your permission request, other than a refund of the amount(s) paid by you to Elsevier and/or Copyright Clearance Center for denied permissions.

LIMITED LICENSE

The following terms and conditions apply only to specific license types:

15. Translation: This permission is granted for non-exclusive world English rights only unless your license was granted for translation rights. If you licensed translation rights you may only translate this content into the languages you requested. A professional translator must perform all translations and reproduce the content word for word preserving the integrity of the article. If this license is to re-use 1 or 2 figures then permission is granted for non-exclusive world rights in all languages.

16. Website: The following terms and conditions apply to electronic reserve and author websites:

Electronic reserve: If licensed material is to be posted to website, the web site is to be password-protected and made available only to bona fide students registered on a relevant course if:

This license was made in connection with a course,

This permission is granted for 1 year only. You may obtain a license for future website posting,

All content posted to the web site must maintain the copyright information line on the bottom of each image,

A hyper-text must be included to the Homepage of the journal from which you are licensing at <http://www.sciencedirect.com/science/journal/xxxxx> or the Elsevier homepage for books at <http://www.elsevier.com> , and

Central Storage: This license does not include permission for a scanned version of the material to be stored in a central repository such as that provided by Heron/XanEdu.

17. Author website for journals with the following additional clauses:

All content posted to the web site must maintain the copyright information line on the bottom of each image, and the permission granted is limited to the personal version of your paper. You are not allowed to download and post the published electronic version of your article (whether PDF or HTML, proof or final version), nor may you scan the printed edition to create an electronic version. A hyper-text must be included to the Homepage of the journal from which you are licensing at <http://www.sciencedirect.com/science/journal/xxxxx> . As part of our normal production

process, you will receive an e-mail notice when your article appears on Elsevier's online service ScienceDirect (www.sciencedirect.com). That e-mail will include the article's Digital Object Identifier (DOI). This number provides the electronic link to the published article and should be included in the posting of your personal version. We ask that you wait until you receive this e-mail and have the DOI to do any posting.

Central Storage: This license does not include permission for a scanned version of the material to be stored in a central repository such as that provided by Heron/XanEdu.

18. Author website for books with the following additional clauses:

Authors are permitted to place a brief summary of their work online only.

A hyper-text must be included to the Elsevier homepage at <http://www.elsevier.com> . All content posted to the web site must maintain the copyright information line on the bottom of each image. You are not allowed to download and post the published electronic version of your chapter, nor may you scan the printed edition to create an electronic version.

Central Storage: This license does not include permission for a scanned version of the material to be stored in a central repository such as that provided by Heron/XanEdu.

19. Website (regular and for author): A hyper-text must be included to the Homepage of the journal from which you are licensing at <http://www.sciencedirect.com/science/journal/xxxxx>. or for books to the Elsevier homepage at <http://www.elsevier.com>

20. Dissertation/Dissertation: If your license is for use in a dissertation/dissertation your dissertation may be submitted to your institution in either print or electronic form. Should your dissertation be published commercially, please reapply for permission. These requirements include permission for the Library and Archives of Canada to supply single copies, on demand, of the complete dissertation and include permission for UMI to supply single copies, on demand, of the complete dissertation. Should your dissertation be published commercially, please reapply for permission.

21. Other Conditions: Permission is granted to submit your article in electronic format. This license permits you to post this Elsevier article online if it is embedded within your dissertation. You are also permitted to post your Author Accepted Manuscript online however posting of the final published article is prohibited. Please refer to Elsevier's Posting Policy for further information:
<http://www.elsevier.com/wps/find/authors.authors/postingpolicy>

v1.6

If you would like to pay for this license now, please remit this license along with your payment made payable to "COPYRIGHT CLEARANCE CENTER" otherwise you will be invoiced within 48 hours of the license date. Payment should be in the form of a check or money order referencing your account number and this invoice number RLNK501043469. Once you receive your invoice for this order, you may pay your invoice by credit card.

Please follow instructions provided at that time.

Make Payment To:

Copyright Clearance Center

Dept 001

P.O. Box 843006

Boston, MA 02284-3006

For suggestions or comments regarding this order, contact RightsLink Customer

Support:customer@copyright.com or +1-877-622-5543 (toll free in the US) or +1-978-646-2777.

Gratis licenses (referencing \$0 in the Total field) are free. Please retain this printable license for your reference. No payment is required.

Permissions for Chapters 5 and 6

ELSEVIER LICENSE

TERMS AND CONDITIONS

Mar 26, 2014

This is a License Agreement between John T Favreau ("You") and Elsevier ("Elsevier") provided by Copyright Clearance Center ("CCC"). The license consists of your order details, the terms and conditions provided by Elsevier, and the payment terms and conditions.

All payments must be made in full to CCC. For payment instructions, please see information listed at the bottom of this form.

Supplier	Elsevier Limited
	The Boulevard, Langford Lane
	Kidlington, Oxford, OX5 1GB, UK

Registered Company Number	1982084
---------------------------	---------

Customer name	John T Favreau
---------------	----------------

Customer address	60 Prescott Street
------------------	--------------------

WORCESTER, MA 01605

License number	3320251079580
----------------	---------------

License date	Feb 01, 2014
--------------	--------------

Licensed content publisher	Elsevier
Licensed content publication	Journal of Vascular Surgery
Licensed content title	Acute reductions in mechanical wall strain precede the formation of intimal hyperplasia in a murine model of arterial occlusive disease
Licensed content author	John T. Favreau, Chengwei Liu, Peng Yu, Ming Tao, Christine Mauro, Glenn R. Gaudette, C. Keith Ozaki
Licensed content date	17 October 2013
Licensed content volume number	
Licensed content issue number	
Number of pages	1
Start Page	0
End Page	0
Type of Use	reuse in a dissertation/dissertation
Intended publisher of new work	other

Portion	full article
Format	both print and electronic
Are you the author of this Elsevier article?	Yes
Will you be translating?	No
Title of your dissertation/dissertation	Cyclic mechanical strain reduction temporally precedes arterial intimal hyperplasia in a murine model
Expected completion date	May 2014
Estimated size (number of pages)	100
Elsevier VAT number	GB 494 6272 12
Permissions price	0.00 USD
VAT/Local Sales Tax	0.00 USD / 0.00 GBP
Total	0.00 USD
Terms and Conditions	

INTRODUCTION

1. The publisher for this copyrighted material is Elsevier. By clicking "accept" in connection with completing this licensing transaction, you agree that the following terms and conditions apply to this transaction (along with the Billing and Payment terms and conditions established by Copyright Clearance Center, Inc. ("CCC"), at the time that you opened your Rightslink account and that are available at any time at <http://myaccount.copyright.com>).

Licensing material from an Elsevier book: A hyper-text link must be included to the Elsevier homepage at <http://www.elsevier.com>. All content posted to the web site must maintain the copyright information line on the bottom of each image.

Posting licensed content on Electronic reserve: In addition to the above the following clauses are applicable: The web site must be password-protected and made available only to bona fide students registered on a relevant course. This permission is granted for 1 year only. You may obtain a new license for future website posting.

For journal authors: the following clauses are applicable in addition to the above: Permission granted is limited to the author accepted manuscript version* of your paper.

*Accepted Author Manuscript (AAM) Definition: An accepted author manuscript (AAM) is the author's version of the manuscript of an article that has been accepted for publication and which may include any author-incorporated changes suggested through the processes of submission processing, peer review, and editor-author communications.

AAMs do not include other publisher value-added contributions such as copy-editing, formatting, technical enhancements and (if relevant) pagination.

21. Other Conditions:

v1.7

If you would like to pay for this license now, please remit this license along with your payment made payable to "COPYRIGHT CLEARANCE CENTER" otherwise you will be invoiced within 48 hours of the license date. Payment should be in the form of a check or money order referencing your account number and this invoice number RLNK501216334.

Once you receive your invoice for this order, you may pay your invoice by credit card. Please follow instructions provided at that time.

Make Payment To:

Copyright Clearance Center

Dept 001

P.O. Box 843006

Boston, MA 02284-3006

For suggestions or comments regarding this order, contact RightsLink Customer

Support: customer care@copyright.com or +1-877-622-5543 (toll free in the US) or +1-978-646-2777.

Gratis licenses (referencing \$0 in the Total field) are free. Please retain this printable license for your reference. No payment is required.

Appendix B: Staining protocols and controls

Masson's Trichrome

This protocol was provided courtesy of the WPI Gateway Park histology core.

Biebrich Scarlet Acid Fuchsin stock solution (Red)

Biebrich scarlet aqueous 1%	90.0ml
Acid Fuchsin aqueous 1%	10.0ml
Glacial Acetic Acid 100%	1.0ml

Biebrich scarlet aqueous 1%

Biebrich Scarlet	1.0gm
DH ₂ O	99.0ml

Acid Fuchsin aqueous 1%

Acid fuchsin	1.0gm
DH ₂ O	99.0ml

Phosphomolybdic-Phosphotungstic Acid Solution (Yellow)

Phosphomolybdic acid	5.0gm
Phosphotungstic acid	5.0gm
DH ₂ O	200.0ml

Aniline Blue solution (Blue)

Aniline blue	2.5gm
Glacial Acetic acid 100%	2.0ml
DH ₂ O	100.0ml

1% Glacial Acetic Acid solution

Glacial acetic acid 100%	1.0ml
DH ₂ O	100.0ml

Hematoxylin Solution A

Hematoxylin crystals	1.0gm
95% Alcohol	100.0ml

Hematoxylin Solution B

Ferric Chloride, 29% aqueous	4.0ml
DH ₂ O	95.0ml

Hydrochloric acid, concentrated	1.0ml
---------------------------------	-------

Ferric chloride 29%

Ferric chloride	29.0gm
DH ₂ O	100.0ml

Weigerts Iron Hematoxylin solution

Equal parts of solution A and B

Run a control slide.

Control tissue: Heart, uterus, skin.

Safety equipment: Work under a hood with lab coat, gloves, and glasses.

1. De-paraffin slides in xylene (1)----- 2 minutes (re-use)
2. De-paraffin slides in xylene (2)----- 2 minutes (re-use)
3. Clear slides in 100% alcohol----- 2 minutes
4. Clear slides in 100% alcohol----- 2 minutes
5. Hydrate slides in 95% alcohol----- 2 minutes
6. Hydrate slides in running water----- 5 minutes
7. Bouin's at 60 degrees Celsius----- 1 hour (re-use)
8. Wash in running water ----- 10 minutes
9. Weigert's Hematoxylin (make fresh) ----- 10 minutes (dump)
10. Wash in running water ----- 10 minutes
11. Biebrich Scarlet Acid Fuchsin----- 10 minutes (re-use)
12. Rinse in running water----- 2 minutes
13. Phosphomolybdic / Phosphotungstic acid----- 10 minutes (re-use)
14. No rinse, goes directly into blue
15. Aniline Blue----- 10 minutes (re-use)
16. Rinse in running water----- 1-2 minutes
17. 1% Glacial Acetic Acid----- 5 minutes (re-use)
18. Dehydrate in 95% alcohol----- 1 minute
19. Dehydrate in 95% alcohol----- 1 minute
20. Dehydrate in 100% alcohol----- 1 minute
21. Dehydrate in 100% alcohol----- 1 minute
22. Dehydrate in 100% alcohol----- 5 minutes
23. Clear in xylene (4)----- 2 minutes (re-use)
24. Clear in xylene (5)----- 5 minutes (re-use)

Results:

Nuclei- **Black**

Cytoplasm, keratin, muscle fiber and intercellular fibers- **Red**

Collagen- **Blue**

Weigerts Iron Hematoxylin:

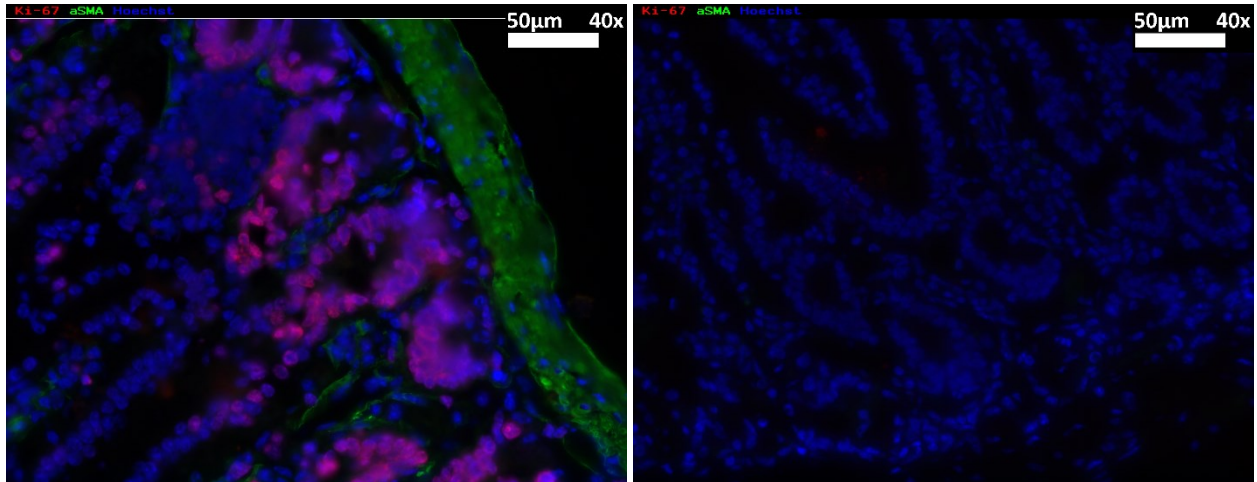
Equal parts of solutions A and B – 20ml and 20ml for tall glass staining coplin jar.

Ki-67 and alpha Smooth Muscle Actin

Control tissue

- Mouse intestine (+)
- Use primary delete negative control

Sample positive control below (left) and negative control (right) with alpha smooth muscle actin in green, Ki-67 in red and nuclei in blue



Deparaffinize

Materials

- Xylene
- Ethanol
- DI water
- Tap water

Procedure

1. Xylene 1 for 3 minutes
2. Xylene 2 for 3 minutes
3. 100% ethanol for 3 minutes
4. 100% ethanol for 3 minutes
5. 95% ethanol for 3 minutes
6. 70% Ethanol for 3 minutes
7. 50% ethanol for 3 minutes
8. Rinse in running tap water for 5 minutes

Heat induced epitope retrieval

Materials

- Tris-EDTA buffer (pH 9.0)

- 1.21 grams Tris HCl (MP Biomedical, 816124)
- 0.37 grams Ethylenediaminetetraacetic acid (EDTA. Sigma, ED4SS)
- 1000 mL Distilled water
- 0.5 mL Tween 20

Mix Tris, EDTA and DI water. pH should be near 9.0 but adjust as necessary. Add Tween 20

- Pressure cooker

Procedure

While deparaffinizing slides, bring 1L Tris-EDTA buffer to a boil in the unsealed pressure cooker. Once buffer is at a rolling boil, transfer slides to a metal slide rack and place in the boiling buffer solution. Seal the pressure cooker and wait until it reaches full pressure (gas escapes pressure release valve). Time 3 minutes from onset of full pressure. After 3 minutes, transfer pressure cooker to sink, release pressure and run cold water into pressure cooker for 10 minutes.

Staining protocol

Materials

- Phosphate buffered saline (PBS)
- 0.25% Triton-X 100 in DI H₂O
- 5% Goat serum in PBS
- 3% Goat serum in PBS
- Primary:
 - Mouse anti Alpha, smooth muscle actin monoclonal 1:50 (Abcam,AB7817)
 - Rabbit anti Ki-67 monoclonal 1:100 (Sigma,AB16667)
 - In 3% goat serum
- Hoechst dye 1:6000 in PBS
- Secondary:
 - Alexa-fluor 488 goat anti-mouse 1:400 (Invitrogen A11029)
 - Alexa-fluor 568 goat anti-rabbit 1:400 (Invitrogen A11036)
 - In 3% goat serum
- Cytoseal-60

Procedure

1. Wash 3x in PBS for 5 mins
2. Permeabilize with 0.25% Triton X for 20 mins
3. Block with 5% goat serum in PBS for 30 mins
4. Incubate in primary antibody overnight at 4 degC
5. Wash 3x in PBS for 5 mins
6. Incubate in secondary antibody for 1 hr at room temperature
7. Wash 3x in PBS for 5 mins
8. Counterstain with Hoechst for 5 minutes

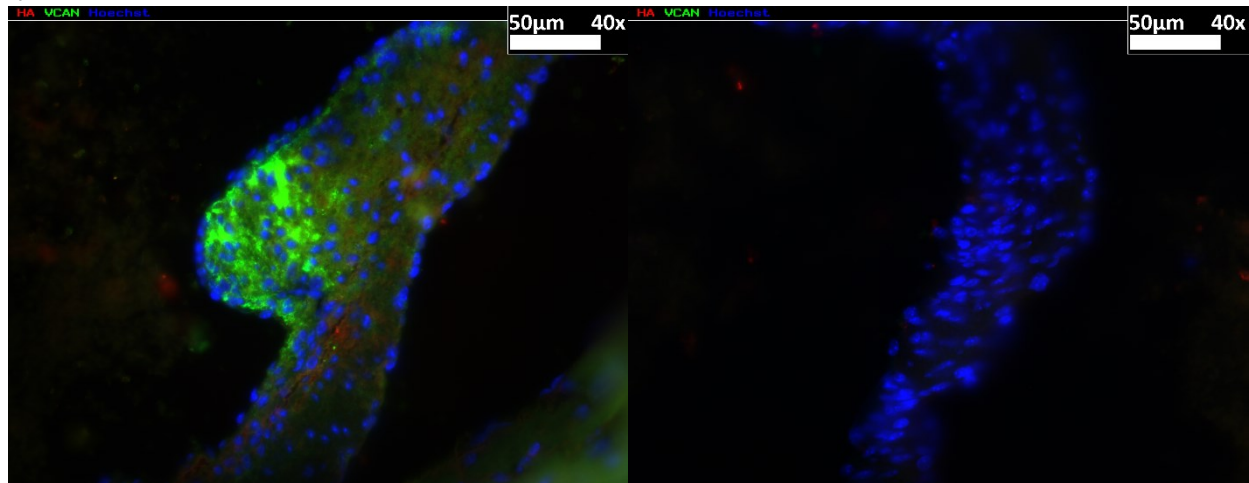
9. Wash 3x in PBS for 5 mins
10. Coverslip with cyto seal-60

Hyaluronic acid and Versican

Control tissue

- Mouse heart valve (+)—Use longitudinal sections of the mouse heart
- Use primary delete negative control

Sample positive control below (left) and negative control (right) with versican in green, hyaluronic acid in red and nuclei in blue



Deparaffinize

Materials

- Xylene
- Ethanol
- DI water
- Tap water

Procedure

1. Xylene 1 for 3 minutes
2. Xylene 2 for 3 minutes
3. 100% ethanol for 3 minutes
4. 100% ethanol for 3 minutes
5. 95% ethanol for 3 minutes
6. 70% Ethanol for 3 minutes
7. Rinse in running tap water for 5 minutes

Staining protocol

Materials

- Control tissues: Artery (+) and (-), Heart with valves visible (+) and (-)
- PBS
- 5% Goat serum in PBS
- Sodium acetate buffer
 - NaOAc 50 mM (0.41%)

- NaCl 0.15 M (0.87%)
 - pH 6.0 in D.I. water
- Primary hyaluronidase (-) control
 - 20 units/mL Hyaluronidase from Bovine testes (Sigma, H3506)
 - In Sodium Acetate Buffer
- Primary:
 - Hyaluronic acid binding protein-biotinylated 3 ug/mL, 1:30 (Sigma, H9910)
 - Rabbit anti-mouse Versican 1:150 (Millipore, AB1033)
 - 0.1% BSA, 3% Goat serum in PBS
- Secondary:
 - Alexa-fluor 488 goat anti-rabbit 1:400 (Invitrogen, A-11008)
 - Alexa-fluor 568 Streptavidin 1:400 (Invitrogen, S-11226)
 - 0.1% BSA, 3% goat serum in PBS
- Hoechst 33342 dye 1:6000 in PBS ()
- Cytoseal-60

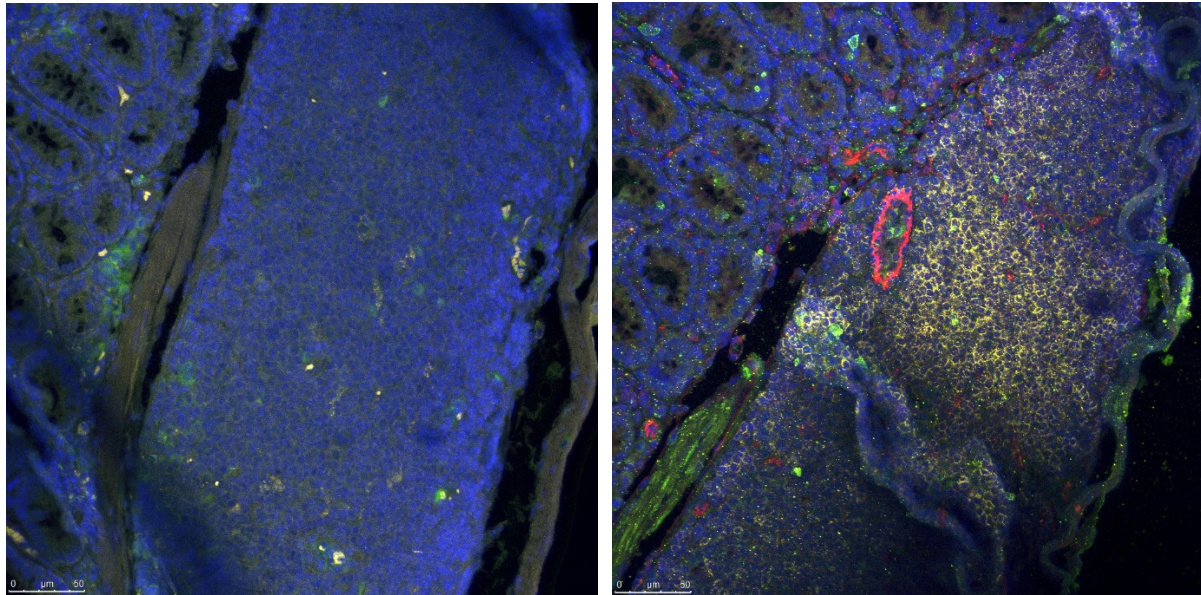
Procedure

1. Wash 3x in PBS for 5 mins
2. Permeabilize with 0.25% Triton X for 20 mins
3. Wash 3x in PBS for 5 mins
4. Perform Enzyme digestion of HA in negative controls (Leave positive controls in Sodium acetate buffer) for 1 hr at 37 degC
5. Wash 3x in PBS for 5 mins
6. Block with 5% goat serum/1% BSA in PBS for 1 Hour
7. Incubate in primary antibody overnight at 4 degC
8. Wash 3x in PBS for 5 mins
9. Incubate in secondary antibody for 1 hour at room temp
10. Wash 3x in PBS for 5 mins
11. Counterstain with Hoechst for 5 minutes
12. Wash 3x in PBS for 5 mins
13. Coverslip with cyto seal

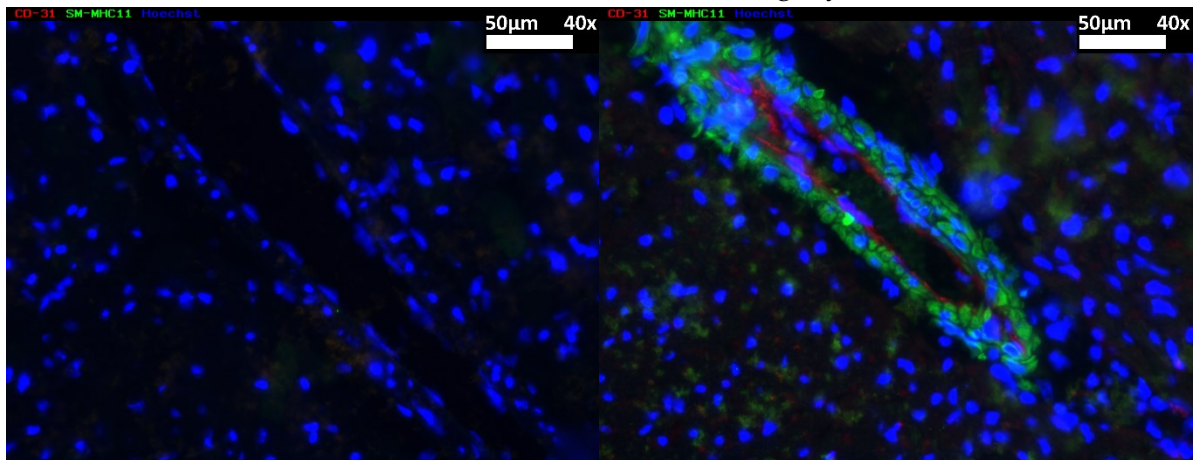
Myosin Heavy Chain, CD-31 and CD-45

Controls

Intestine control (CD-45 in yellow shows up clearly) Positive control (right) and primary delete control (left)



Heart control (Myosin heavy chain in green and CD-31 in red). These two stains are clearly visible in the blood vessels in the heart. Note that surrounding myocardium is not stained.



Deparaffinize

Materials

- Xylene
- Ethanol
- DI water
- Tap water

Procedure

1. Xylene 1 for 3 minutes

2. Xylene 2 for 3 minutes
3. 100% ethanol for 3 minutes
4. 100% ethanol for 3 minutes
5. 95% ethanol for 3 minutes
6. 70% Ethanol for 3 minutes
7. 50% ethanol for 3 minutes
8. Rinse in running tap water for 5 minutes

Antigen retrieval

Materials

- Citrate Buffer (1mM Citric Acid, 0.05% Tween 20, pH 6.0)
 - Citric acid (anhydrous) ----- 1.92 g
 - Distilled water ----- 1000 ml

Mix to dissolve. Adjust pH to 6.0 with 1N NaOH and then add 0.5 ml of Tween 20 and mix well. Store this solution at room temperature for 3 months or at 4 C for longer storage.

- Pressure cooker

Heat induced epitope retrieval

Materials

- Citrate Buffer (1mM Citric Acid, 0.05% Tween 20, pH 6.0)
 - 1.21 grams Tris HCl (MP Biomedical, 816124)
 - 0.37 grams Ethylenediaminetetraacetic acid (EDTA. Sigma, ED4SS)
 - 1000 mL Distilled water
 - 0.5 mL Tween 20 ()

Mix Tris, EDTA and DI water. pH should be near 9.0 but adjust as necessary. Add Tween 20

- Pressure cooker

Procedure

- While deparaffinizing slides, bring 1L Tris-EDTA buffer to a boil in the unsealed pressure cooker. Once buffer is at a rolling boil, transfer slides to a metal slide rack and place in the boiling buffer solution. Seal the pressure cooker and wait until it reaches full pressure (gas escapes pressure release valve). Time 3 minutes from onset of full pressure. After 3 minutes, transfer pressure cooker to sink, release pressure and run cold water into pressure cooker for 10 minutes.

Procedure

1. Place citrate buffer in coplin jar
2. Add coplin jar with citrate buffer to water bath on hot plate
3. Heat to 90-100°C, incubate for 20-40 minutes
4. Remove and allow sections to cool in citrate buffer for 20 minutes at room temperature

Staining protocol

Materials

- Control tissues: Aorta, heart
- PBS
- 0.25% Triton-X 100 in DI H₂O
- 5% Goat serum in PBS
- Primary:
 - Mouse monoclonal anti smooth muscle myosin heavy chain 1:400 (Abcam, AB683)
 - Rabbit anti CD-31 monoclonal 1:50 (Abcam 28364)
 - Rat anti Mouse CD-45 1:50 (BD 550539)
 - 3% goat serum
- Hoechst dye 1:6000 in PBS
- Secondary:
 - Alexa-fluor 488 goat anti-rat 1:400 (Invitrogen A11029)
 - Alexa-fluor 568 goat anti-rabbit 1:400 (Invitrogen A11036)
 - Alexa-fluor 633 goat anti-mouse
 - 3% goat serum
- Cytoseal-60

Procedure

1. Wash 3x in PBS for 5 mins
2. Permeabilize with 0.25% Triton X for 20 mins
3. Block with 5% goat serum in PBS for 30 mins
4. Incubate in primary antibody overnight at 4 degC
5. Wash 3x in PBS for 5 mins
6. Incubate in secondary antibody for 1 hr at room temperature
7. Wash 3x in PBS for 5 mins
8. Counterstain with Hoechst for 5 minures
9. Wash 3x in PBS for 5 mins
10. Coverslip with cyto seal

Appendix C: Derivation of theoretical strain relationship

Definitions

E_i	Green's Strain at inner wall
E_o	Green's Strain at outer wall
λ_i	Stretch ratio at inner wall
λ_o	Stretch ratio at outer wall
r_o	Outer radius at zero stress state
r_i	Inner radius at zero stress state
R_o	Outer radius at stressed state
R_i	Inner radius at stressed state
L	Length of tubing

Known relationships

Definition of Stretch ratio

$$\lambda_o = \frac{R_o}{r_o} \quad Eq\ 1 \qquad \lambda_i = \frac{R_i}{r_i} \quad Eq\ 2$$

Definition of Green's Strain in 1D

$$E_o = \frac{1}{2}(\lambda_o^2 - 1) \quad Eq\ 3 \qquad E_i = \frac{1}{2}(\lambda_i^2 - 1) \quad Eq\ 4$$

Conservation of tube wall Volume

$$L \cdot (\pi \cdot r_o^2 - \pi \cdot r_i^2) = L \cdot (\pi \cdot R_o^2 - \pi \cdot R_i^2) \quad Eq\ 5$$

Solution

$$E_o = \frac{1}{2} \left(\frac{R_o^2}{r_o^2} - 1 \right)$$

$$E_i = \frac{1}{2} \left(\frac{R_i^2}{r_i^2} - 1 \right)$$

Combine Eq1, Eq3

Combine Eq2, Eq4

$$R_o^2 = r_o^2 (2 \cdot E_o + 1)$$

$$R_i^2 = r_i^2 (2 \cdot E_i + 1)$$

Solve for R_o^2 and R_i^2

$$r_o^2 - r_i^2 = r_o^2 (2 \cdot E_o + 1) - r_i^2 (2 \cdot E_i + 1)$$

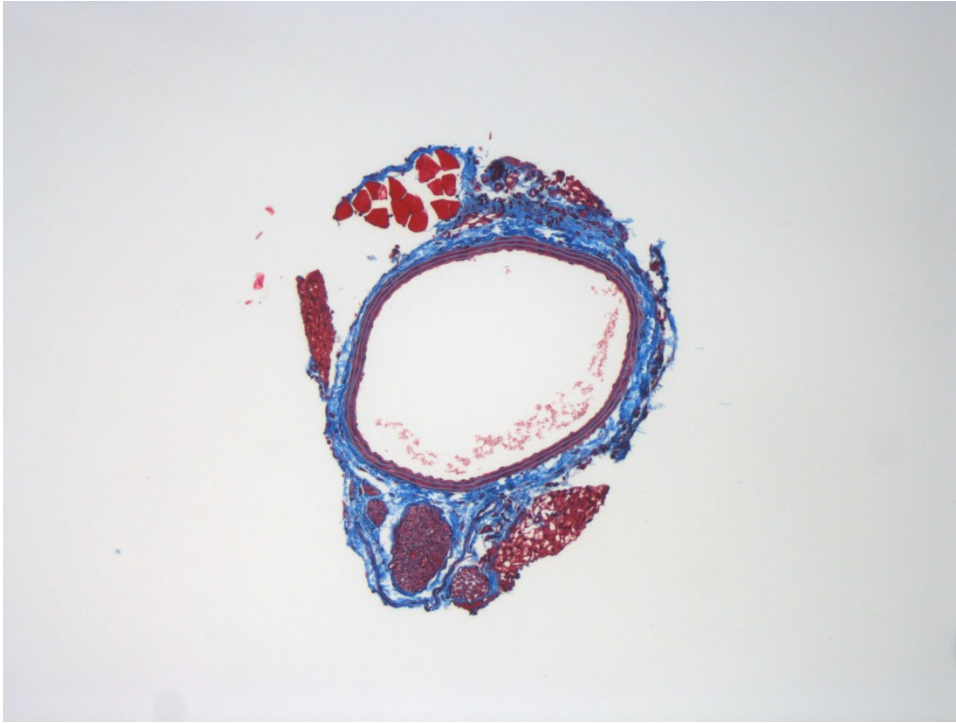
Simplify Eq5 and input
values for R_o^2 and R_i^2

$$E_o = \frac{r_i^2}{r_o^2} \cdot E_i$$

Simplify and solve for E_c

Appendix D: Determination of vessel layer thickness

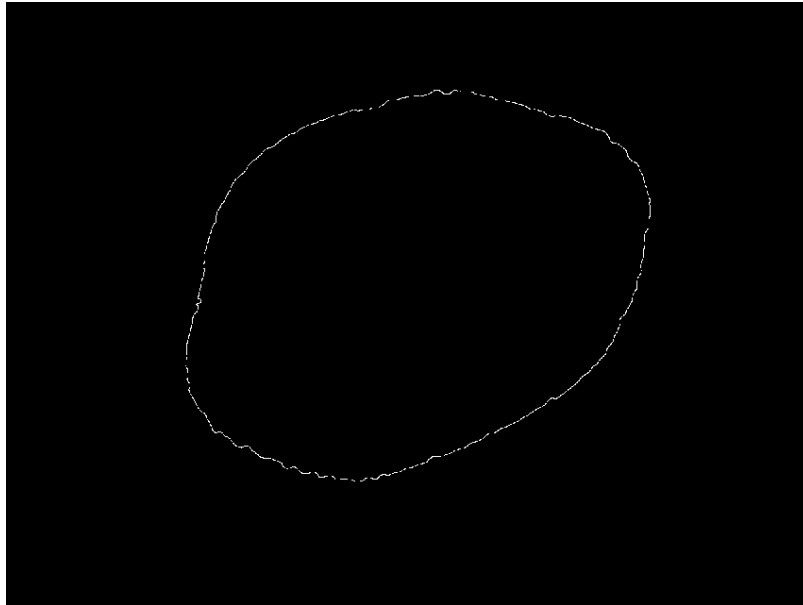
1. Original image:



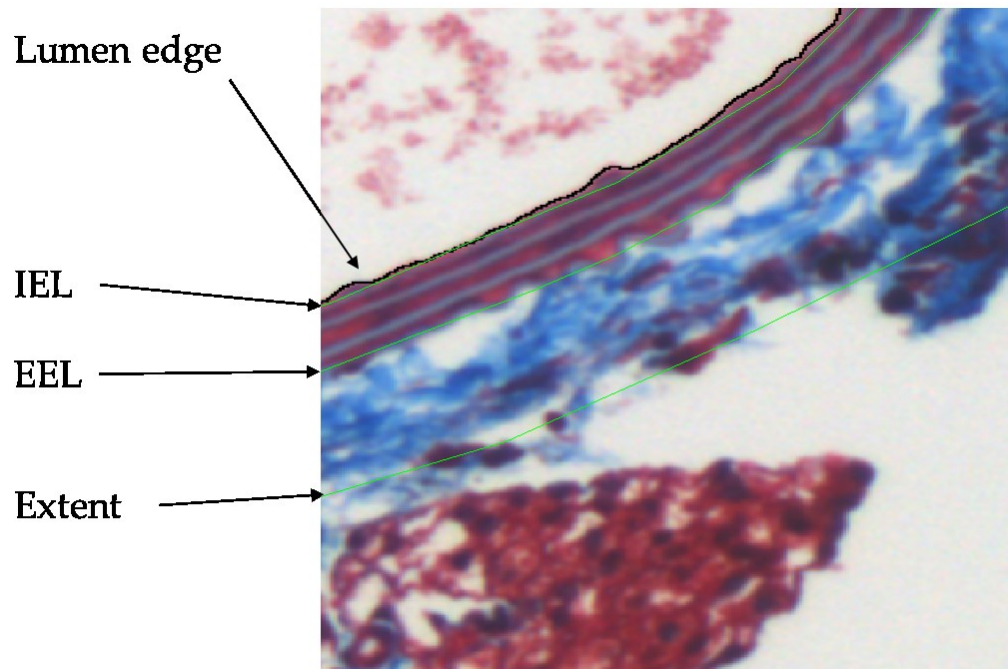
2. Thresholded image:



3. Extraction of lumen edge:



4. User selection of IEL, EEL and vessel extent:



5. Convert pixel areas to area in microns²:

$$R = 0.540 \cdot \frac{\mu\text{m}}{\text{pixellength}} \quad (\text{Known value for our scope, camera and objective})$$

$$A_{\text{micron}} = A_{\text{pix}} \cdot R^2$$

6. For each area, calculate ideal radius:

$$r_{\text{ideal}} = \sqrt{\frac{A_{\text{micron}}}{\pi}}$$

7. Compute vessel parameters from ideal radii:

- Intimal thickness:

$$t_I = r_{\text{iel}} - r_{\text{lumen}}$$

- Wall thickness:

$$t_{\text{wall}} = r_{\text{extent}} - r_{\text{lumen}}$$